Dipl.-Ing. Ozan Caliskanoglu

HOT DUCTILITY INVESTIGATIONS OF CONTINUOUSLY CAST STEELS

DISSERTATION

Submitted to the
Faculty of Mechanical Engineering and Economic Sciences at
Graz University of Technology
in Partial Fulfillment of the Requirements for the Degree of
"Doktor der technischen Wissenschaften"

Institute of Materials Science and Welding
Graz, 2015

Supervisors:	Univ.-Prof. Dipl.-Ing. Dr. techn. Christof Sommitsch
	Dr. Eng. Coline Béal
Reviewers:	Univ.-Prof. Dipl.-Ing. Dr. techn. Christof Sommitsch
	Univ.-Prof. Dipl.-Ing. Dr. techn. Ernst Kozeschnik

Preface

This PhD thesis is submitted for the degree “Doktor der technischen Wissenschaften” at the Faculty of Mechanical Engineering and Economic Sciences at Graz University of Technology. The work was conducted under the supervision of Prof. Christof Sommitsch at the Institute of Materials Science and Welding at Graz University of Technology between January 2012 and September 2015. This thesis, which was part of the K1-MET research program “Thermomechanical Modelling of Continuous Casting and Hot Rolling”, was funded and supported by The Austrian Research Promotion Agency (FFG), Austrian Competence Centers for Excellent Technologies (COMET) and voestalpine Stahl GmbH.

I declare that I have authored this thesis independently, that I have not used other than the declared sources/resources, and that I have explicitly marked all material which has been quoted either literally or by content from the used sources.

Ozan Caliskanoglu

Graz, November 2015

Acknowledgements

First of all, I would like to thank Prof. Christof Sommitsch for the supervision of the present thesis and giving me the opportunity to work at the Institute of Materials Science and Welding (IWS) at Graz University of Technology.

I owe particular thanks to my second supervisor Dr. Coline Béal for her kind support during the project.

Special thanks go to Dr. Martina Dikovits for her interim assistance within the last period of the work.

I want to thank Prof. Ernst Kozeschnik from the Institute of Materials Science and Technology at Vienna University of Technology for accepting to read this thesis and also for his valuable support during the whole project.

Furthermore, I would like to thank The Austrian Research Promotion Agency (FFG), Austrian Competence Centers for Excellent Technologies (COMET) and voestalpine Stahl GmbH for supporting and funding the project through the K1-MET research program.

I am very grateful to my colleagues and members of IWS, and to all the people who supported and assisted me in completing this thesis.

Last but not least, the greatest thanks are directed to my family and to my wife for supporting me with encouraging words and deeds not only during the whole work, but also throughout my entire life.

Abstract

Transverse surface cracks in continuously cast steels, which may arise especially during the straightening or unbending operation, represent a significant problem. The probability of crack formation of steels increases as the materials hot ductility becomes worse. This may occur within a temperature range between 600–1200°C and is commonly assessed by conducting laboratory hot tensile tests. In the present work, the hot ductility behavior (second ductility minimum) of low- and Ti-Nb microalloyed steel has been studied in order to analyze the embrittlement and cracking susceptibility after melting and solidification. For this purpose, tensile specimens were subjected to various thermomechanical histories and were pulled to fracture between 650°C and 1000°C. It was found, that the low-alloyed steel embrittles within the two-phase austenite-ferrite region due to thin ferrite films along austenite grain boundaries. In contrast, the Ti-Nb microalloyed steel evinces distinct poor ductility at testing temperatures up to 1000°C, irrespective of which thermal cycle has been utilized or whether the samples have been melted or reheated. Microstructural examinations and supplementary thermo-kinetic computer simulations revealed marked Ti-Nb precipitation which was responsible for the impaired materials hot ductility.

Kurzfassung

Oberflächenquerrisse an stranggegossenen Stählen, die insbesondere während des Richt- oder Rückbiegevorgangs entstehen können, stellen ein ernsthaftes Problem dar. Mit abnehmender Duktilität des Materials steigt auch die Wahrscheinlichkeit der Oberflächenrissbildung. Dies kann in einem Temperaturbereich zwischen 600–1200°C auftreten und wird gewöhnlich mittels Heißzugversuchen im Labor nachgebildet. In der vorliegenden Arbeit wird das Duktilitätsverhalten (2. Duktilitätsminimum) von einem niedrig- und Ti-Nb mikrolegierten Stahl untersucht und die Versprödungs- bzw. Rissneigung nach dem Aufschmelzen und Erstarren analysiert. Zu diesem Zweck wurden Stahlrundproben verschiedenen thermomechanischen Zyklen ausgesetzt und bei Prüftemperaturen zwischen 650°C und 1000°C bis zum Bruch gezogen. Dabei wurde festgestellt, dass der Duktilitätseinbruch am niedriglegierten Stahl im Zweiphasengebiet Ferrit-Austenit aufgrund von dünnen Ferritfilmen an den Austenitkorngrenzen erfolgt. Im Gegensatz dazu weist die mit Ti und Nb mikrolegierte Stahlcharge eine sehr schlechte Duktilität bis zu einer Prüftemperatur von 1000°C auf, unabhängig davon welche thermischen Zyklen durchgeführt oder ob die Proben vorher umgeschmolzen oder nur wiedererwärmt wurden. Mikrostrukturuntersuchungen und begleitende thermokinetische Computersimulationen offenbarten markante Ti-Nb Ausscheidungen, die für den starken Abfall der Duktilität des Materials verantwortlich waren.

List of symbols and abbreviations

Symbol/ abbreviation	Meaning	Unit (SI)
A_0	Initial cross section	m^2
A_{e1}	Lower equilibrium temperature for austenite (γ)	°C
A_{e3}	Upper equilibrium temperature for alpha-ferrite (α)	°C
A_f	Cross section after fracture	m^2
A_{r3}	Austenite-to-ferrite transformation temperature on cooling	°C
bcc	Body-centered cubic	
CCT	Continuous cooling transformation diagram	
D	Particles mean diameter	m
ε	Strain	
$\dot{\varepsilon}$	Strain rate	s^{-1}
EDX	Energy-dispersive X-ray	
F_{max}	Maximum tensile force	N
fcc	Face-centered cubic	
L	Active deformed slab length	m
LOM	Light optical microscopy	
N_V	Particles number density	m^{-3}
PFZ	Precipitate-free zone	
ppm	Particles per million	
R	Bending radius	m
RA	Reduction of area after fracture	%
RA_{crit}	Critical reduction of area after fracture	%
σ_{max}	Ultimate tensile stress	Pa
SEM	Scanning electron microscopy	
SSCC	Surface structure control cooling	
t	Slab thickness	m
T_L	Liquidus-temperature	°C
T_S	Solidus-temperature	°C
TEM	Transmission electron microscopy	
TTT	Time-temperature-transformation diagram	
v	Casting speed	ms^{-1}
ZDT	Zero-ductility-temperature	°C
ZST	Zero-strength-temperature	°C

Content

1 Introduction

Within a few decades, the continuous casting technology has become one of the most important and innovative sectors of the metal production industry and is accounting for more than 95% of the total crude steel production globally [1]. The method is characterized by a high degree of automation, an improved product quality, shorter processing times and therefore a significant increase in yield [2], [3].

However, defects in casting products cannot always be avoided. During the process, the solidifying slab is exposed to different thermal as well as mechanical loads, which may cause defects like internal or external cracks. Certain steel grades such as microalloyed steels are susceptible to cracking during the continuous slab casting once the occurring stresses and strains can no longer be absorbed causing the materials structure to lose its cohesion significantly. [3], [4]

There are two characteristic temperature regions where steels exhibit distinct poor ductility and are particularly prone to cracking. Depending on the chemical composition, the embrittlement in the high temperature region above approximately 1300°C up to the solidus temperature primarily induces internal cracks and partly longitudinal surface cracks which arise due to the presence of segregated remaining melt within interdendritic and intercellular areas (first ductility minimum). In the second region of low ductility during the unbending and straightening operation roughly between 600°C and 1200°C, however, transverse surface cracks are predominantly formed on the cast steel slabs, which are mainly caused by precipitates and thin ferrite bands surrounding the austenite grain boundaries (second ductility minimum). [5], [6]

This region is especially critical for micro- and low-alloyed steels, since the resulting tensile strains and stresses during the straightening or unbending process may embrittle the cast surface involving marked loss in quality. Required repair works and post-processing on the casting products therefore decrease the productivity causing additional costs. Due to these negative effects, the crack formation mechanisms in continuously cast steels have been the subject of numerous research studies. The plastic deformability and the cracking sensitivity, which strongly depend on various influencing factors such as material and testing

conditions, can be analyzed specifically by means of hot ductility tensile tests.

In most cases, the specimens are heated either directly to the desired testing temperature or to a temperature below the solidus temperature, cooled to the testing temperature and then subsequently strained until fracture [7]. However, there is often a question mark over how appropriate the measurements reflect the microstructural development during the continuous casting process, since the influence of solidification on the precipitation and segregation behavior remains more or less unconsidered. For this reason, many researchers are dealing with the hot tensile testing technique on specimens with preceding melting in order to enable a better physical simulation and a potential transferability to practice.

2 Objectives

This thesis has the main objective to examine the hot ductility of two steel grades, one of them microalloyed with Ti and Nb, with the aim of quantitatively predicting the tendency of surface crack formation during the continuous casting process. In a first step, the principle influence of melting and solidification on the hot ductility is evaluated in order to verify the temperature region of ductility loss (second ductility minimum) and to characterize its underlying root cause by applying the casting simulator BETA 250-5 and subsequent metallographic fracture analyses. On the basis of the results obtained, further studies on the effect of individual process parameters such as peak temperature and cooling rate on the hot ductility of the microalloyed steel are performed. The purpose of the present research is therefore twofold: to gain a better understanding of the crack formation mechanisms and to correlate the respective findings with industrial experience so that appropriate measures can be taken to prevent crack initiation during casting in order to enhance quality and productivity, respectively.

3 Literature review

This chapter includes an overview and relevant literature related to the study of the hot ductility of continuously cast steels. First, the continuous casting and the problem of the crack formation will be outlined, followed by a general description of the hot ductility of steels and its influencing factors.

3.1 Continuous casting

With the development and commissioning of continuous casting facilities, a new era of crude steel production began in the middle of the last century. Fig. 1 shows the world's total crude steel production by regions. It can be seen, that the crude steel production in most regions remained more or less constant, except China, whose output grew by more than 600% to 823 million tons compared to 2000 (129 mill. t).

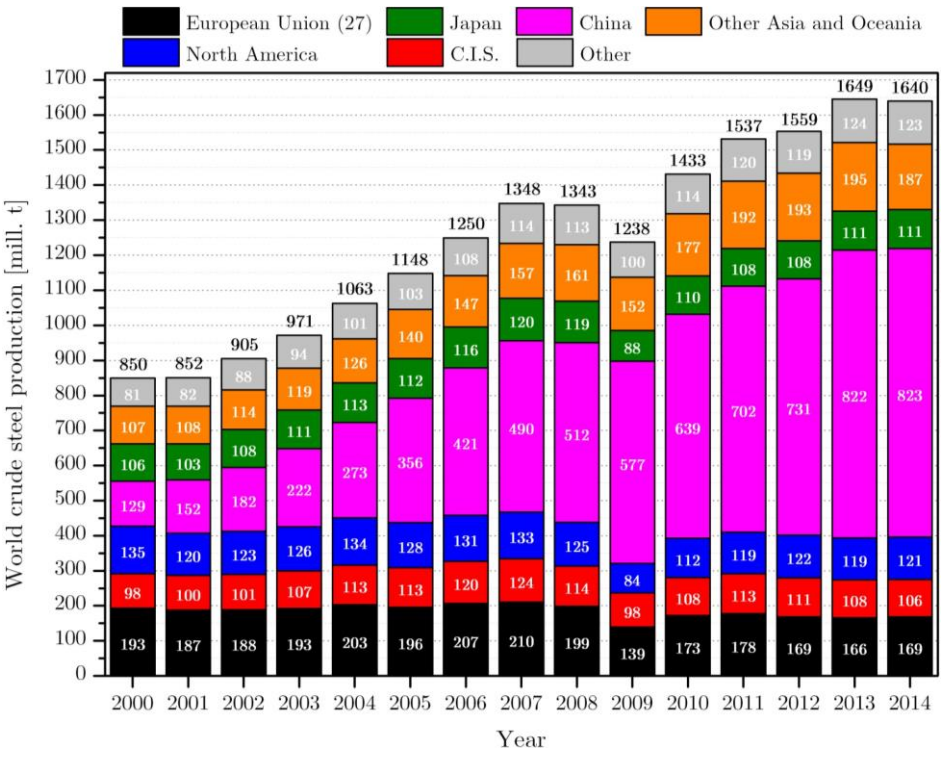

Fig. 1: Total production of crude steel in million tons and shares of selected countries and regions from 2000 to 2014. Based on [1].

The share of continuously cast semi-products including billets, blooms and slabs[1] in world's total crude steel production since the commercial deployment has rapidly increased and has meanwhile reached an historic high of 96.1%, Fig. 2a. Over the past 20 years alone, the annual global output of continuously cast products has more than tripled and has achieved a record high of 1584 million tons in 2013. In the last decades, this clear trend could be noticed in Austria as well. Within a few years, the share of continuous casting almost doubled from 51.2% (1980) to 93.4% (1985) and reached in 2013 a share of 96.4%, Fig. 2b. [1]

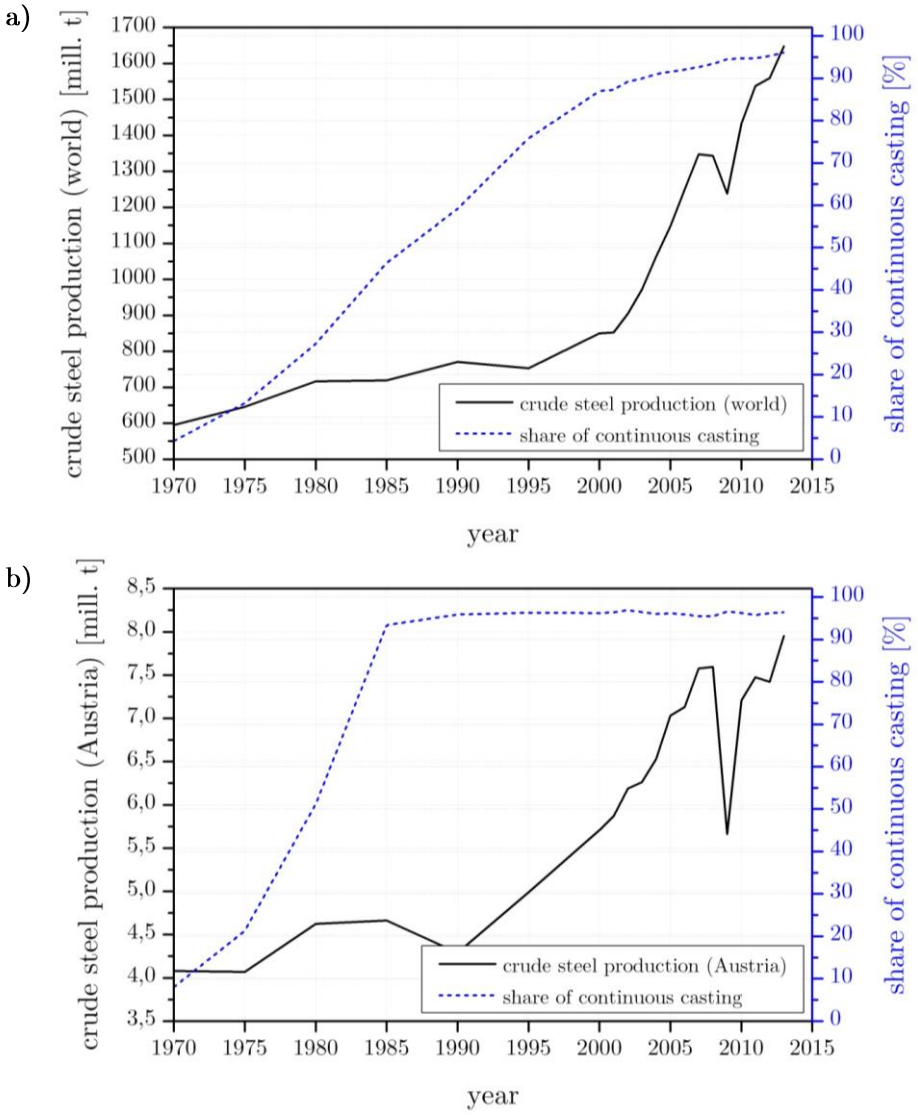

Fig. 2: Crude steel production in million tons and percentage share of continuous casting from 1970 to 2013. a) World. b) Austria. After [1].

[1] billets: cross sections with a side length of about 150mm.
blooms: cross sections with a side length more than 150mm; thickness to width ratio=1:1.3.
slabs: cross sections with a thickness>100 mm; thickness to width ratio>1:1.3. Depending on diameter and cross section lengths, round and multi-side strands are considered as billets or blooms [4].

The process is characterized by the manufacture of high-quality products regarding surface quality, uniformity, degree of purity, as well as substantial energy and cost savings. Thus, the former widespread ingot casting, which requires additional time and cost consuming processing steps, has been largely replaced by the continuous casting technology. [3]

During continuous casting, the liquid metal is poured from a casting ladle into a tundish, where the alloy melt continues flowing downstream through a bottom outlet valve into a water-cooled copper mould, Fig. 3. This facilitates the formation of a thin solidified shell by the heat dissipation through the direct contact with the mould wall (primary cooling zone). In order to stabilize the molten steel and to retain its desired shape, a rigid dummy bar is inserted into the mould, which is then being continuously stripped downwards.

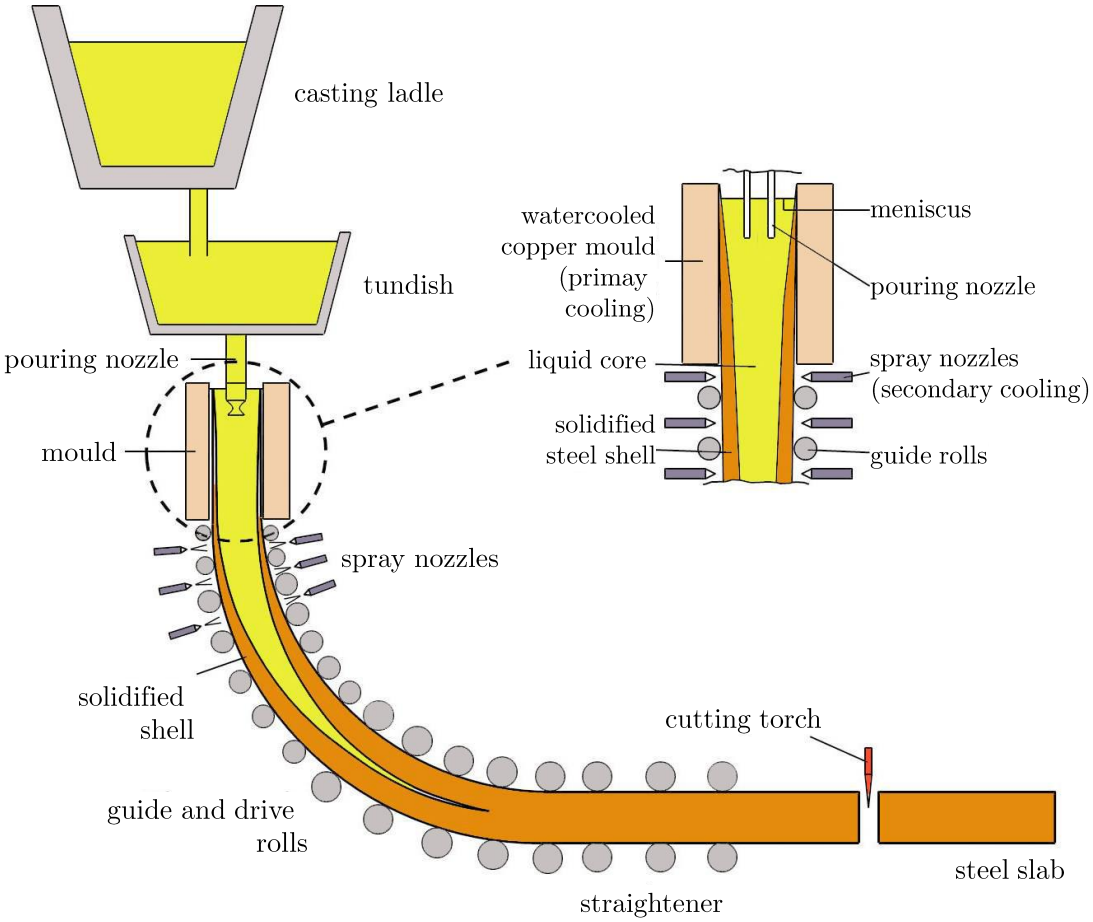

Fig. 3: Schematic illustration of a curved continuous slab caster with straightener. Based on [2], [8].

The casting speed must be selected in such a way that a sufficient outer strand is formed and that an unexpected breakout of the melt below the mould will not occur. To prevent the solidifying shell from sticking to the mould walls, the mould is oscillated up and down usually according to a sinusoidal motion. Furthermore, mould lubricants are also used to

decrease the friction between the mould and the strand. Afterwards, the partially solidified strand exits the primary cooling zone and is further transported to the so-called secondary cooling zone using appropriate support rolls. Here, the majority of the heat extraction is performed by a series of spray water cooling nozzles. Moreover, additional heat removal is achieved by the natural radiation and convection as well as by the thermal conduction due to the contact between the casting and the support rolls. After the strand is completely solidified, the slab is cut to the desired lengths by a cutting torch and is then either transported to certain cooling beds by a runout-table or is directly conveyed to hot- or cold-rolling systems. [2], [3]

Depending on the alloy and dimension to be cast, a distinction is made between vertical, curved or bow-type with one ore multiple strengthening points as well as infrequently oval bow-type or horizontal slab casters. Especially in the case of large steel slabs and due to the problem of the strand shell bulging as a result of the ferrostatic pressure, it is thus necessary to adequately support the strand shell at least until the end of the liquid core. Therefore, the bow-type form became the most widely used continuous slab caster today and is schematically shown in Fig. 3 [4], [7]. At low casting speeds, the straightening operation is carried out on a completely solidified slab, possibly contributing to high mechanical roller loads. With increasing casting speeds, on the other hand, the liquid core is extended to the horizontal segment, which may lead again to bulging and to the creation of “whale”-shape structures, thus causing a breakdown of the casting process. Apart from that, the slab is subjected to various other thermal and mechanical loads, which may cause marked quality losses. A detailed description of such stresses during continuous casting was once published by Lankford [8] and will be briefly addressed in the following section.

3.1.1 Thermal and mechanical stresses

During solidification within the mould, the liquid sump exerts a ferrostatic pressure on the newly developed skin, whereby the skin bulges outwards until a complete contact between the shell and the mould surface is achieved. In this manner, mainly tensile stresses arise at the solidification front and the shell, reaching their maximum at the center of the strand in transverse direction. Below the mould, a bulging of the slab between the support-rolls may occur as well, which may generate tensile stresses on the strand surface and compressive stresses on the solidification front, Fig. 4. [8]

By pulling the slab from the primary cooling zone, friction forces between the oscillating mould-wall and the already solidified strand shell are also created, whose extend depends on

the friction coefficient and on the pressing force owing to the ferrostatic pressure as mentioned above.

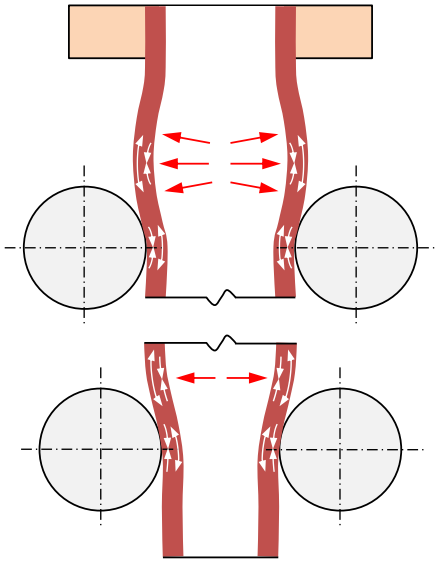

Fig. 4: Schematic illustration of the bulging process due to poorly adjusted support rolls. Based on [8].

Depending on the mould stroke, the friction at the strand surface causes axial as well as additional bending stresses, which are of tensile nature during the downward stroke and compressive during the upward stroke. Fig. 5 shows an overview of the resulting tensile stresses in the solidifying shell during the upward mould stroke.

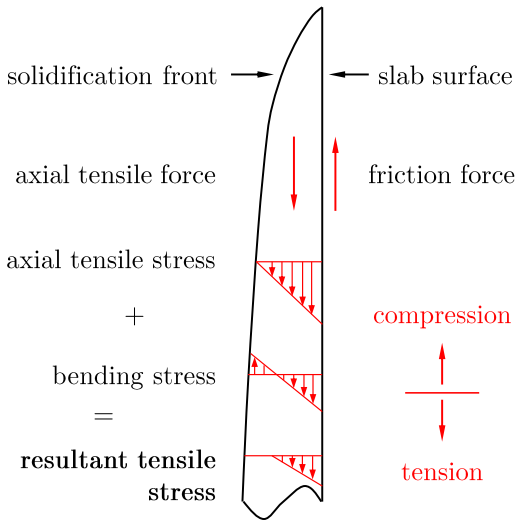

Fig. 5: Forces and stresses in the solidifying shell through the friction force within the mould. Based on [8].

Moreover, the weight force of the slab generates an axial tensile stress on the strand shell, which can be either increased or decreased depending on the driving power of the drive rolls.

If the strand will be compressed by the drive rolls for instance (compression casting), the effective axial force is then equal to the weight force minus the driving force. The unbending or straightening operation, however, basically induces the highest mechanical stresses on the cast surface, which are compressive in the bottom areas and tensile in the top parts of the slab. The respective bending strain ε can then be calculated by dividing the slab thickness t by two times the bending radius R of the casting machine:

$$\varepsilon = \frac{t}{2R}, \tag{1. 1}$$

whereas the strain rate ε can be defined as the product of the strain multiplied by the ratio of the casting speed v to the active deformed slab length L:

$$\dot{\varepsilon} = \varepsilon \frac{v}{L}, \tag{1. 2}$$

Likewise, mechanical stresses may also occur due to a misalignment of the slab guiding frames or due to eccentric support rolls [3].

Furthermore, lateral as well as axial thermal strains and stresses are able to build up within the slab-shell by virtue of the temperature gradient caused through the primary and secondary cooling process. Principally, at any cross section, tensile stresses develop in cooler regions because of the restraint shrinkage in the hotter regions, or vice versa, compressive stresses may be formed in the hotter regions. A non-uniform cooling in the secondary zone at positions with alternating temperature gradients may similarly produce local tensile and compressive stresses. Further thermal stresses in continuously cast materials may also result from eccentric or misaligned pouring streams, distorted mould or from transformation induced strains. [8]

In certain temperature ranges some steels exhibit a poor ductility, in which they may easily embrittle even at very small loads. All these stresses can promote the formation of different cracks which will be delineated in the following section.

3.1.2 Crack formation in continuous casting

Cracks in continuously cast products can cause significant losses in the output of good material, in the worst case even leading to a shutdown of the casting machines. The various crack types can arise from almost anywhere and can propagate in all directions as schematically represented in Fig. 6.

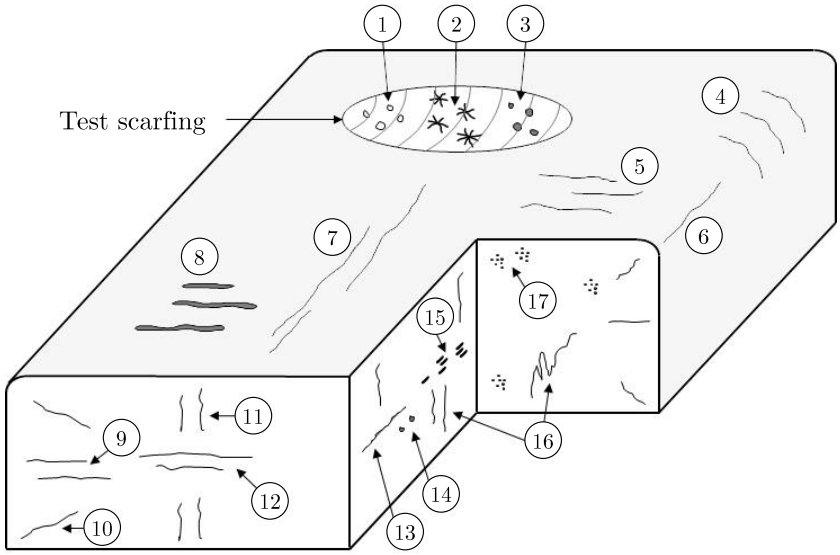

surface defects

1. pinholes
2. star cracks
3. macro inclusions
4. transverse corner cracks
5. transverse surface cracks
6. longitudinal corner cracks
7. longitudinal surface cracks
8. deep oscillation marks

internal defects

9. side halfway cracks
10. internal corner cracks
11. straightening/bending, midway or pinch roll cracks
12. centreline cracks
13. centreline segregation
14. semi macrosegregation
15. porosity
16. halfway cracks
17. non metallic inclusions, clusters

Fig. 6: Schematic drawing of potential surface and internal defects in continuously cast slabs. Based on [5], [9].

Internal cracks preferably develop in the high temperature region near the solidus temperature of the alloy, where steels evince a low strength and ductility. However, surface cracks may already form within the mould on the solidifying strand skin (oscillation marks). Transverse surface and corner cracks on cast slabs are frequently observed in the secondary cooling zone. From a qualitative point of view, surface cracks are more problematic than internal cracks, since the formation of additional oxide scale layers at the defective areas may not fuse to the underlying bulk material in the subsequent rolling process. This requires further post-processing, therefore decreasing the efficiency. Especially in the hot charging or direct rolling process in modern plants, such surface treatments cannot be always executed. Thus, a production of defect-free cast structures is often indispensable. In the following Fig. 7, a few examples for diverse surface defects in continuously cast slabs are given.

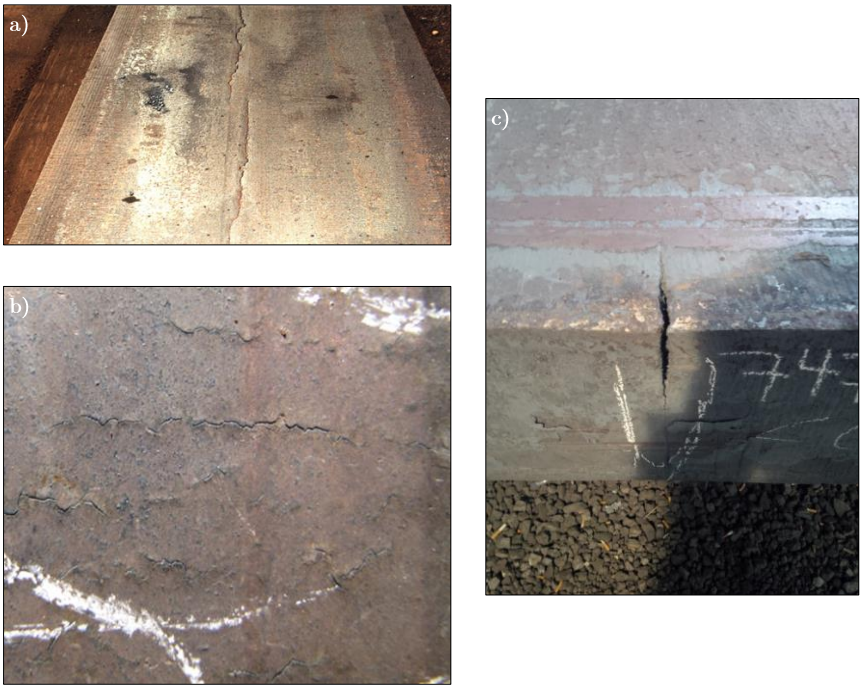

Fig. 7: Continuously cast slabs with diverse surface defects. a) Longitudinal surface cracks, b) transverse surface cracks and c) transverse corner crack.

Appropriate recommendations for preventing transverse surface crack initiation can be found in [5], [10]. These include e.g. an execution of uniform and proper water spray cooling in order to minimize surface temperature gradients and to prevent straightening within unfavorable temperature ranges.

3.2 Hot ductility of steels

The cracking susceptibility of continuously cast steels is strongly related to the decreased deformability or poor ductility at certain temperature levels. There are different testing methods in order to investigate the high-temperature properties such as the ductility of materials under continuous casting conditions. The most common way is to conduct hot tensile tests by pulling the samples until fracture according to a specific thermomechanical cycle and by measuring the reduction of area (RA) in percent, which is expressed by

$$RA = \left(1 - \frac{A_f}{A_0}\right) \cdot 100\,[\%], \qquad (1.\ 3)$$

where A_f denotes the cross section after fracture and A_0 the initial cross section of the specimen. Basically, the higher the RA-value, the more the material is able to deform and therefore the less the material is prone to cracking.

Additional materials high-temperature properties such as the ultimate tensile stress σ_{max}, is also often ascertained using the equation

$$\sigma_{max} = \frac{F_{max}}{A_0} \text{ [MPa]}, \qquad (1.\ 4)$$

with F_{max} as the maximum tensile force during testing. As can be seen in Fig. 8, the stress basically declines with increasing deformation temperature until it becomes zero, the zero-strength-temperature (ZST). Two distinct drops in ductility ($RA<RA_{crit}$) can be predominantly recognized when plotting RA against the deformation temperature (blue line).

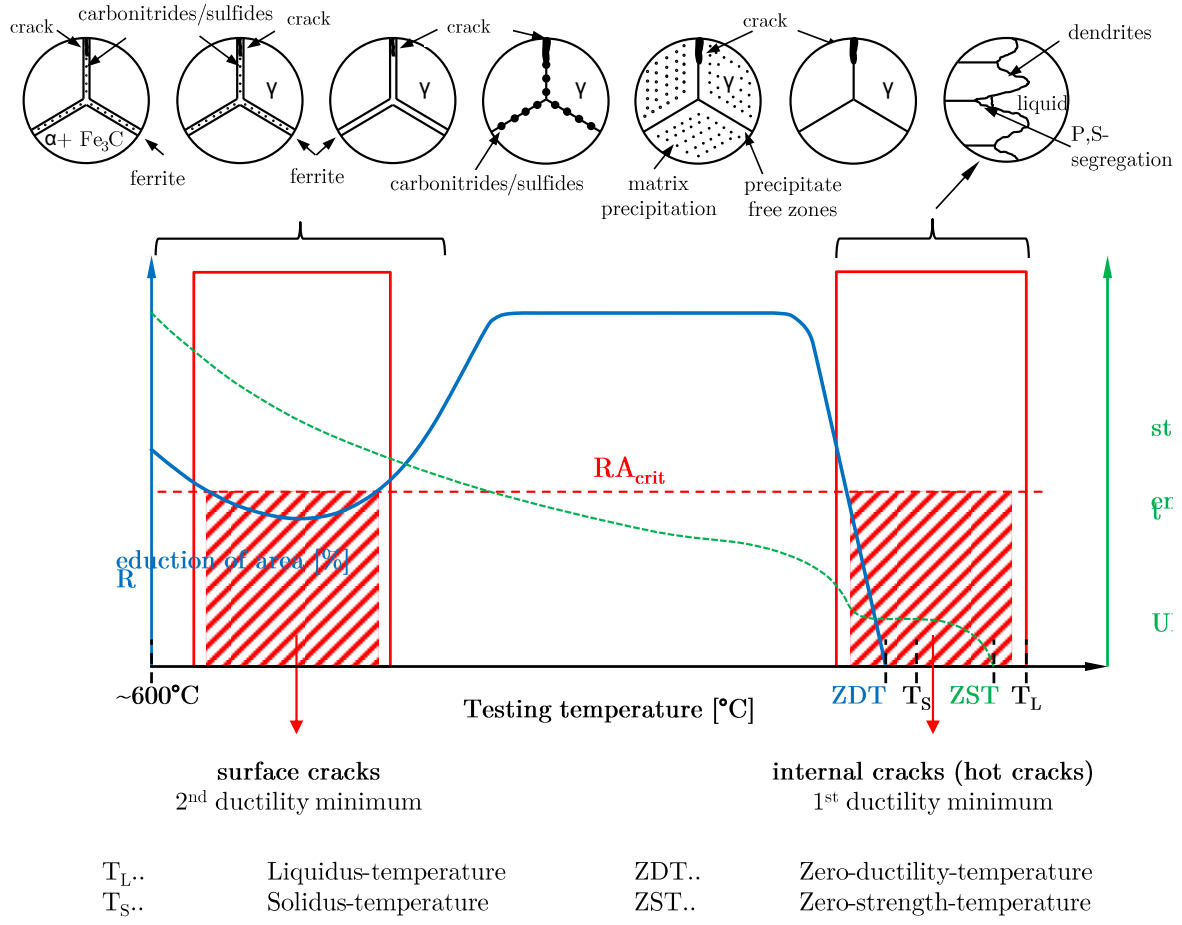

Fig. 8: Different mechanisms affecting the hot ductility of steels. Based on [7].

As per Mintz et al. [11], the recommended value for RA_{crit} is 40%, while Suzuki et al. [12] are suggesting a minimum of 60% RA. The first trough of embrittlement, the so-called first ductility minimum, can be found at elevated temperatures just below the solidus-temperature. This zone is limited by the zero-ductility-temperature (ZDT) down to the area, where the material becomes ductile again. The low ductility is mainly attributed to the presence of liquid residuals, which form interdendritically during solidification. The extension

and the slope of the ductility curve primarily depend on the carbon content and on all alloying elements such as phosphorus, copper, sulfur or boron, contributing to the segregation of low-melting phases along dendrites or grain boundaries, locally decreasing the solidus-temperature. In this way, cracks at the solidification front between the dendrites may be formed, even when a small external force is applied. These give rise to the formation of internal cracks or hot cracks within the cast material. [6], [8], [13]–[15]

The second ductility minimum in the intermediate temperature region roughly between 600°C and 1200°C, however, is generated due to several factors such as the materials chemical composition or thermomechanical history as will be described in the following in more detail. This embrittlement particularly occurs during the straightening or unbending operation and give rise to the formation of transverse surface and corner cracks. [16]–[19]

3.3 Causes for the loss of hot ductility (second ductility minimum)

Principally, the embrittlement within the low temperature region of the austenite phase is caused by grain boundary sliding and becomes even accelerated when fine and dense precipitation occurs, leading to brittle failure via microvoid coalescence. A decrease in ductility may also result by strain concentration within precipitate-free zones or within film-like ferrite being formed along austenite grain boundaries. [6], [20]–[23]

3.3.1 Precipitation-related ductility loss

It is well known, that the grain boundary mobility in austenite is a decisive factor for high-temperature ductility [24]. At lower temperatures and low strain rates, restoration processes such as dynamic recovery or dynamic recrystallization hardly occur. Therefore, the fracture mode is mainly characterized by grain boundary sliding which causes the formation of cavities, such as so-called wedge-type cracks within grain boundary triple-points, even without the presence of intergranular precipitates, Fig. 9 [23], [25].

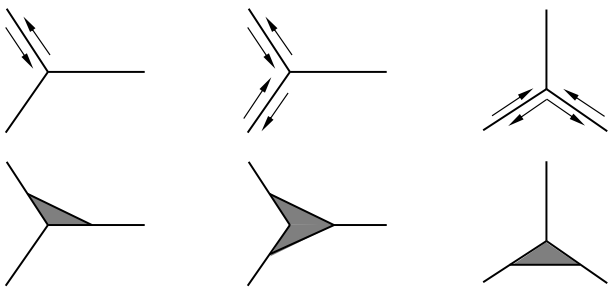

Fig. 9: Schematic models showing wedge-type crack formation. After [25].

Nevertheless, an accelerated embrittlement in many cases takes place when precipitates such as sulfides, carbides, oxides or nitrides are present, favoring cavitation and crack formation e.g. by grain boundary pinning [8], [22]. Within the second ductility minimum, the fracture surfaces of the specimens are characterized by typical intergranular decohesion with fine grain-boundary-covering dimples as exemplary shown in Fig. 10 [26]. This becomes more pronounced as the precipitates size and interparticle spacing become smaller.

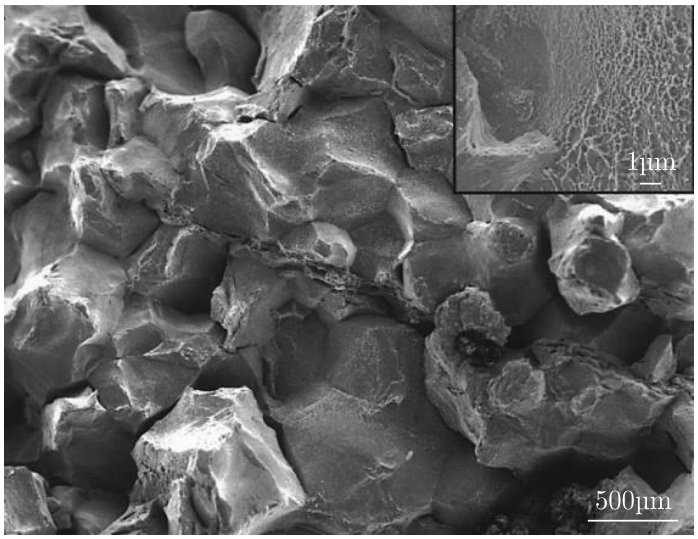

Fig. 10: Fracture surface of a Nb steel tested at 750°C showing intergranular failure [26].

Comparable embrittlement may also occur by the formation of deformation-induced precipitates, such as Nb-carbides in Nb-containing steels [21], [27]. With increasing density of dislocation-pinning precipitates, the density of mobile dislocations becomes thus decreased, which prevents plastic flow in the grain interior relocating the strain to grain boundary regions [28]. Similar effects can be observed when fine matrix precipitation takes place, leading to increased matrix strengthening [22]. Yasumoto et al. [29], for instance, reported an existence of precipitate-free zones (PFZ) along the austenite grain boundaries of 1–1.5µm in width which enhanced strain concentration on grain boundaries. This mechanism has also been observed and well described by Maehara and Ohmori [30] who investigated the hot ductility of low-carbon Nb-Al alloyed steels. Small submicrovoids around a great number of microalloying precipitates with interparticle spacings of 0.2–0.5µm were formed upon deformation and coalesced to microvoids of about 7–12µm in length. Final fracture occurred as the result of microvoid coalescence as schematically illustrated in Fig. 11 [30]. However, the type, shape and size of precipitates as well as the resulting extent of the ductility loss is different and strongly depends on the materials chemical composition and thermomechanical history.

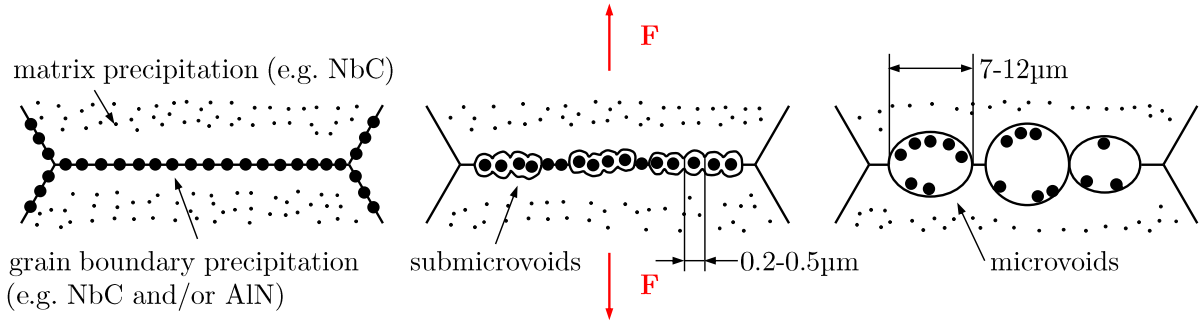

Fig. 11: Schematic representation of grain boundary embrittlement by microvoid coalescence in Nb-microalloyed-steel within the austenitic phase due to PFZ. After [30].

3.3.2 Transformation-related ductility loss

As the temperature further decreases, the embrittlement can be usually linked to the austenite-to-ferrite transition (A_{r3}-temperature) when thin bands of ferrite along the austenite grain boundaries have been formed [22]. Under an applied load, this leads to strain concentration predominantly on the ferrite films which increases as the volume fraction of ferrite decreases since ferrite is softer than austenite [16]. Chimani and Mörwald [31], who used a micromechanical 2D-model by considering the elastic-plastic properties of both ferrite and austenite, suggested that the ferrite fraction should be at least 30% to allow homogeneous stress distribution for plain C–Mn steels at a strain rate of $10^{-2}s^{-1}$, Fig. 12.

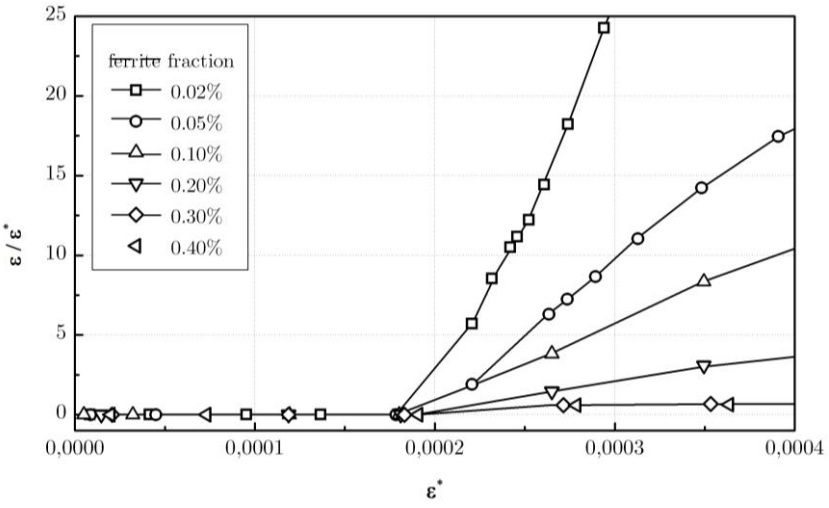

Fig. 12: Diagram presenting the local strain concentration in the ferritic phase (ε) as a function of the global strain (ε^*) plain C–Mn steel at $\dot{\varepsilon}=10^{-2}s^{-1}$ for different ferrite fractions. Based on [31].

According to Lewis at el. [32], the ductility is at a minimum when 5–10% ferrite is present and substantially recovers when more than 50% ferrite has been formed in the

microstructure. Basically, the nucleation rate of ferrite and therefore the development of the second ductility minimum in plain C-Mn steels strongly depend on the carbon content, cooling rate, strain, strain rate and prevailing grain structure [32], [33]. It has also been shown that ferrite can also be formed deformation-induced above the A_{r3}-temperature often close to the equilibrium transformation temperature A_{e3} in both coarse and fine-grained steels [32], [34]–[37]. However, the general course of the ductility trough towards lower testing temperatures is determined by the ferrite growth rate, which, for instance, increases with decreasing grain size. Apart from that, the ductile voiding also depends on particles or precipitates located at grain boundaries (e.g. Mn-sulfides or Al-nitrides) promoting, in turn, intergranular microvoid coalescence, Fig. 13 [22], [30].

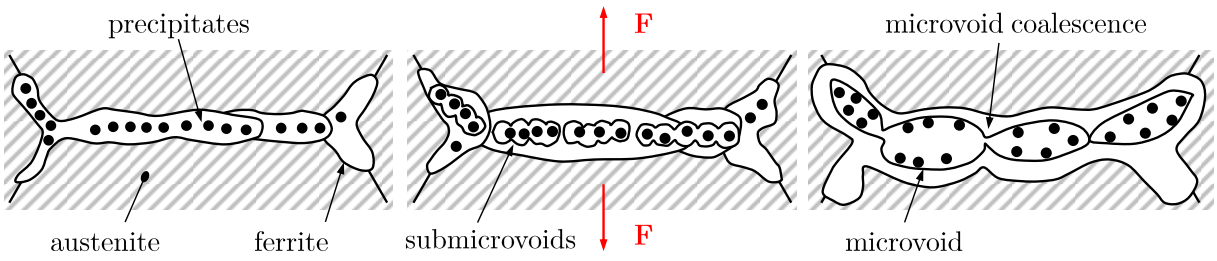

Fig. 13: Schematic representation of grain boundary embrittlement by microvoid coalescence in the two-phase austenite-ferrite region. Based on [30].

3.4 Factors affecting the hot ductility

There are several factors which affect the development of the hot ductility of continuously cast steels. The most important ones are briefly described in the following sections and include the chemical composition, the microstructural conditions as well as the thermomechanical history to which the materials are exposed.

3.4.1 Influence of the chemical composition

This section focuses on some selected elements which are known or suspected to have a great influence on the hot ductility of steels. These are carbon, nitrogen, aluminum, niobium, titanium, manganese as well as sulfur.

3.4.1.1 Carbon

The influence of carbon on the hot ductility and transverse cracking susceptibility of steels has been the subject of numerous research studies [22], [23], [34], [38]–[40]. In conventional

on-heating tests, the obtained development of the ductility trough in plain C–Mn and C–Mn–Al steels with the same grain sizes can be basically related to the austenite-to-ferrite transformation. With increasing C-content, the A_{r3}-temperature and consequently the second ductility minimum are shifted towards lower deformation temperatures as observed by Crowther and Mintz [34] in plain solution treated C–Mn steels, Fig. 14. Maehara et al. [39] even observed no effects of carbon on the hot ductility of C–Mn–Nb–Al steels with C ranging from 0.05 to 0.3% and almost each having Nb of around 0.05-%. Rather, a significant effect of carbon on the austenite grain growth behavior could be noticed, especially in the case of hot tensile tests with prior melting. The austenite grain size strongly depends on the C-content of the steel, which reaches its maximum between 0.1–0.15% C, this being the range at which the investigated steels exhibited distinctive intergranular fracture. This can be attributed to the higher austenite formation temperature in peritectic steels.

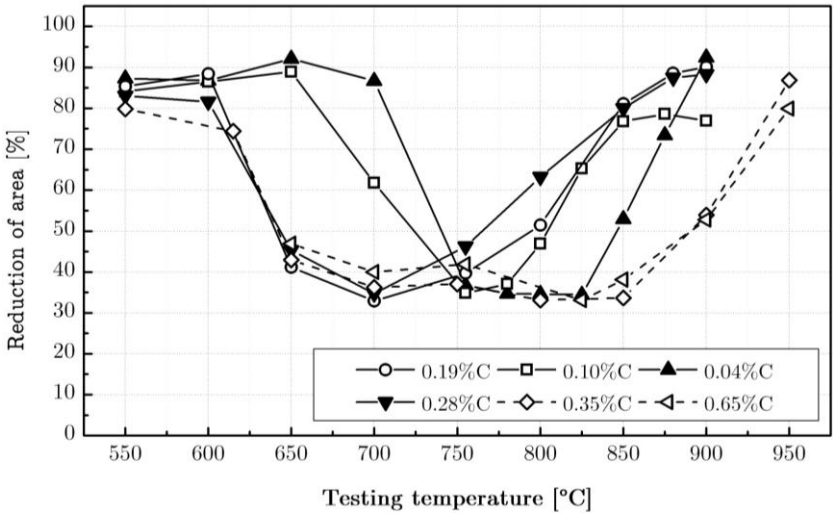

Fig. 14: Influence of the C-content on the hot ductility of plain C–Mn steels. After [34].

Accounting for the peritectic transformation

During the peritectic solidification (Fig. 15), body-centered cubic (bcc) delta-ferrite firstly precipitates from the melt. This results in an enrichment of carbon in the melt due to the lower solubility of carbon in delta-ferrite. With further cooling, face-centered cubic (fcc) austenite starts wrapping the initially formed delta-phase while residual melt still remains. At the same time, carbon diffusion both to the liquid-delta and delta-austenite interface takes place, whereas the carbon-concentration in the former is highest. [41]

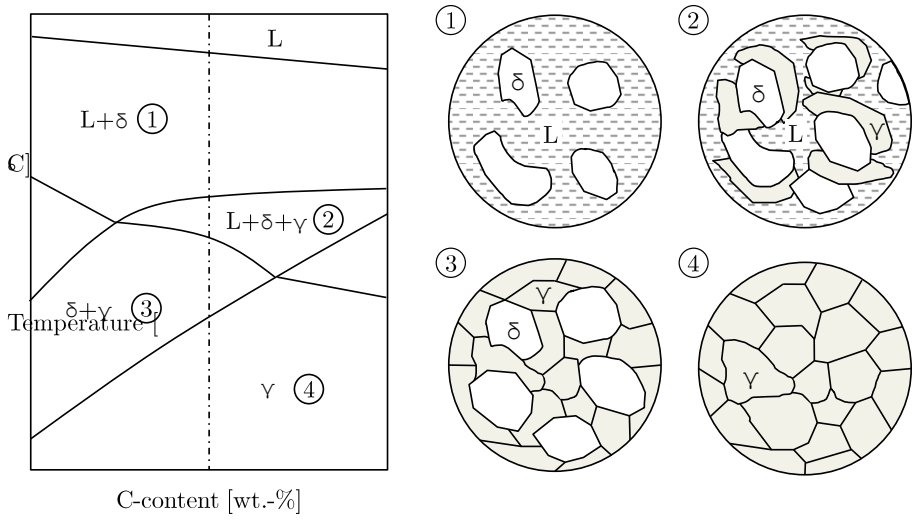

Fig. 15: Schematic illustration of a peritectic reaction in microalloyed steel.

Owing to the different densities and volume contractions of the two solid phases during the delta-to-austenite transformation, an uneven strand shell thickness may develop. The resulting shrinkage stresses and further loss of contact between the shell and mould wall may generate local differences in heat extraction. Consequently, the thinner sections of the inhomogeneously solidified shell are then more susceptible to surface cracking, especially when the carbon content of the steel ranges from 0.08 to 0.17% as shown in the following Fig. 16. Furthermore, the uneven surface solidification produces much coarser and columnar grains, thus accelerating the cracking sensitivity even further. [22], [39], [42]

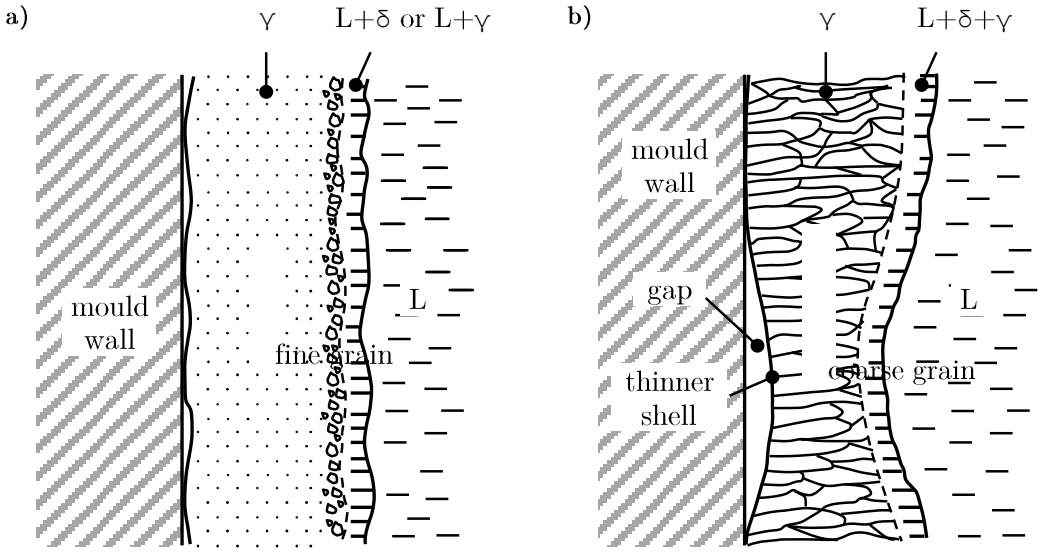

Fig. 16: Solidifying austenite shell structure in a) low or high C and b) medium C steel. Based on [39].

3.4.1.2 Nitrogen

Nitrogen generally decreases the hot ductility in low- and microalloyed steels as soon as fine nitrides and carbonitrides are formed within the matrix and/or at austenite grain boundaries, promoting intergranular fracture [23], [43]–[47]. As reported by Ouchi and Matsumoto [45], an increase of the N-content in C–Mn–Nb steels from 20ppm to 63ppm significantly deteriorates the ductility and shifts the ductility minimum to lower RA-values and higher testing temperatures, Fig. 17. Sricharoenchai et al. [48] have also shown that a higher nitrogen level slightly decreases the ductility minimum in C–Mn–Nb steels. Similar effects can be observed if steels contain other microalloying elements such as Al or Ti which have a high affinity for nitrogen as well. In Al-containing steels, for instance, Al combines with N to form fine AlN-precipitates preferably along austenite grain boundaries, making the cast material more susceptible to transverse cracking as the product of Al and N increases [44], [47]. By contrast, Hannerz [38] noted no or very slight influence of N (0.005 to 0.013%) on the hot ductility of solution treated plain Al-free 0.08%C–1.51%Mn-steels at testing temperatures between 750°C and 900°C, Fig. 18.

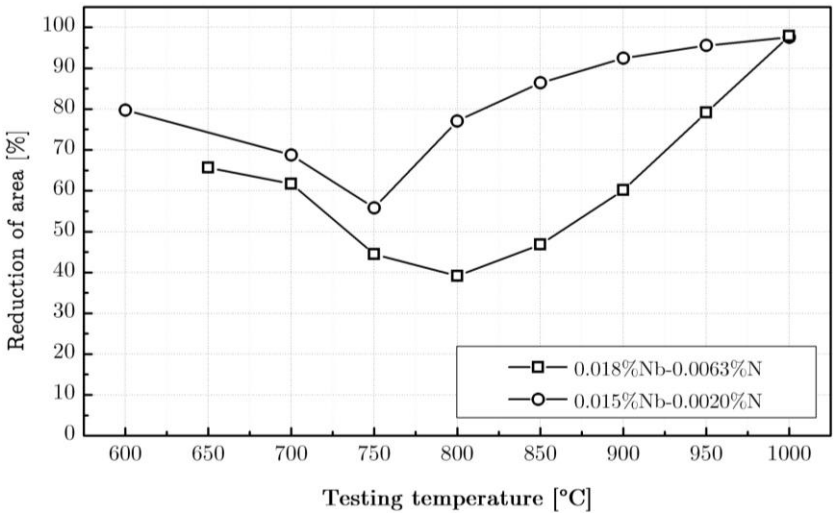

Fig. 17: Influence of the N-content on the hot ductility of Nb-containing steels. After [45].

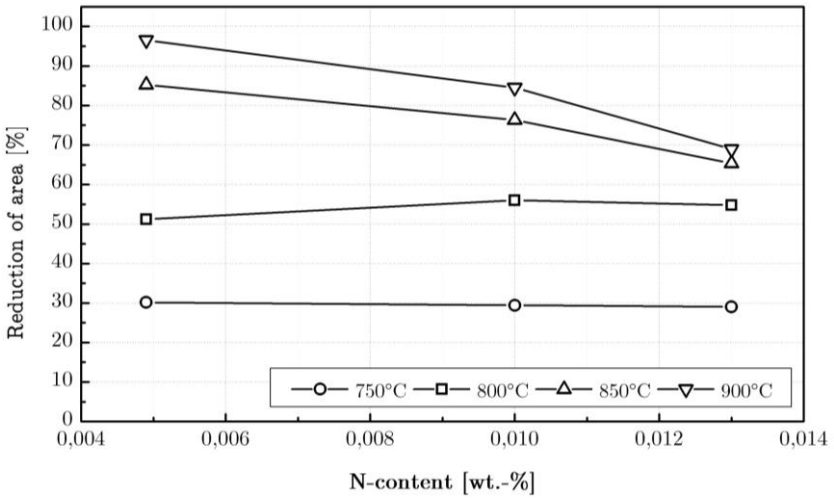

Fig. 18: Influence of the N-content on the hot ductility of Al-free 0.08%C–1.51%Mn steels. After [38].

3.4.1.3 Aluminum

Much research on the detrimental effect of aluminum on the hot ductility of steels exist, as Al tends to combine with N to form fine AlN-precipitates as already stated in the previous section [16], [18], [23], [38], [46], [47], [49]–[52]. An increase of the solubility product of $Al \cdot N$ accelerates AlN-precipitation resulting in broader and wider ductility troughs with a ductility minimum moving to higher testing temperatures as e.g. observed by Hannerz et al. [38] on solution treated (1300°C for 300s) 0.07%C–1.53%Mn steels, Fig. 19.

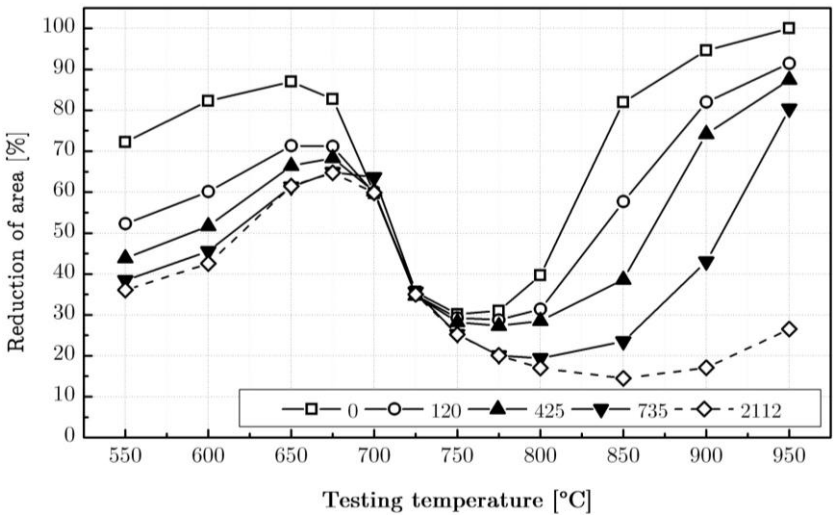

Fig. 19: Influence of the $Al \cdot N$ product ($\cdot 10^6$) on the hot ductility of solution treated C–Mn–Al steels. After [38].

This embrittlement can be attributed to the formation of fine AlN situated at the austenite grain boundaries impeding grain boundary mobility or generating grain boundary microvoids during deformation [38]. Furthermore, melting Al-alloyed steels in-situ can worsen the hot ductility, as this enhances the segregation-factor of Al to grain boundaries promoting an accelerated intergranular AlN precipitation compared to solution treated steels [16], [44].

Fig. 20 shows the ductility curves of in-situ melted 0.1%C–1.4%Mn–Al steels with 65ppm nitrogen and soluble Al ranging from 0.009% to 0.06% at various cooling rates. Here, the highest Al-content ($Al \cdot N = 3.9 \cdot 10^{-4}$ppm) impaired the hot ductility to RA<40% below 900°C. It can be further seen that higher cooling rates were always detrimental to ductility between 800–850°C. However, Pradhan et al. [47] suggest that the $Al \cdot N$ should be less than $3 \cdot 10^{-4}$ppm to avoid transverse cracking.

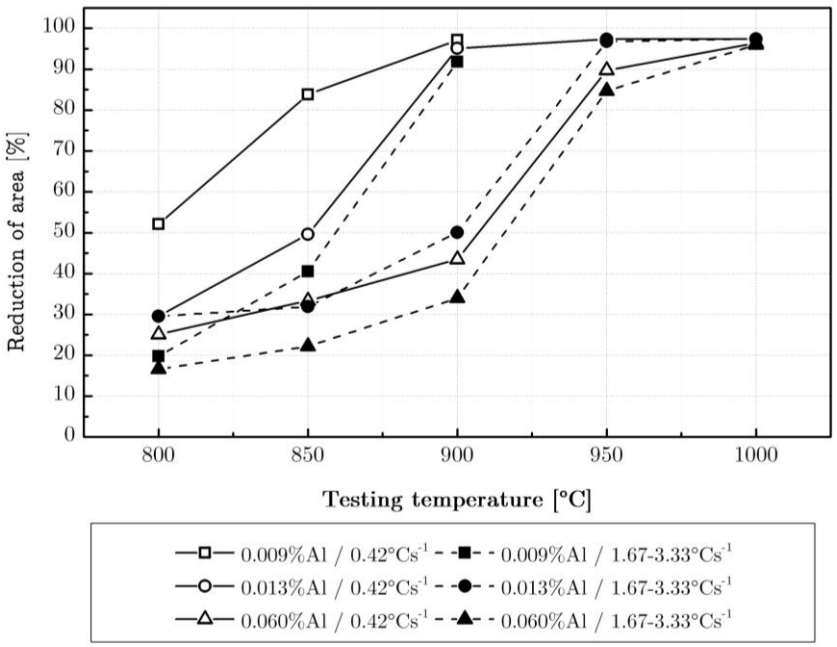

Fig. 20: Hot ductility curves of in-situ melted C–Mn–Al steels with various Al-contents and cooling rates. After [16].

3.4.1.4 Niobium

Niobium is added to steels for its ability to refine austenite grains and increase the materials strength and toughness through precipitation hardening. However, this makes it sometimes difficult to cast these steels without sacrificing quality, since it has often been reported that an addition of niobium tends to deteriorate the hot ductility due to the formation of intergranular Nb-rich precipitates. This leads to the pinning of austenite grain boundaries which becomes more pronounced as the Nb-content increases [38], [45], [48], [53]–[55]. Mintz et al. [56] found that cyclic temperature oscillations on cooling from the solution

treatment resulted in a deepening and widening of the ductility trough on adding 0.035% Nb to a 0.12%C–1.44%Mn–0.015%Al steel. Sricharoenchai et al. [48] also observed a loss in ductility being attributed to fine deformation-induced Nb(CN)-precipitation on solution treated plain 0.085%C steels (Fig. 21a). An addition of 1.56% Mn shifted the minimum to lower testing temperatures. Additional 0.06% Al to this alloy not only deepened but also widened the ductility trough because of its co-precipitation with niobium. Similar mechanisms have been noted by Carpenter et al. [57], who observed reduced ductility when 0.019% Nb was added to a 0.16%C–1.2%Mn–0.015%Ti–0.027%Al steel after melting the specimens in-situ (Fig. 21b). This caused an intense and fine NbTi-precipitation facilitating accelerated intergranular fracture due to the higher total volume fraction of particles compared to steels which either contained only Nb or Ti.

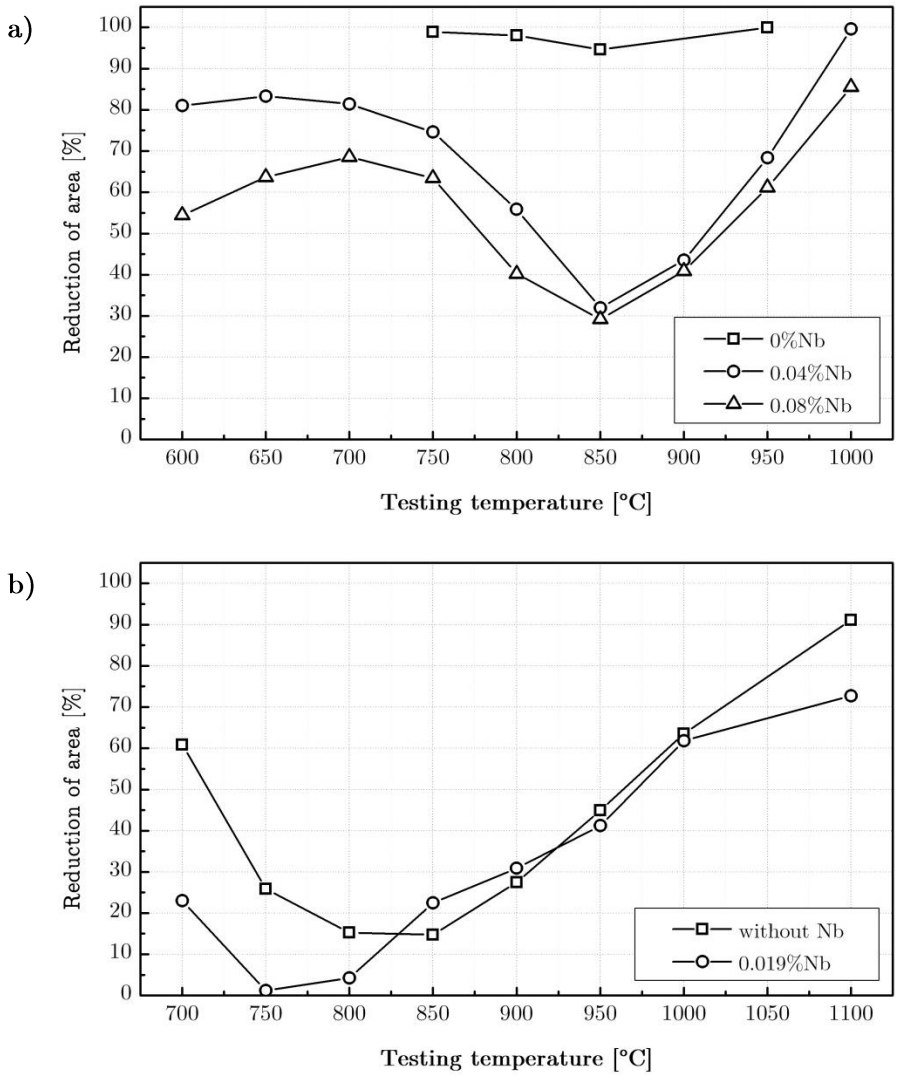

Fig. 21: Influence of Nb on the hot ductility of: a) plain 0.085%C steel after solution treatment at 1300°C for 300s; b) C–Mn–Ti–Al steel after melting and applying a cooling rate of 1.67°Cs^{-1}. After [57].

3.4.1.5 Titanium

The application of titanium as a microalloying element in the crude steel production is gaining increasing importance. Ti, even in very small quantities, may affect the metallurgical and mechanical properties of steels significantly, so that certain processes such as the control of the austenite grain growth, the acceleration or retardation of softening or transformation processes may be directly influenced [58]. During welding for instance, Ti-containing precipitates may contribute to a grain refinement and to an improved charpy impact toughness in the heat-affected zone [16].

Grain refinement through Ti-additions during continuous casting, however, hardly occurs. Rather, titanium unbinds the nitrogen and avoids the formation of Al-nitrides in Al-containing steels. On the one hand, TiN-precipitates are less detrimental to ductility than AlN, and on the other hand, they act as nucleation sites for the deteriorating NbC or Nb(CN)-precipitates in Nb-containing steels. If finer TiN-precipitates than AlN are formed in Ti-containing steels, however, the ductility then becomes worse, regardless of the cooling rate. [22], [59]

Numerous studies on the influence of Ti on the second ductility minimum have already been conducted, but the ductility investigations were not always carried out on in-situ melted and solidified specimens [45], [60]. Considerable improvements of ductility of Ti-containing steels compared to Ti-free samples were mostly observed if they were only heated to a temperature well below the solidus temperature. This effect is due to the fact that the fine grain structure remains even at temperatures above 1300°C, still enabling a good deformability. For a better understanding of the influence of titanium, however, it is of crucial importance to melt the specimen and to dissolve the precipitates before straining. In this way, no grain refinement and almost no improvement in ductility can be observed when the steel is tested after a preceding melting process. [35], [59], [61]–[63]

Abushosha et al. [59], for instance, reported that an addition of Ti to a C–Mn–Al–Nb steel does not recover the hot ductility by melting the samples in-situ and by applying a cooling rate of 1.67°Cs^{-1} by contrast to solution treated steel samples as illustrated in Fig. 22. Only a decrease of the cooling rate resulted in slight improvement in ductility.

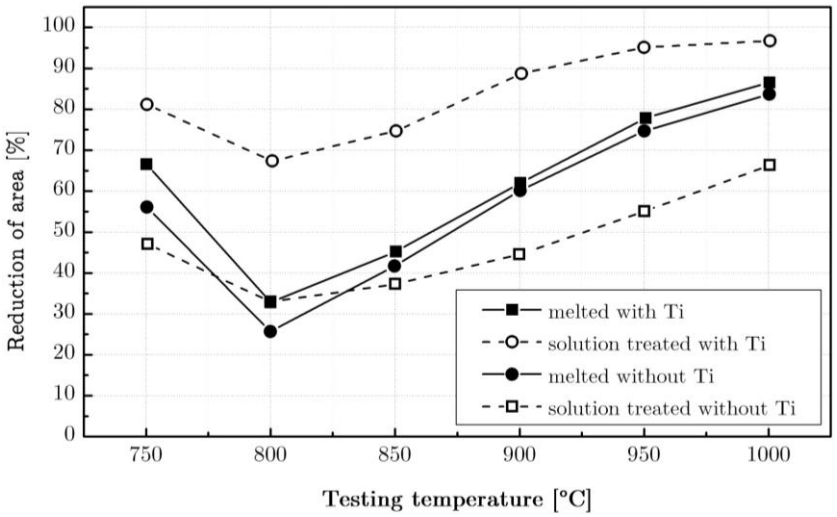

Fig. 22: Influence of Ti on the hot ductility of in-situ melted (solid) and solution treated (dashed) C–Mn–Al–Nb steels by applying a cooling rate of 1.67°Cs^{-1}. After [59].

Similar findings have been confirmed by Abushosha et al. [35] in a later work in which they investigated the hot ductility of in-situ melted C–Mn–Al steels with Ti-additions between 0–0.04% and Ti:N ratios of 0–6.2 in a temperature range between 700°C and 1100°C with different cooling rates (0.42, 1.67 and 3.33°Cs^{-1}). They noted that Ti-additions generally impaired the ductility of the respective steel alloys once finely distributed TiN-precipitates have been created. An increase of the cooling rate from the melting regime to the deformation temperature also resulted in poor ductility, usually leading to the formation of fine AlN- as well as MnS-particles along grain boundaries. Accordingly, additions of Ti may not contribute to a remarkable increase in ductility, particularly during the thin-slab casting process with higher cooling rates.

Comineli et al. [62] examined the effect of Ti on the ductility of melted C–Mn–Nb–Al steels and observed in the following two cases an improvement of the ductility below the testing temperature of 950°C compared to Ti-free steels:

- Steel with 0.014% Ti and 0.004% N having a Ti:N ratio of 3.5:1 and the lowest product of Ti and N of $0.56 \cdot 10^{-4}$ for all cooling rates (0.42, 1.67 and 3.33°Cs^{-1}).
- Steel with 0.045% Ti and 0.0056% N having the highest Ti:N ratio of 8.04:1 for all cooling rates.

The steel with 0.034% and 0.011%Ti with the highest Ti · N product of $3.74 \cdot 10^{-4}$ as well as the steel with 0.02%Ti with the same N content and a Ti · N product of $2 \cdot 10^{-4}$ showed a slight increase in ductility only between 900°C and 950°C by utilizing a cooling rate of

0.42°Cs^{-1}. Spradbery et al. [64] investigated the influence of undercooling on the hot ductility of C–Mn–Al and C–Mn–Al–Nb steels both with and without Ti (N-content~0.005%), Fig. 23.

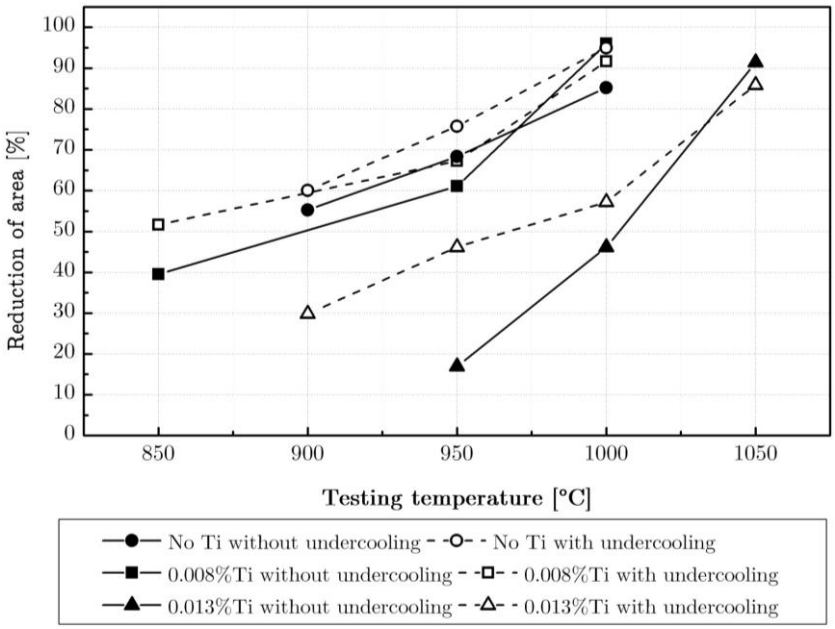

Fig. 23: Influence of the Ti-content on the hot ductility of Nb-containing steels with and without an undercooling step. After [64].

A direct cooling with 1.67°Cs^{-1} as well as using an additional undercooling step of 100°C before straining resulted both in worse ductility behavior compared to steels having no Ti.

Banks et al. [65] observed a significant increase in ductility of Ti-containing 0.04%C–1.6%Mn–Nb steels at deformation temperatures ranging from 800°C to 1000°C, whereas the samples were subjected to similar thermal histories as the slabs exposed during continuous casting. Hence, the specimens were first melted at 1500°C, rapidly cooled with 10°Cs^{-1} to 950°C, then reheated to 1050°C, further slowly cooled with 0.2°Cs^{-1} to testing temperature and finally pulled to fracture at $3 \cdot 10^{-3}$s^{-1}. For comparison, hot tensile tests on samples after normal cooling were conducted as well. Steels with Ti-additions exposed to a normal cooling procedure indicated worse RA-values compared to the same alloys having no Ti, whereas, on the other hand, a thermal pattern similar to continuous casting contributed to an improvement of the ductility of C–Mn–Nb–Ti steels below 900°C.

3.4.1.6 Manganese and sulfur

The influence of sulfur on the hot ductility is one among the most investigated topics, since it has been well known to induce grain boundary weakening particularly at higher testing temperatures [8], [14], [29], [38], [66]–[69]. This occurs through the segregation of S to

grain boundaries, through the formation of low-melting phases such as FeS or by combining with Mn to form MnS- or FeMnS-inclusions preferably at austenite grain boundaries [12], [22], [29], [70], [71]. It has been found, that generally increasing the S-level both deepens and widens the ductility trough as illustrated in Fig. 24 from the work of Weinberg [67].

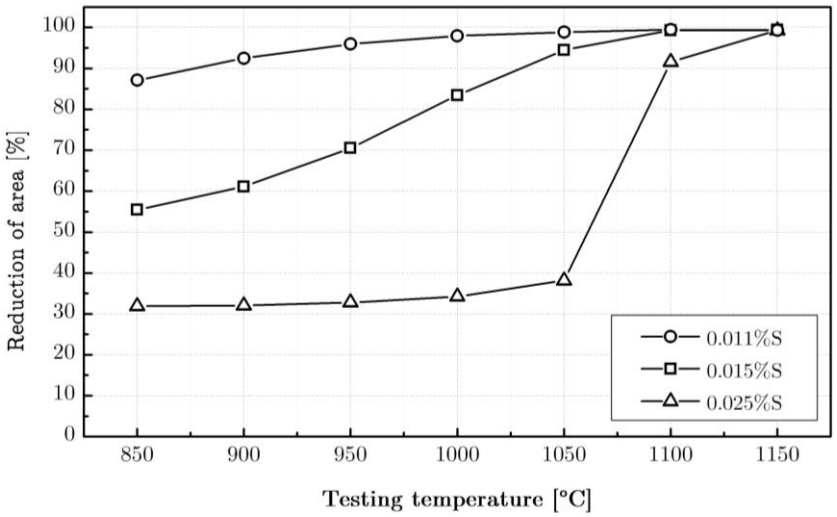

Fig. 24: Influence of the S-content on the hot ductility of plain 0.04–0.06%C steels [69]. Based on [67].

Cowley et al. [72] reported no detrimental effect of S on the hot ductility of solution treated C–Mn–Al steels. However, these observations were reversed once the specimens have been melted in-situ due to a high level of segregation, producing a greater amount of sulfides at the austenite grain boundaries on cooling. Apart from that, much research focuses on the influence of Mn together with S and on the importance of the Mn:S ratio on the hot ductility of continuously cast steels [8], [22], [29], [66]. Basically, high Mn:S ratios and low amounts of S have been considered to prevent embrittlement [69], [71]. Suzuki et al. [12] have found that not only the Mn:S ratio, but also the absolute values of Mn and S are of crucial importance. If the S-content is less than 0.006% and Mn higher than 0.7%, no brittle fracture is expected, even if the Mn:S is small [12]. Fig. 25 presents their results on low-carbon (C<0.3wt.-%) steels in a temperature range between 900°C and 1200°C at a cooling rate of 20°Cs^{-1} after melting and utilizing a strain rate of 5s^{-1}.

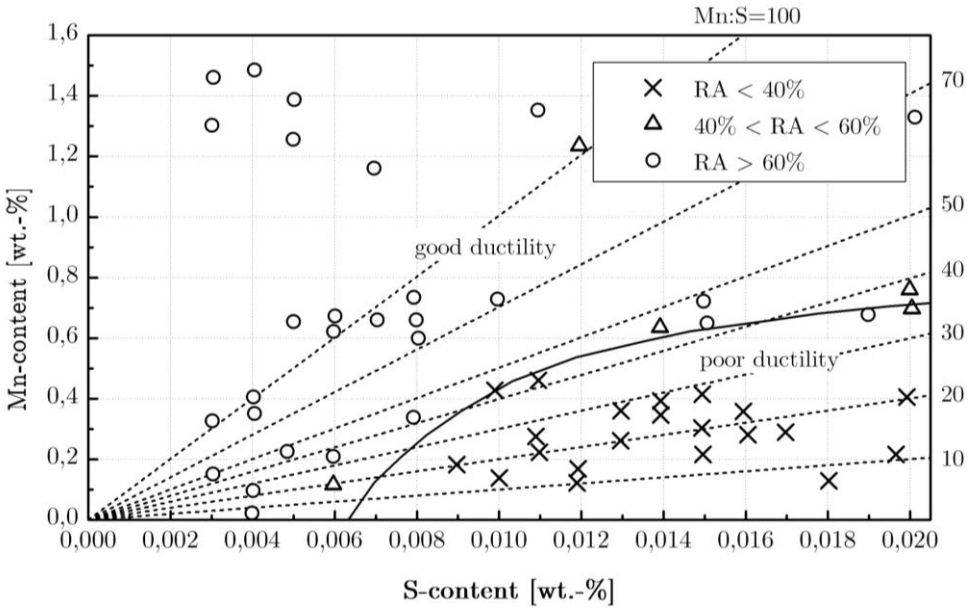

Fig. 25: Influence of the Mn- and S-content on the hot ductility of melted low C–steels in the temperature range between 900–1200°C at a strain rate of $5s^{-1}$. Modified after [12].

3.4.2 Influence of the grain size

Refining the grain size is generally found to be beneficial to the hot ductility of steels, provided that no precipitation is present [73], [74]. Crowther and Mintz [73] noted that a grain refinement on solution treated plain 0.19%C–1.5%Mn steels led to reductions both in the width as well as in the depth of the ductility trough as presented in Fig. 26.

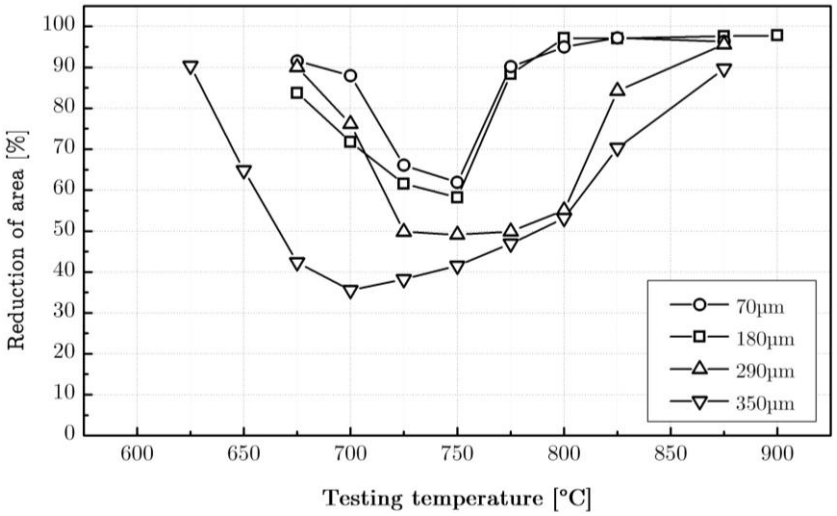

Fig. 26: Influence of various grain sizes on the hot ductility of plain 0.19%C–1.5%Mn steels. Based on [73].

Basically, the brittle fracture in coarse-grained steels can be attributed to the fact that large individual cracks are able to develop and less number of triple-points and grain edges exist to act as barriers for crack propagation [75]. By contrast, in the case of microalloyed steels, others have reported that the grain size had no or slight influence on the hot ductility once fine precipitation has taken place, overriding the effect of grain refinement [45], [74].

3.4.3 Influence of the thermomechanical history

As already stated in subchapter 3.2, hot tensile tests are commonly used to assess the hot ductility and the likelihood to cracking under varying thermomechanical and microstructural conditions, respectively. Tensile specimens are heated to desired testing temperatures after being exposed to respective thermal histories using either inductive [15], [63], [76]–[79], conductive [14], [80]–[83] or, more rarely, radiative heating [84]. According to Fig. 27, the heating cycles can be basically divided into 3 categories [6]:

a. Direct heating method: Specimens are directly heated to test temperature and pulled to fracture after a defined holding time.
b. Solution treatment: Specimens are heated below the materials solidus-temperature (T_S), cooled to test temperature and subsequently pulled to fracture.
c. In-situ melting: Specimens are heated above T_S and appropriately melted, subsequently cooled to test temperature and pulled to fracture.

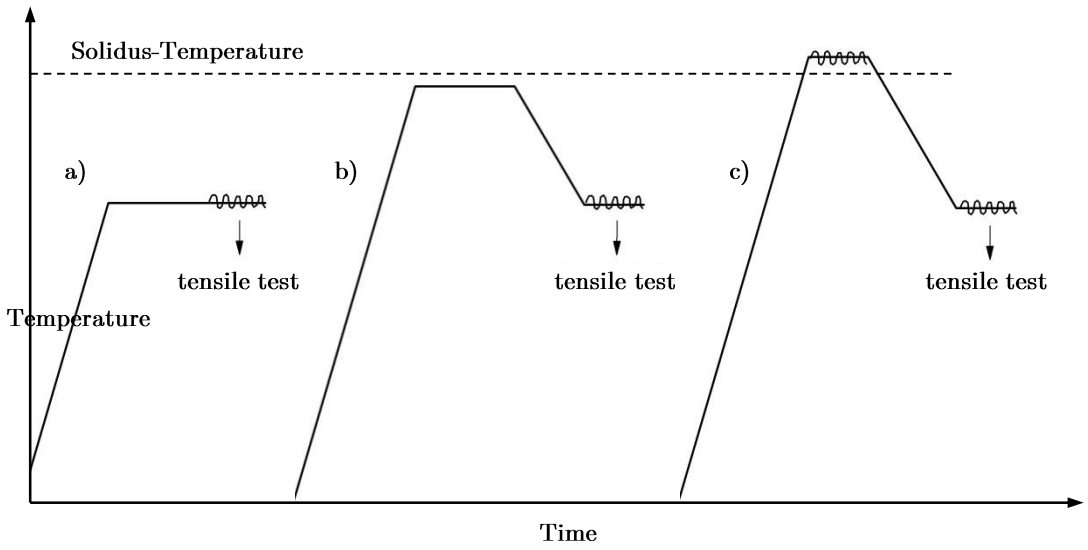

Fig. 27: Schematic diagrams of thermomechanical histories for evaluating the hot ductility of steels.

In contrast to conventional hot tensile testing techniques (cycles a and b), the in-situ melting method (cycle c) facilitates a reproduction of coarse as-cast microstructures by taking into account the effects of solidification. This considers the segregation of alloying elements at grain boundaries and allows the dissolution of certain particles such as Ti-containing precipitates or MnS within the two-phase solid-liquid region. [65], [85], [86]

The following sections briefly describe the essential experimental variables including strain rate, cooling rate and thermal treatment, which can significantly affect the hot ductility behavior of steels during tensile testing.

3.4.3.1 Influence of the strain rate

Basically, the strain rates during continuous slab or bloom casting for thicknesses of at least 200mm are believed to be $10^{-3}s^{-1}$ to $10^{-4}s^{-1}$ using the equations presented in section 3.1.1. For thin slab casting, the strain rates may be up to one order of magnitude higher ($10^{-2}s^{-1}$). Increasing the strain rate has been generally found to improve the hot ductility of microalloyed and low-alloyed steels within the ductility trough, often being characterized by a gradually change of the fracture mode from transgranular to intergranular failure [14], [22], [23], [45], [87]–[89]. Fig. 28 shows the increasing RA-values of various solution-treated microalloyed steels with increasing strain rate at a testing temperature of 800°C [90].

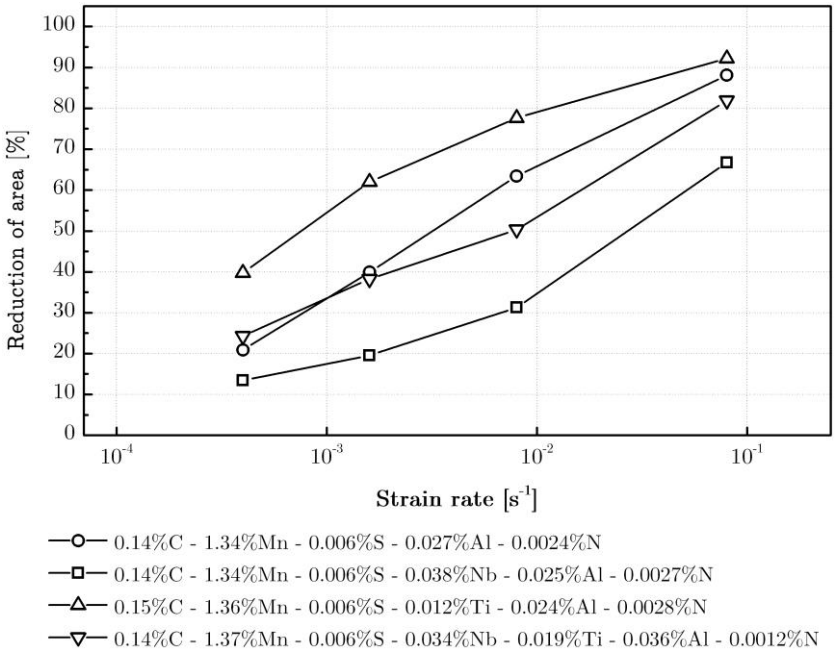

Fig. 28: Influence of the strain rate on the hot ductility of microalloyed steels solution treated at 1300°C for 10min and deformed at 800°C. After [90].

According to references [22] and [91], several mechanisms have been stated to explain the ductility improvement at higher strain rates:

- Insufficient time is available for deformation-induced precipitation as well as for the formation of deformation-induced ferrite.
- Limited grain boundary sliding.
- Insufficient time for the formation and growth of voids next to precipitates or inclusions along grain boundaries.
- An increase of the strain rate allows recovery in the ferrite band by work hardening. This decreases the strength-difference of ferrite and austenite and counteracts localized strain concentration within thin ferrite bands.

Worth mentioning are possible contrary effects of precipitation during deformation. Yasumoto et al. [29], for instance, reported a decrease in hot ductility in 0.05%C–Mn–Al steels when the strain rate was increased from $10^{-2}s^{-1}$ to $10^{-1}s^{-1}$. They suggested that the slower strain rate promoted a coarsening of intergranular Fe-rich FeMn-sulfides and thus decreased the degree of grain boundary pinning [22], [29].

3.4.3.2 Influence of the cooling rate

Depending on the chemical composition, reducing the cooling rate has been generally found to improve the materials hot ductility as reported in numerous research studies [29], [35], [46], [81], [92]. It is noted, that a slower cooling rate encourages the coarsening of precipitates and increases the interparticle spacing [93]. This diminishes the dispersion of fine and dense precipitation and therefore suppresses the formation and coalescence of microvoids during deformation. Fig. 29 illustrates the deterioration of the hot ductility of in-situ melted Ti-containing 0.1%C–1.4%Mn–Al steels (Ti:N ratio=3.4) with increasing cooling rates from $0.42°Cs^{-1}$ to $3.33°Cs^{-1}$ [35]. Similar observations have been obtained by Abushosha et al. [46] on both as-cast C–Mn–Nb–Al and C–Mn–Al steels with the same varying cooling rates.

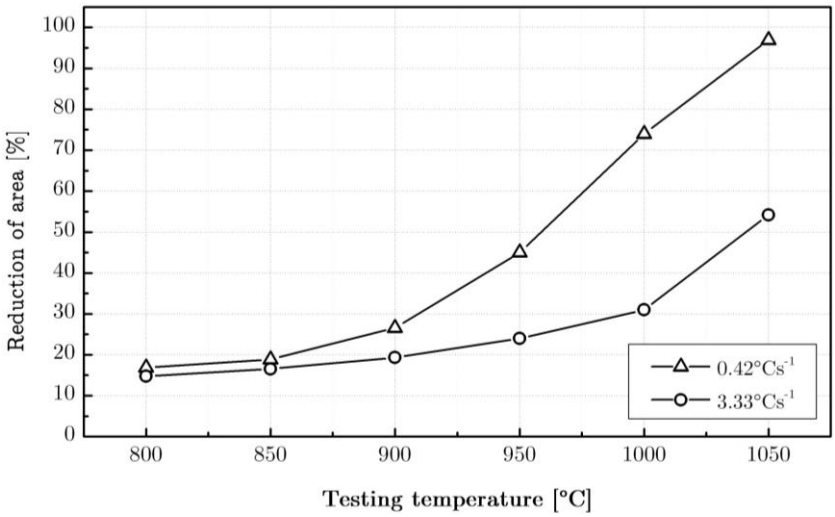

Fig. 29: Influence of the cooling rate on the hot ductility of in-situ melted C–Mn–Al–Ti steels. Bases on [35].

3.4.3.3 Influence of the thermal treatment

The oversimplified cooling patterns presented in Fig. 27 may not adequately represent the thermal cycle experienced by the slab surface during continuous casting. Therefore, improved thermal treatments as close to industrial practice are of great importance to simulate the effects of undercooling and thermal oscillations on the hot ductility of steels. The causes for the embrittlement at the second ductility minimum have been strongly related to the formation of small ferrite bands surrounding the austenite grains, once an average direct on-cooling from the austenitic regime to around γ-α transformation start temperatures has been applied. One of the promising approaches to successfully overcome this problem has been developed by Kato et al. [94] by applying a surface structure control cooling method, Fig. 30.

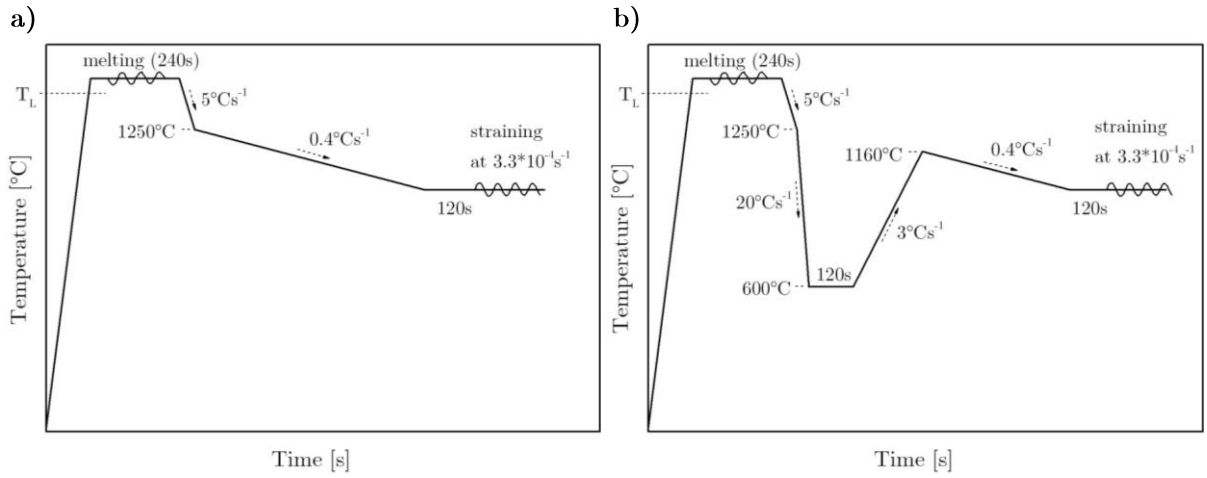

Fig. 30: a) Mild cooling and b) Surface structure control cooling (SSCC) process [94].

This concept causes the suppression of film-like intergranular ferrite by rapidly cooling the specimens well below the A_{r3}-temperature followed by a reheating to the austenite region giving rise to both homogeneous ferrite and precipitates distribution throughout the microstructure. It can be seen from Fig. 31 that the SSCC causes the hot ductility to fully recover over the whole testing temperature range compared to the conventional direct on-cooling (mild cooling, Fig. 30b) method.

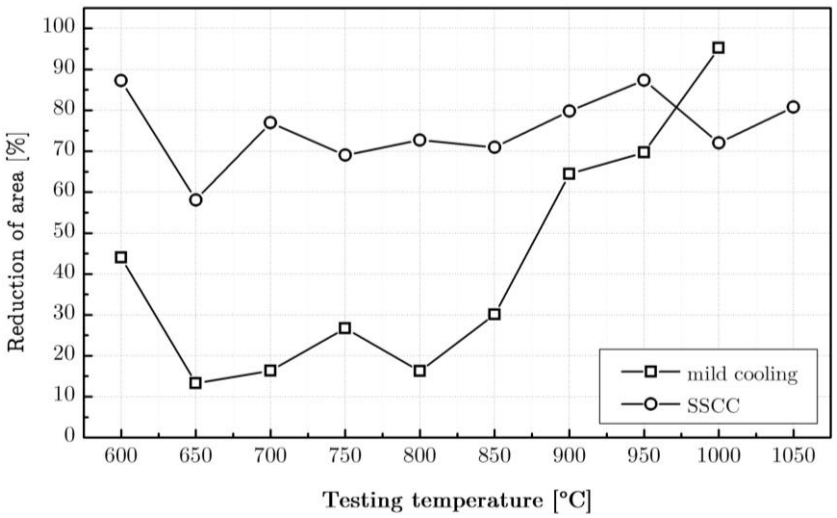

Fig. 31: Influence of SSCC on the hot ductility of in-situ melted 0.07%C–1.5%Mn–0.02%Nb–0.02%Al–0.01%Ti steels. After [94].

Several other studies have been also published dealing with the influence of various thermal histories on the hot ductility and are partly contradictory. It has often been reported that complex temperature oscillations give rise to poor ductility due to an increased amount of fine precipitation with greater particles volume fractions [22], [80], [92]. Mintz et al. [56] have reported a broadening and deepening of the ductility trough for solution-treated C–Mn–Nb–Al steels by utilizing temperature oscillations on cooling due to precipitation of NbCN. This has become even worse when the amplitudes of the temperature oscillations further increased. Spradbery and Mintz [64] have shown that introducing an undercooling step of 100°C below the testing temperature for as-cast C–Mn–Al and C–Mn–Al–Ti (Ti:N less than the stoichiometric ratio of 3.42:1) steels resulted in worse ductility. On the other hand, Carpenter et al. [57] observed an improved ductility in Nb- and Ti-bearing microalloyed steels by simulating the thermomechanical history of the near-surface regions of continuously cast steels in laboratory hot tensile tests. They concluded in their work that the respective thermal cycles promoted the coarsening of NbTi(CN)-precipitates compared to the observations during simple cooling treatment without introducing any thermal oscillations.

4 Experiments

This chapter of the work presents the investigated materials and testing equipment which have been used to examine the hot ductility behavior during selected thermomechanical histories. Following this, microstructural testing and simulation methods are introduced for materials characterization.

4.1 Investigated materials

Two low-alloyed steels from the voestalpine Stahl Linz GmbH, one of them additionally microalloyed with Ti and Nb, were chosen to be investigated in the present work. The chemical compositions in wt.-% are given in Table 1, whereas the respective indicated designations "A15" and "44A6" are only internally in use. Both steel grades were delivered in the as-cast and normalized condition from a continuously cast slab.

Table 1: Chemical composition of the investigated steels (wt.-%).

Steel	C	Si	Mn	P	S	Cr	Ni	Ti	Nb	Al	N
A15	0.158	0.013	1.10	0.0094	0.006	0.034	0.011	0.001	0.002	0.041	0.0036
44A6	0.063	0.025	1.93	0.0088	0.001	0.041	0.038	0.129	0.048	0.054	0.0070

Cylindrical tensile specimens of 160mm in length and 19.5mm in diameter were machined from the peripheral regions of the cast slab with their longitudinal axes being parallel to the casting direction, Fig. 32.

Owing to the inductive heat input and the resulting uneven thermal gradient along the longitudinal direction, it often occurs that the specimen does not break in the central reference point during hot tensile testing [95]. This happens, for instance, if ferrite and austenite are concurrently present, with the former being the softer phase at which strain concentration will take place. For this reason, the samples were then turned to the specific shape, as shown below, with a curved narrowing in the middle of 15mm in diameter at which the fracture should occur and of 40mm in length which was also taken as the gauge length for strain rate calculations.

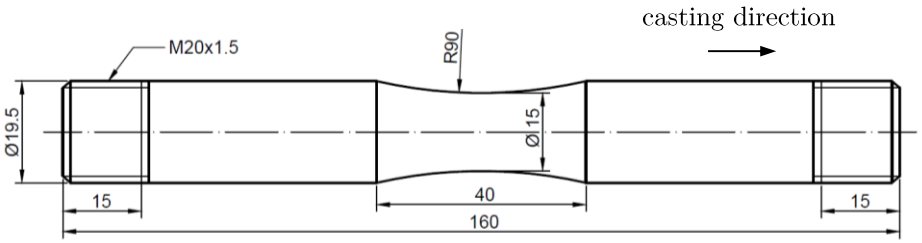

Fig. 32: Specimen geometry and dimension in mm.

4.2 Testing equipment

This section gives an overview of the thermomechanical testing machine BETA 250-5 including a brief description of the melting procedure, a presentation of the quenching system and the experimental setup for hot tensile tests.

4.2.1 Hot tensile testing machine BETA 250-5

The experimental apparatus BETA 250-5 is a vertical thermomechanical tensile testing machine as shown in Fig. 33. The power transmission is carried out via a ball screw drive supporting a maximum nominal force of 250kN including a load cell according to DIN 51220 Class I [96]. Furthermore, the machine is equipped with a 12kW inductive heating unit consisting of an automatic resonance frequency recognition system supplied by the company iew GmbH and a fixed five-turn copper coil inductor with an inner diameter of 30mm and a length of 50mm. The vacuum recipient is connected via an electropneumatic angle valve to a Pfeiffer rotary vane pump Duo 065 D for producing fine-vacuum and a Leybold-Heraeus turbo molecular pump TURBOVAC 1500 for high-vacuum. There is also the possibility to directly connect the chamber to an inert gas cylinder such as argon or helium. Apart from that, the chamber door is equipped with two viewing windows which provide the use of additional contactless measuring devices such as pyrometers or high-speed cameras. The required temperature measurement for the heating control can be either performed by a thermocouple or optionally by a pyrometer. The output signal of the respective temperature measuring sensor is captured by a controller Eurotherm2704 which sends the feedback signal to the frequency-generator. An electronic controller EDC100, on the other hand, controls the ball screw drive and is simultaneously measuring the actual crosshead travel and force value which can be directly displayed on its front panel or on a PC. Both controllers are connected via a serial port to a PC where the target values such as temperature and crosshead speed

can be programmed. For defining specific thermomechanical test sequences, the application software by Messphysik Materials Testing GmbH (version 2.20.00) has to be used. Important quantities including temperature, heating power, vacuum pressure, crosshead travel and force are displayed both at the operating and control cabinet beside the recipient as well as on the PC. [96]

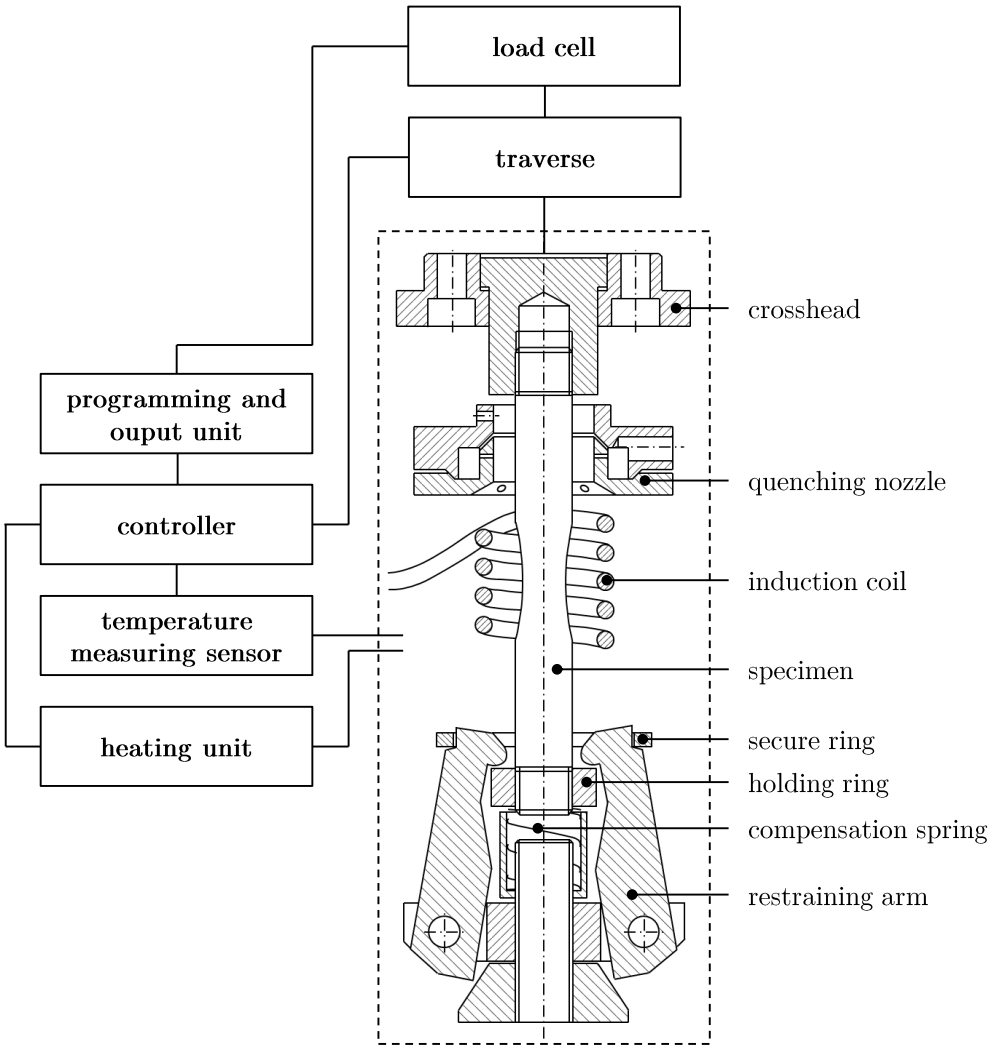

Fig. 33: Schematic illustration of BETA 250-5.

A particular feature of the testing machine is its ability to melt the samples in-situ without using any protective covering such as quartz tubes [59], [97]. By means of a fine-vacuum pressure usually of 0.2mbar and the inductive heat input, it is feasible to form a stable oxide layer supporting a liquid pool inside the specimen. Residual oxygen proportions in the chamber cause a slight surface oxidation and an additional surface convection, hence showing a temperature profile which increases from the outside towards the inside of the specimen. Thus, a thin solid layer can be produced, preventing the liquid fraction of about 10mm in length from breaking out. Additionally, the carbon content in the oxidized shell is

lower than the overall alloy, whereby it can be overheated while the center of the specimen already starts to melt. A further advantage is that a thermocouple for an accurate surface temperature measurement can be used throughout the whole process. [98]

4.2.1.1 Melting procedure

The melting parameters for low- and micro-alloyed steels can be determined in two different ways. On the one hand by the temperature-controlled heating and on the other hand by the so-called heat-input-controlled heating method, whereas the latter modified process has proved to be a more successful approach as will be described in the following.

Temperature-controlled melting

In order to determine the alloy-dependent melting parameters, the specimens are first heated to 1400°C and further to a specific peak temperature T_m with $1°Cs^{-1}$ at which the samples are hold for at least 60s. The procedure has to be repeated and T_m varied until a clear liquid pool can be observed by quickly pulling the samples to fracture immediately after the holding time[2].

Heat-input-controlled melting

Recent observations have shown that slight deviations both in vacuum-pressure and peak temperature may strongly influence the melting procedure for certain steel grades, thus initiating an uneven surface oxidation and thermal radiation and accordingly an overheating of the inductive heating system. Consequently, this overshooting of the heat-input often caused a breakout of the melt and therefore led to an increased test failure rate. However, a repeatable melting process is maintained if a constant heating power is kept at a relevant high temperature regime. Hence, extensions on the programming software with an additional command for entering controlled power-output values between 0-100% were carried out in order to switch from the automatic to the manual heat-input mode for a certain time period. The melting parameters can be accordingly determined following the same temperature-controlled heating phase to 1400°C and further heating with a specific power-output for at least 120s. Again, the procedure has to be repeated and the power-output varied until a clear

[2] 1400°C is derived from experience for peritectic and low/micro-alloyed steel grades which may possibly be reduced for e.g. high-carbon steels, since the incipient melting temperature mostly depends on the carbon-content and other alloying elements (e.g. boron).

liquid pool can be observed by pulling the samples upon holding the power-output for the appropriate time. After the melting process, the system has to be switched back to the automatic mode to continue with the defined thermal schedule on cooling.

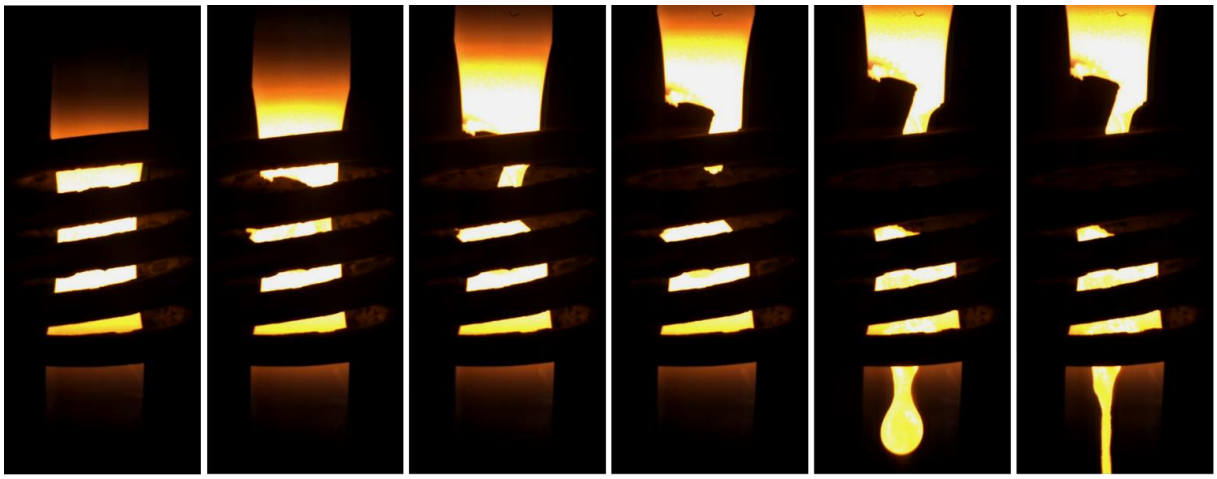

Fig. 34: Specimen pulled immediately after the end of the heat-input controlled melting showing a dropping melt and the formed oxide layer on the upper specimen part; Ti-Nb alloyed steel, used power-output: 25% for 120s.

4.2.1.2 Quenching system

The possibility of specimen quenching at any desired time and temperature on the BETA 250-5 was one of the main tasks of the current research project and has been recently realized through water-spray cooling [99]. For this purpose, the high-flow quenching unit (HFQU) from Gleeble® systems must be used. In order to ensure full quenching, water is pressurized up to 300kPa and sprayed via a specially constructed quenching ring nozzle onto the hot sample surface. The ring is equipped with diagonally directed main nozzles towards the lower specimen part and additional vertical side nozzles directed to the upper specimen part. This enables sufficient heat removal from the whole specimen volume, which is especially necessary for the quenching of partially strained and unstrained specimens. Before executing water-quenching experiments, however, the chamber has to be flooded with inert gas followed by a disconnection of the vacuum unit, respectively. The flooding itself takes about 60s and is usually carried out during cooling after the melting or holding process. Once atmospheric pressure is being reached, the quenching is initiated manually until all the water is drained out of the HFQU (filling capacity: 2.5l). Depending on the peak temperature, the possible mean cooling rates down to 100°C on the standard BETA-specimens were measured to be about 100–200°Cs^{-1}.

4.2.1.3 Experimental setup

One end of the specimen has to be screwed into the upper crosshead while the lower end has to be clamped on a special restraining system as already illustrated in Fig. 33. This unit is equipped with a steel spring and three gripper arms, compensating thermal expansions downwards and holding the sample when pulling it upwards. A type S (Pt/Pt-Rh) thermocouple has to be spot-welded to the sample-center to control and measure the surface temperature during the whole thermomechanical treatment. The crosshead speed v for a given strain rate ε has to be determined beforehand by the following formula:

$$\dot{\varepsilon} \cdot L = v, \tag{1. 5}$$

where L denotes the gauge length of the tensile specimen with 40mm.

Hot ductility evaluation

The hot ductility behavior of the steel specimens is evaluated by constructing hot ductility curves by the reduction of area after fracture in percent (RA) as a function of deformation temperature, which is basically defined as

$$RA = \left(1 - \frac{A_f}{A_0}\right) \cdot 100\ [\%], \tag{1. 6}$$

where A_0 is the initial cross section of the specimen and A_f the cross section after fracture. Since the formation of solidification shrinkages due to the melting process cannot be avoided, it is necessary to subtract the respective areas both from the load-bearing initial cross section as well as from the cross section after fracture, Fig. 35.

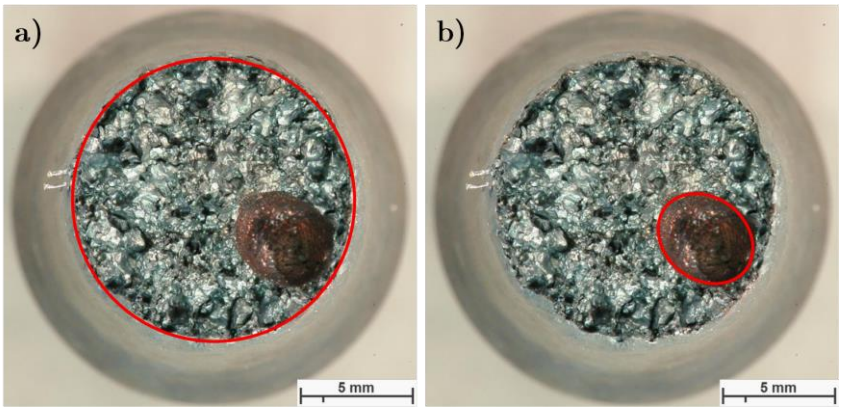

Fig. 35: Graphical evaluation of a) cross section after fracture and b) shrinkage cavity.

Thus, both areas in (1. 6) can be expressed as follows:

A_f = cross section after fracture – solidification cavities (1. 7)

A_0 = initial cross section – solidification cavities (1. 8)

The cross section after fracture and the solidification cavities are determined graphically applying the image-processing software ImageJ [100]. For each thermomechanical treatment and test temperature, at least one valid RA-value is taken for the ductility evaluations. Moreover, the software-package is also used to measure the mean grain diameter of quenched specimens.

4.3 Thermomechanical histories for hot ductility investigations

This subchapter contains detailed information regarding the performed hot ductility investigations. First, direct on-cooling tests on both steel alloys are presented, followed by additional hot ductility tests for the Ti-Nb alloyed steel including solution treatment, slow cooling and surface structure control cooling experiments.

4.3.1 Direct on-cooling tests – Low- and Ti-Nb microalloyed steel

Hot ductility investigations were carried out on both low-alloyed and Ti-Nb microalloyed steels which were subjected to in-situ melting and solidification and directly cooled to deformation temperature as illustrated in Fig. 36. First, the specimens were heated to 1300°C at 10°Cs^{-1} and further to 1400°C at 5°Cs^{-1} followed by a melting process for at least 60s. The peak temperature for the low-alloyed steel was found to be at 1440°C by applying the temperature-controlled melting method, whereas the heat-input controlled melting was conducted for the Ti-Nb steel as described in chapter 4.2.1.1. Here, the minimum resulting peak temperature was found to be at 1460°C. After melting, the specimens were cooled to 1250°C at 5°Cs^{-1} and subsequently cooled at 1°Cs^{-1} to testing temperatures between 650°C and 1000°C. After a short holding time of 10s, the specimens were then pulled to fracture using a strain rate of 10^{-3}s^{-1}.

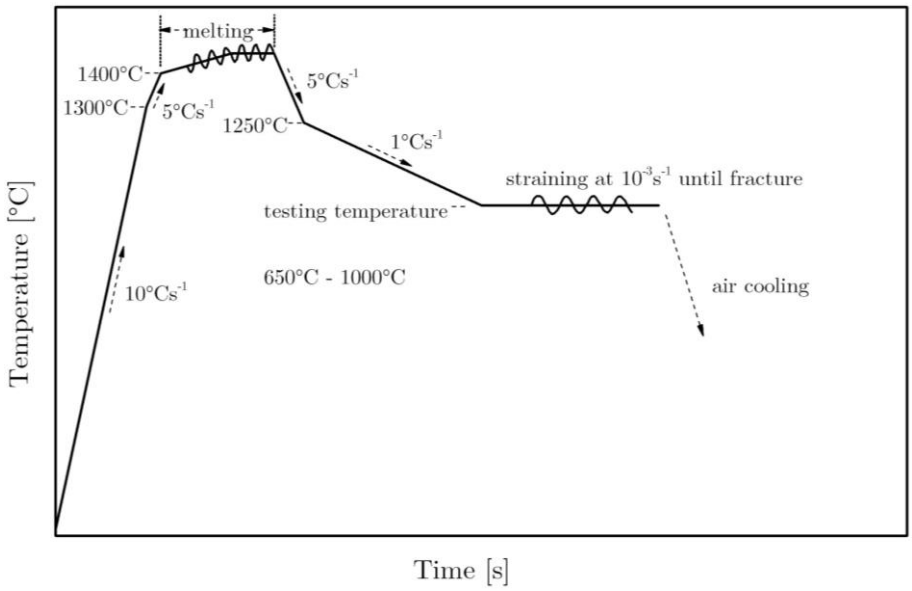

Fig. 36: Schematic illustration of direct on-cooling cycle for low- and Ti-Nb alloyed steel.

4.3.1.1 Selected quenching experiments

Selected quenching experiments using the HFQU-system have been further performed on both steel alloys for subsequent microstructural examinations.

Low-alloyed steel

Water-quenching experiments on the low-alloyed steel at selected testing temperatures were performed in order to freeze the microstructure for further metallographic investigations. This include the quenching at 700°C, 750°C and 800°C both after a holding period of 20s without straining and immediately after pulling the specimens until fracture, Fig. 37a.

Ti-Nb microalloyed steel

Supplementary water-quenching experiments on the Ti-Nb-alloyed steel at testing temperatures 800°C, 850°C and at 950°C were performed as well. Here, the specimens were quenched directly after the start of necking which was simply observed by the reduction of the measured force on the controllers' front panel, Fig. 37b.

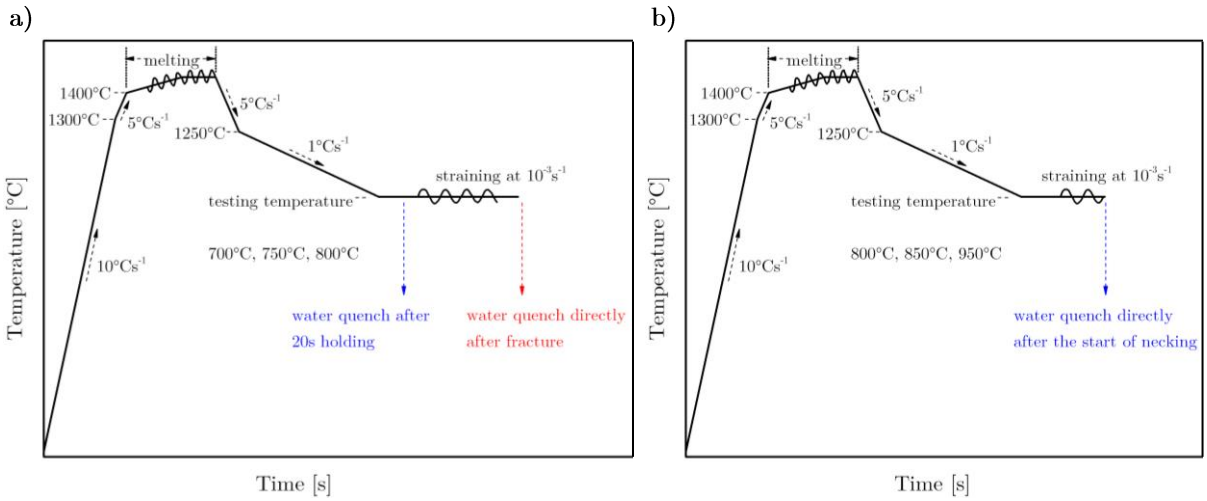

Fig. 37: Selected quenching experiments during the direct on-cooling process for a) low- and b) Ti-Nb alloyed steel.

4.3.2 Solution treatment tests – Ti-Nb microalloyed steel

In addition to the direct on-cooling experiments, solution treatment without in-situ melting on the Ti-Nb alloyed steel was also examined for comparison. Specimens were heated at 10°Cs^{-1} to 1320°C, held at this temperature for 600s and were further cooled down to the testing temperatures at 1°Cs^{-1}, Fig. 38.

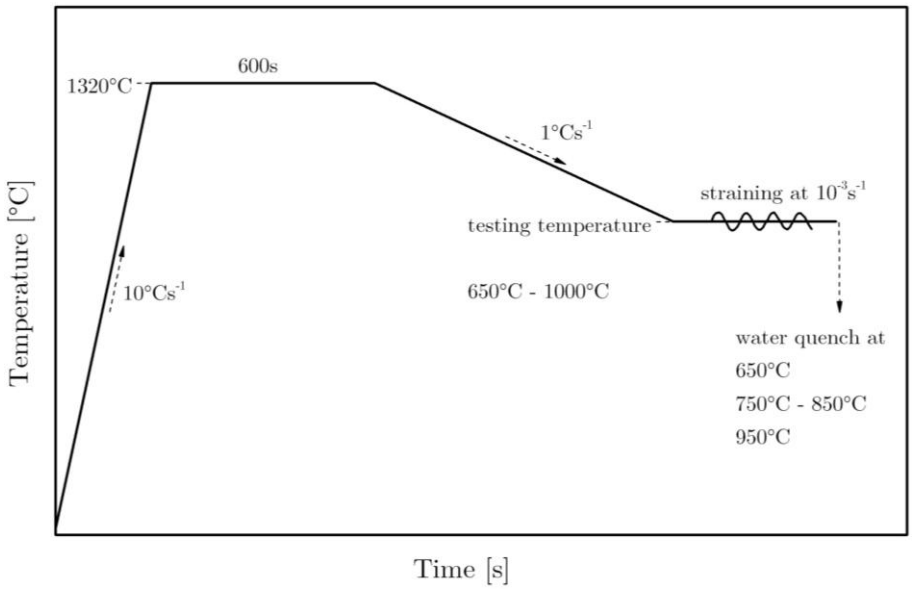

Fig. 38: Schematic illustration of solution-treatment cycle for Ti-Nb microalloyed steel.

4.3.3 Slow cooling tests – Ti-Nb microalloyed steel

The effect of a slow cooling process within a defined temperature range was examined by decelerating the cooling to 0.1°Cs^{-1} below 1100°C to the respective testing temperatures as shown in Fig. 39.

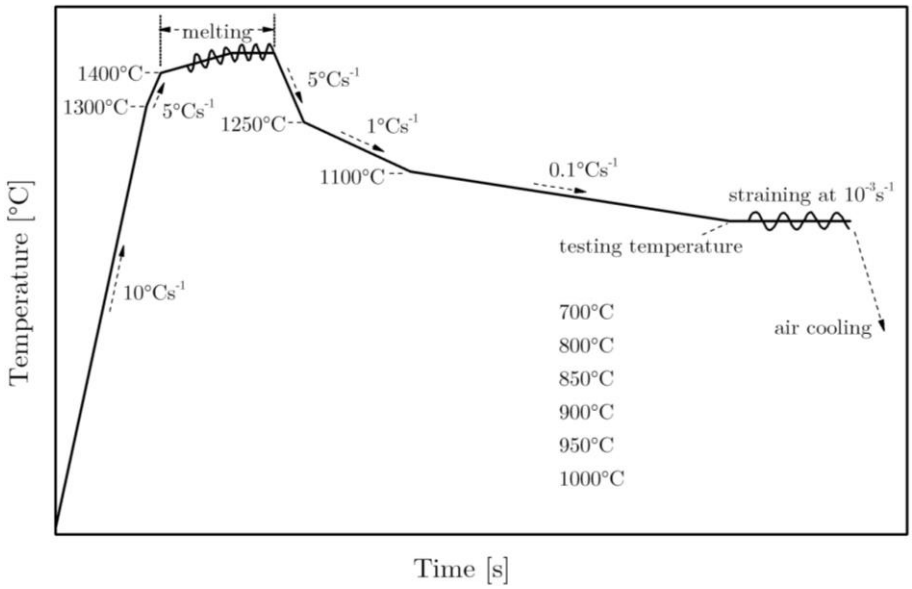

Fig. 39: Schematic illustration of the slow-cooling cycle for Ti-Nb microalloyed steel.

Similar to the quenching experiments during the direct on-cooling process (Fig. 37), complementary investigations were also performed by quenching the specimens directly after the onset of necking at testing temperatures of 850°C and 950°C, Fig. 40.

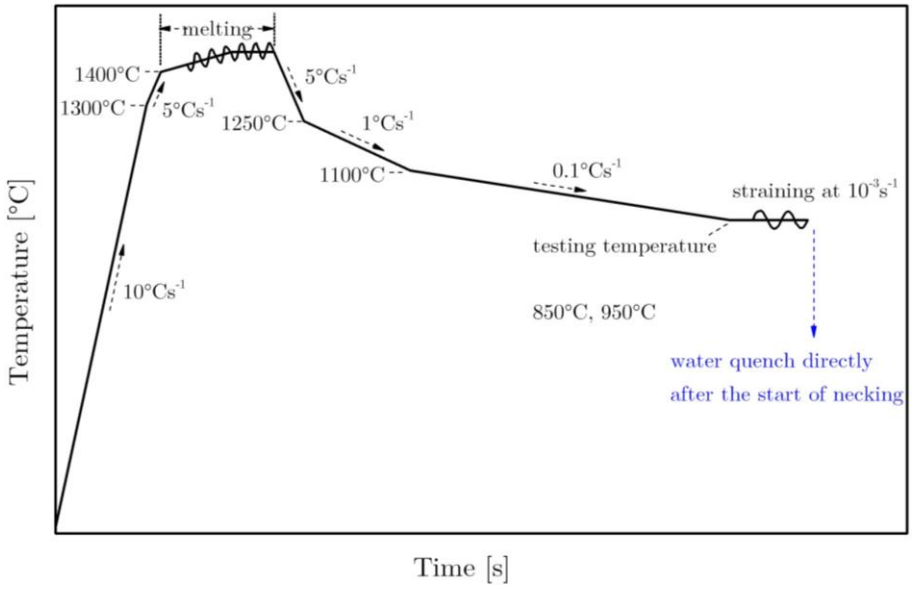

Fig. 40: Selected quenching experiments during slow cooling cycle for Ti-Nb alloyed steel.

4.3.4 Surface structure control cooling (SSCC) tests – Ti-Nb microalloyed steel

Additional hot ductility tests on the Ti-Nb-steel were carried out by utilizing the concept of the so-called "surface structure control cooling" (SSCC), Fig. 41. After the melting process, the specimens were first cooled to a temperature of 1320°C at 5°Cs^{-1} and further rapidly cooled at the maximum possible cooling rate by argon gas through the quenching nozzle to 550°C at which they were held for 120s. Then, the specimens were reheated to 950°C at a rate of 3.3°Cs^{-1} followed by a cooling or heating at 0.4°Cs^{-1} to the testing temperatures. Here, the samples were held for 120s after being subsequently strained to failure and finally water quenched.

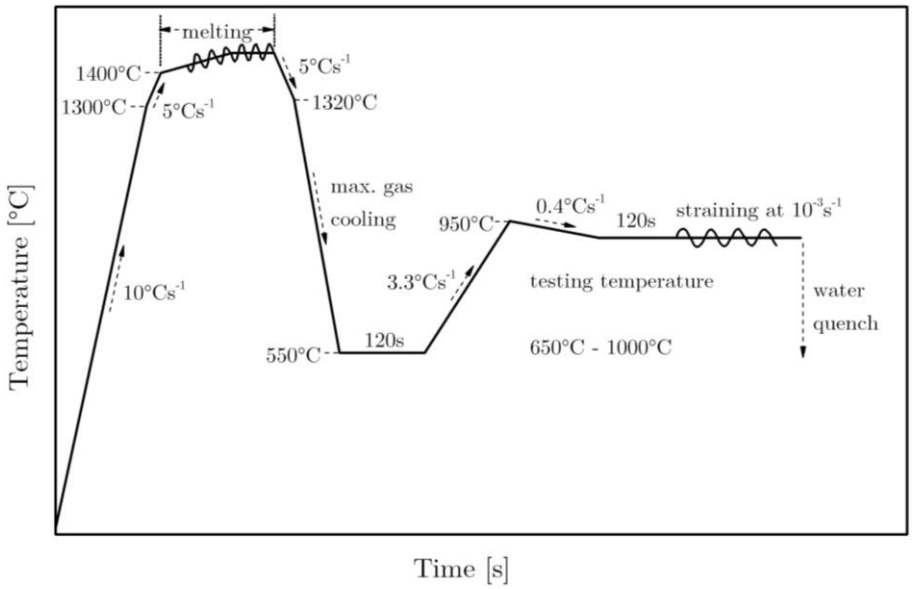

Fig. 41: Schematic illustration of the SSCC cycle for Ti-Nb microalloyed steel.

4.4 Materials characterization

The following part provides a brief description of the utilized materials characterization methods, such as light optical microscopy, scanning electron microscopy and transmission electron microscopy.

4.4.1 Light optical microscopy (LOM)

Optical microscopy using a ZEISS observer.Z1m equipped with an AxioCam MRc5 camera was applied to conduct microstructural investigations on the lower specimen parts near their

fracture surfaces as well as in relevant central regions of the partially strained and unstrained specimens. For this purpose, longitudinally sectioned specimens were hot mounted and further polished with a 500-, 800-, 1200-, 2000- and 4000-grit grinding SiC abrasive paper followed by a diamond polishing up to 1µm. In addition, a 3% Nital solution for about 10s was used to reveal the respective microstructure. The LOM-images were taken in such a way that the horizontal direction always corresponded to the loading direction or longitudinal specimen axis.

4.4.2 Scanning electron microscopy (SEM)

Metallographic fracture analyses were carried out on the upper parts of the pulled specimens using a Leo (ZEISS) 1450VP. SEM-images were taken perpendicular to the fracture surface using a constant acceleration voltage of 20kV.

4.4.3 Transmission electron microscopy (TEM)

TEM observations were performed applying a JEOL 200CX microscope operating at 200kV and a Philips CM300 operating at 300kV using carbon extraction replicas from the center of the partially strained and water-quenched specimens. Carbon replicas were made by evaporating carbon onto the polished and subsequently etched metallographic samples. Particle identification was conducted by electron diffraction and energy-dispersive X-ray (EDX) analysis. [101]

4.5 Simulations

The transformation behaviors of the investigated steels were examined by means of both the thermo-kinetic software MatCalc (version 5.52, rel. 1.010) with the thermodynamic (mc_fe_v2.019.tdb), physical (PhysData.pdb) and diffusion database (mc_fe_v2.005.ddb) [102]–[105] as well as the software-package JMatPro (version 8.0) [106], [107].

Equilibrium transformation temperatures of phases and primary precipitation during solidification considering the backdiffusion of fast diffusing elements such as C and N making use of the Scheil-Gulliver module [108] of MatCalc have been predicted by plotting the phase fractions and chemical compositions as a function of temperature. In addition, continuous cooling transformation (CCT) and time-temperature-transformation (TTT)–diagrams have been created using the JMatPro-program, since these diagrams cannot be experimentally

determined on cooling from the melt at the present state. Supplementary kinetic calculations by means of MatCalc have been performed for the Ti-Nb alloyed steel to simulate the precipitation evolution of secondary phase particles during the direct on-cooling and slow cooling treatments. In order to account for a precise influence of the primary precipitate phases on the second phase particles, the mean diameters of the primary precipitates were experimentally determined, since MatCalc considers the kinetic and diffusion processes only in the solid state. The data taken from the Scheil-calculations were further integrated in the kinetic models and were kept constant during the ensuing kinetic calculations. The precipitation domains for all simulations were set as austenite. Depending on the experimentally observed particles, the nucleation sites for the secondary particles have been appropriately selected. Further, the simulations have been properly adjusted according to the concept of the critical temperature T_{crit} [109], respectively. These setup parameters were used for all simulations in the present work while all other (default) parameters remained unchanged.

For better visualization, the results of the calculations have been reflected in the discussion chapter in order to serve a better correlation between hot ductility and precipitation states.

5 Results

The obtained results from the direct on-cooling experiments, in which both steel alloys were successively cooled to testing temperature after preceding melting, will be presented first. Then, the results of the additional hot tensile tests on the Ti-Nb microalloyed steel will be shown. In order to ensure a good overview of the results of the hot ductility investigations, the hot ductility curves have been classified into three appropriate regions, which are defined as follows:

- Low-temperature end (region 1): Testing temperatures 650–700°C
- Intermediate region (region 2): Testing temperatures 750–800°C
- High-temperature end (region 3): Testing temperatures 850–1000°C

For each region, selected typical and representative metallographic micrographs are illustrated. Following this, the results of the individual transformation behaviors of the investigated materials are presented.

5.1 Results of hot ductility and microstructural investigations

In the following section, hot ductility curves of reduction of area as a function of testing temperature and associated metallographic microstructures of steels are presented.

5.1.1 Direct on-cooling – Low- and Ti-Nb microalloyed steel

Hot ductility curves for both in-situ melted and solidified steels according to the testing schedule reported in chapter 4.3.1 are presented in Fig. 42. At the same time, the three particular regions have been depicted in the figure as mentioned in the beginning of this work. It can be seen, that the Ti-Nb-steel shows a relative low ductility over the whole tested temperature range, having a ductility minimum at 800°C with a RA value of about 30%. In the low-temperature end (region 1), the ductility curve remains almost flat with a maximum ductility being hardly greater than 40% at 650°C, whereas the ductility slightly increases to

values of approximately 60% RA in the high-temperature end at 1000°C. On the other hand, the low-alloyed steel exhibits a better ductility behavior compared to the Ti-Nb steel with a ductility minimum at 750°C of about 20% RA. From the ductility trough, the ductility curve of the low-alloyed steel shows steeper slopes both towards lower and higher testing temperatures. Here, the specimens have shown around 50% RA between 650°C and 700°C and very high RA values well above 70% between 900°C–1000°C within region 3.

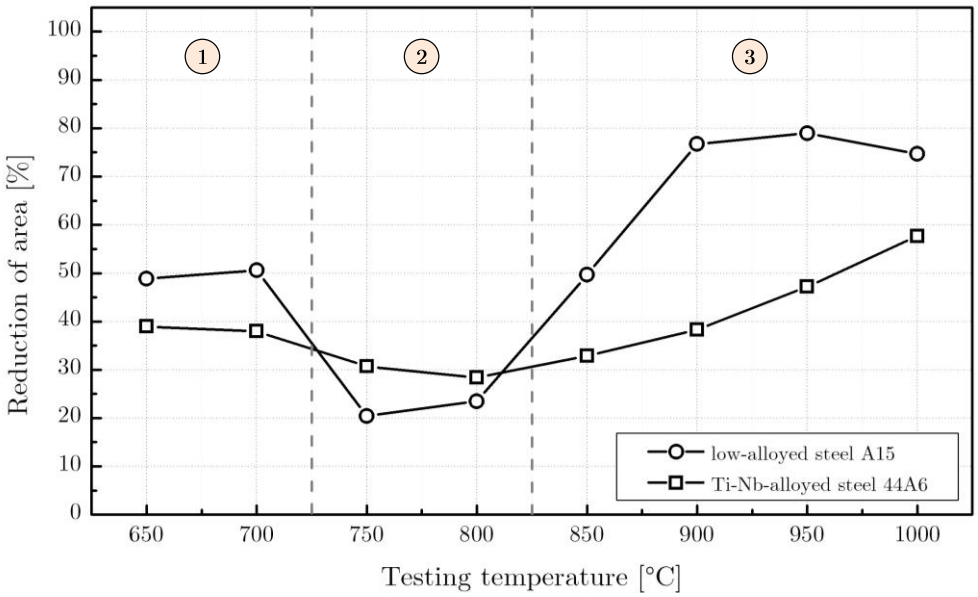

Fig. 42: Hot ductility curves of the investigated steels after being subjected to direct on-cooling process.

5.1.1.1 Microstructural investigations – Low-alloyed steel

Representative micrographs for each region and characteristic metallographic results obtained from the quenching experiments for the low-alloyed steel will be demonstrated in the following.

Region 1: Testing temperatures 650–700°C

Fig. 43a shows the fracture surface of the specimen tested at 650°C (RA=49%) obtained by SEM. As can be seen, the specimen exhibits parts of hot cracks with freely solidified dendritic surfaces or grain boundary surfaces over a large part of the fracture surface and a big shrinkage cavity formed in the edge-region. At a testing temperature of 700°C (RA=51%), a mixed separation consisting of intergranular and dimple fracture is evident, Fig. 43b.

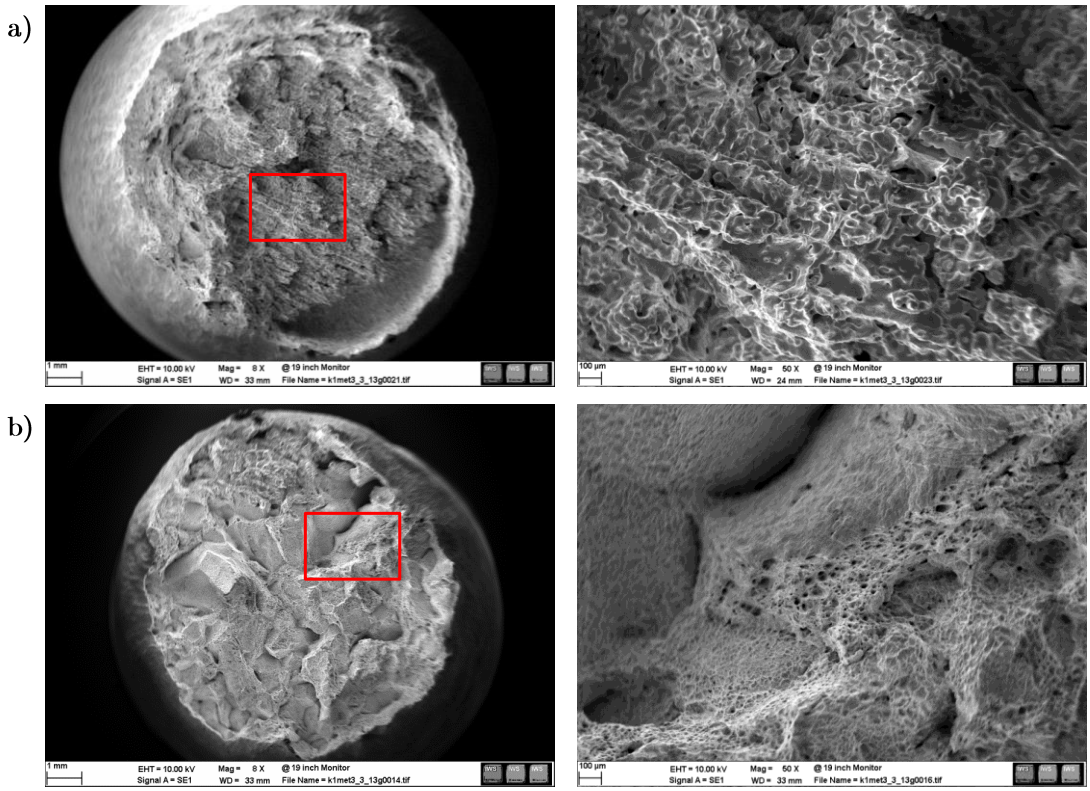

Fig. 43: Fracture surface (SEM) of specimen tested at a) 650°C (RA=49%) and b) 700°C (RA=51%).

Microstructural LOM-investigations on the unstrained and quenched specimens tested at the same temperature show bands of ferrite which surround the prior austenite grains, Fig. 44a. On the other hand, the specimen, which was immediately quenched after fracture, evinces increased ferrite-proportions as shown in Fig. 44b.

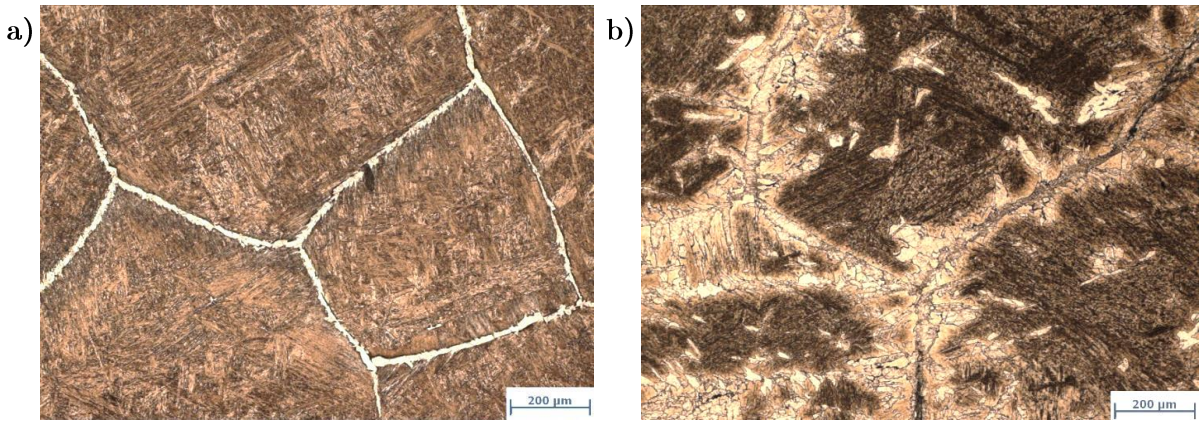

Fig. 44: LOM-images of quenched specimen tested at 700°C. a) after holding for 20s without deformation; b) after fracture (total exposure time ~ 280s).

Region 2: Testing temperatures 750–800°C

At testing temperatures between 750°C and 800°C, the SEM-images reveal a pronounced dimpled intergranular fracture as exemplary illustrated in Fig. 45 for a sample deformed at 750°C showing the lowest RA value of 20%.

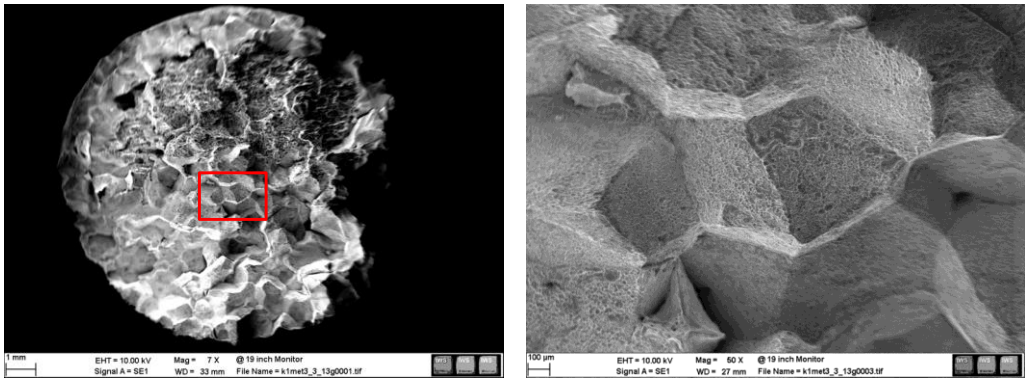

Fig. 45: SEM-fractographs of specimen tested at 750°C (RA=20%).

Specimens quenched at 750°C prior (Fig. 46a) and after deformation (Fig. 46b) show thin intergranular ferrite bands, which was rather not the case at 800°C, Fig. 46c and Fig. 46d. The measured mean grain size by ImageJ was found to be 1140µm at 750°C.

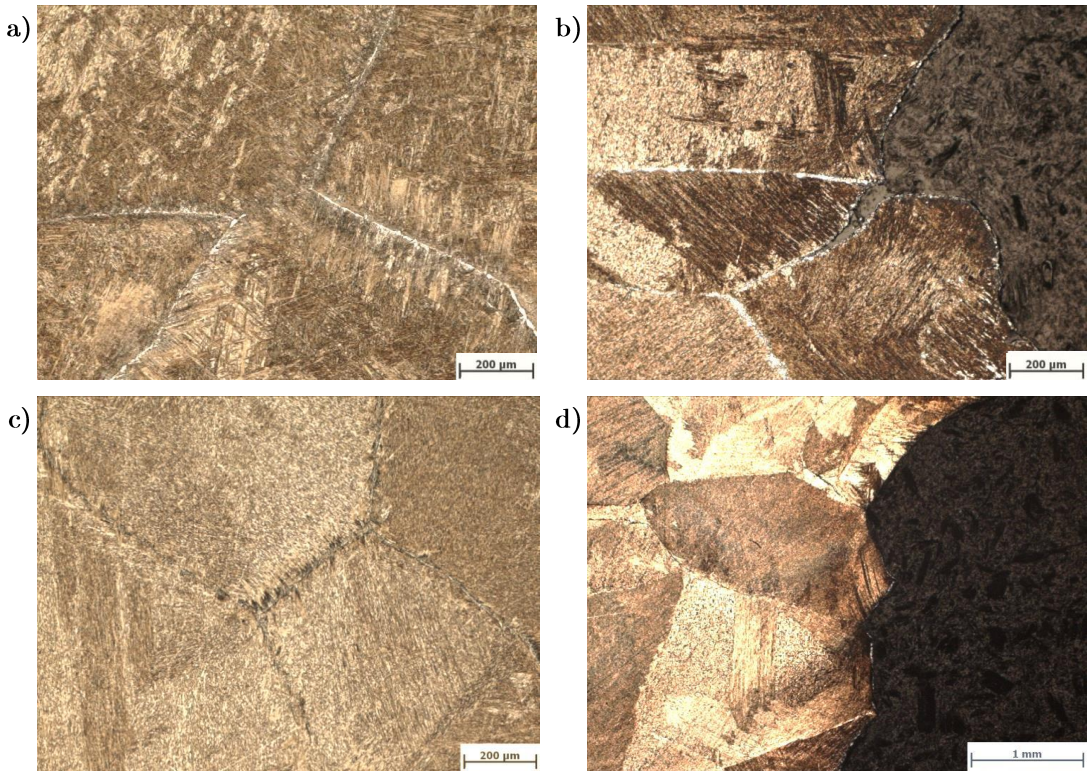

Fig. 46: LOM-images of quenched specimens. After 20s holding: a) at 750°C and c) at 800°C. After deformation: b) at 750°C (exp. time: 180s); d) at 800°C (exp. time: 290s).

Region 3: Testing temperatures 850–1000°C

With increased testing temperatures above 800°C, the fracture mode changes considerably from brittle to ductile showing transgranular fracture behavior with increased RA values up to 80%. Fig. 47 shows a representative micrograph of a specimen obtained within this regime with dendritic fracture areas in the specimen-center and plastic deformation towards peripheral regions.

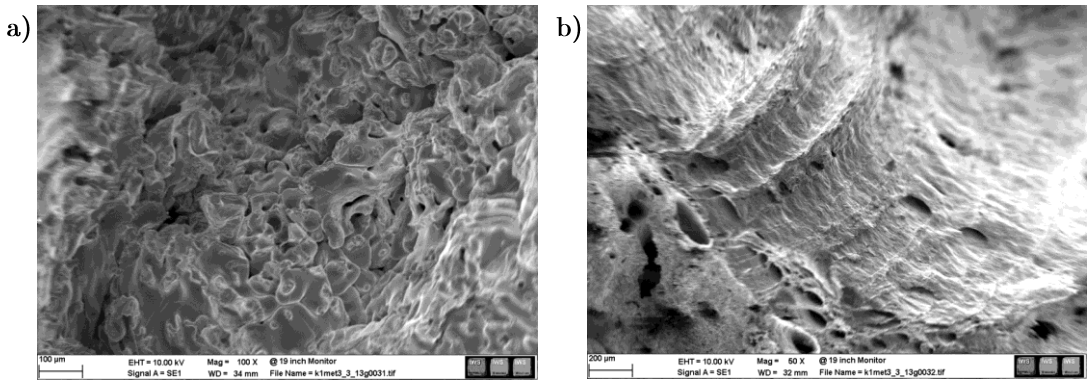

Fig. 47: Fracture surface (SEM) of specimen tested at 950°C (RA=79%). a) specimen-center; b) edge-region.

5.1.1.2 Microstructural investigations – Ti-Nb microalloyed steel

Region 1: Testing temperatures 650–700°C

The fracture surface of the tested Ti-Nb-alloyed steel specimens within the low-temperature end are characterized by fine and dimpled intergranular structures as illustrated in Fig. 48a at 650°C and Fig. 48b at 700°C.

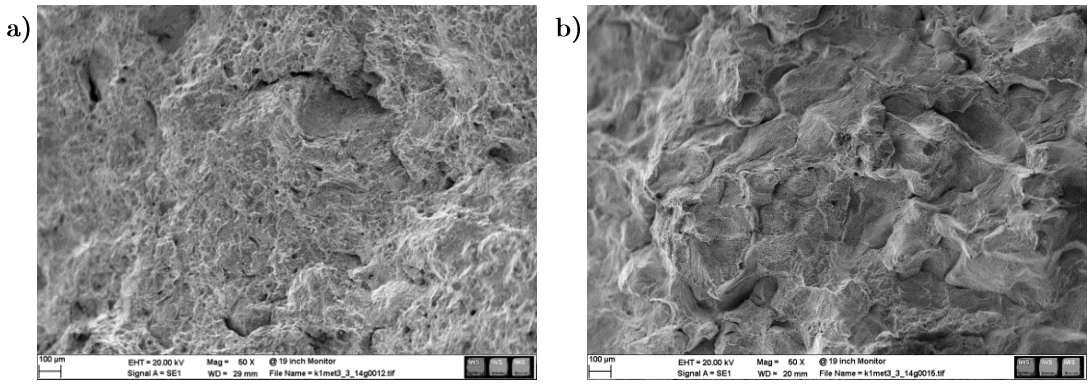

Fig. 48: SEM-fractographs of specimen tested at a) 650°C (RA=39%) and b) 700°C (RA=38%).

Region 2: Testing temperatures 750–800°C

Distinct brittle fracture was observed at deformation temperatures between 750°C and 800°C as shown in Fig. 49a on the SEM-image for a specimen tested at 750°C. Additionally, Fig. 49b presents the microstructure taken from the center of a specimen which was tested at 800°C and directly quenched after the start of necking showing. This image reveals clear indications of intergranular fracture propagating along thin ferrite bands at austenite grains.

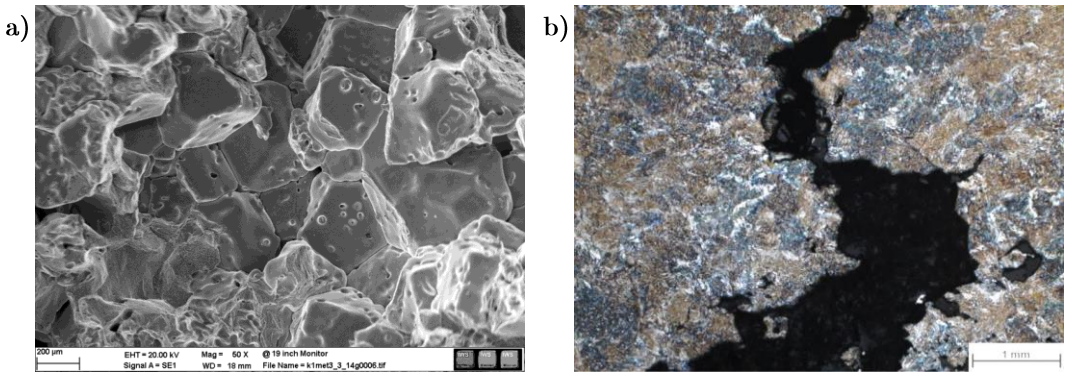

Fig. 49: a) Fracture surface of specimen tested at 750°C (RA=31%). b) LOM-image taken from the specimen center at the onset of necking at 800°C (total exposure time=120s).

Region 3: Testing temperatures 850–1000°C

Within region 3, typical intergranular fracture by grain boundary cracking with flat facets (Fig. 50a) and marked separation by wedge-type cracking still persists at testing temperatures up to 950°C as shown in Fig. 50b of sample quenched after 240s. Specimens being pulled at a temperature of 1000°C, however, are characterized by a slight recovery in ductility showing a mixed mode of ductile-brittle fracture, Fig. 51. However, the graphically measured mean grain size in this steel was found to be 385µm at 900°C.

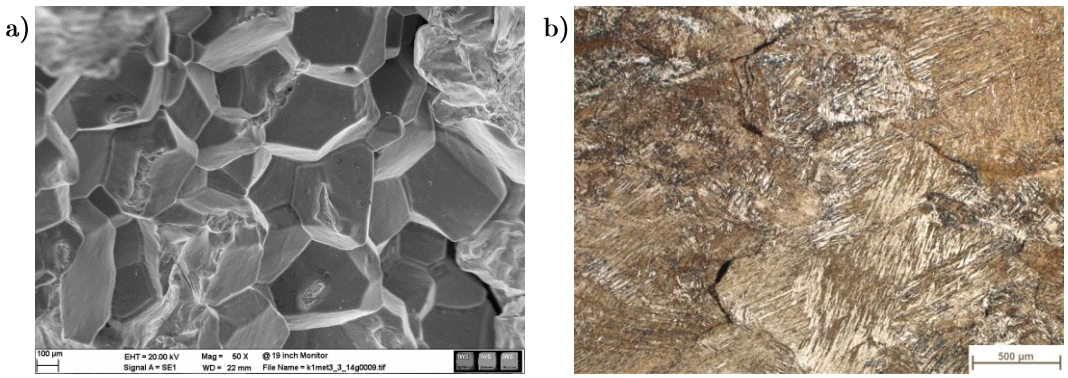

Fig. 50: SEM-fractograph of specimen tested at 850°C (RA=33%). b) LOM-image taken from the specimen center at the onset of necking at 950°C (total exposure time=240s).

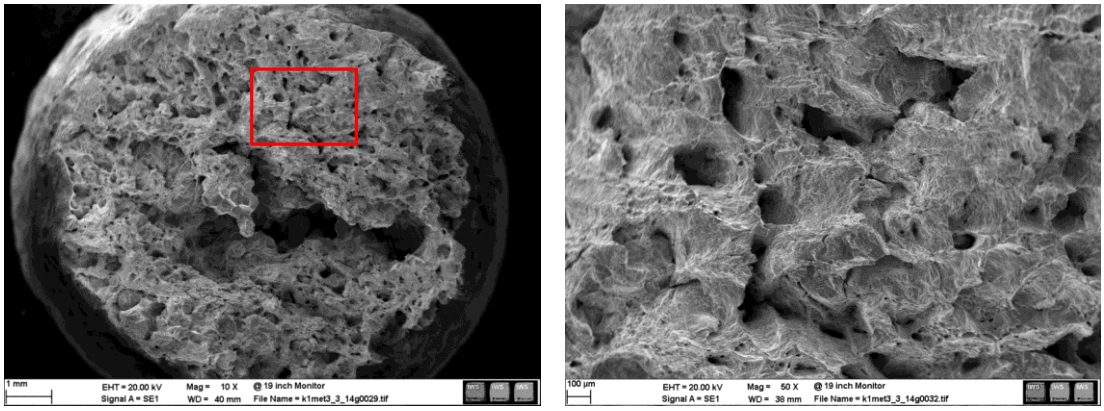

Fig. 51: Fracture surface of specimen tested at 1000°C (RA=58%).

5.1.2 Solution treatment – Ti-Nb microalloyed steel

The ductility curve of the solution treated samples is plotted in Fig. 52 with a quite similar shape compared to the results obtained throughout the direct on-cooling process. The minimum ductility temperature was found to be at 800°C with 30% RA followed by a hardly recovering course of the ductility in region 3, despite the fact that the samples have not been melted prior to cooling. On the other hand, the ductility continuously increases towards the lower testing region reaching the highest RA of more than 50% at 650°C.

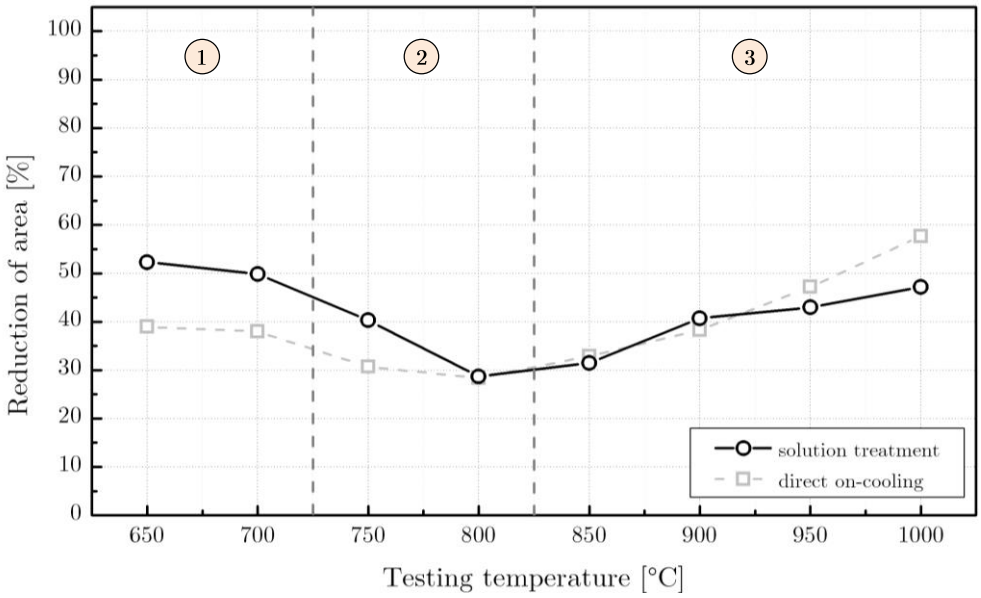

Fig. 52: Hot ductility curve of solution treated Ti-Nb steel samples.

5.1.2.1 Microstructural investigations

Region 1: Testing temperatures 650–700°C

Fig. 53a and b show light optical micrographs of a specimen tested at 650°C revealing a ductile fracture with partly isolated grain boundary cracks just behind the fracture surface. This ductile fracture behavior is better reflected by the additional SEM-micrographs shown in Fig. 53c for the same testing temperature and Fig. 53d for a testing temperature of 700°C.

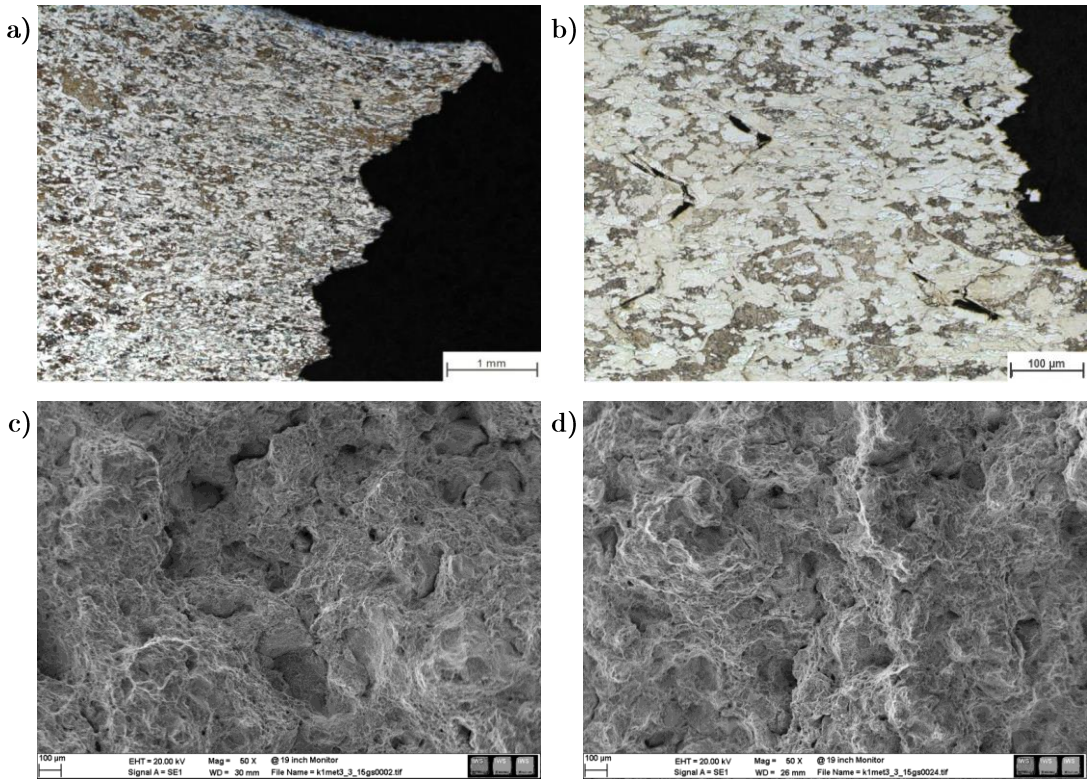

Fig. 53: a) and b) LOM-images of specimen tested at 650°C (RA=52%). SEM-fractographs of specimen tested at c) 650°C (RA=52%) and d) 700°C (RA=50%).

Region 2: Testing temperatures 750–800°C

Within the region of lowest ductility, the appearing fracture is characterized by marked intergranular cracking oriented at an angle of ±45° to the loading direction and crack propagation within thin ferrite bands along the austenite grain boundaries as shown in Fig. 54a at 800°C and Fig. 54b at 750°C.

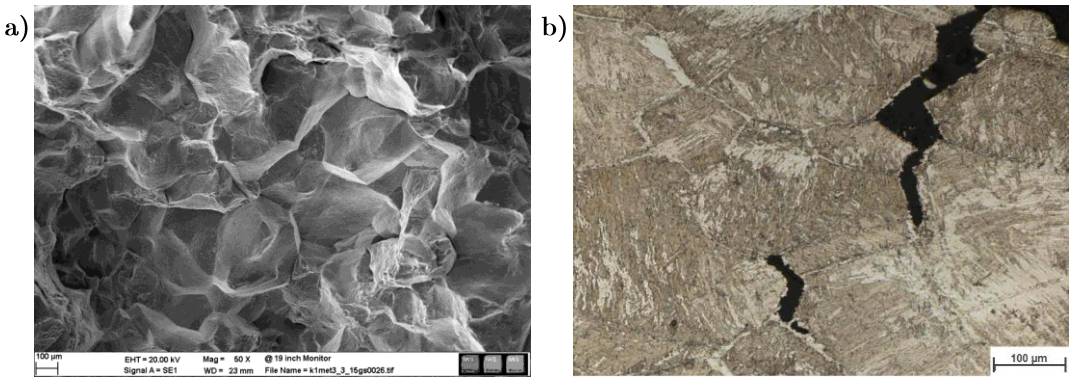

Fig. 54: a) Fracture surface of specimen tested at 800°C (RA=29%). b) LOM-image of a specimen quenched after fracture at 750°C (RA=40%).

Region 3: Testing temperatures 850–1000°C

Within the high-temperature end of the testing regime, the investigated material still reveals a poor ductility behavior with pronounced wedge-type cracking. The brittle decohesion is displayed in Fig. 55a–c for testing temperatures at 850–900°C, whereas an incipient mode of brittle-ductile fracture becomes only evident at 1000°C, Fig. 55d. The mean austenite grain size is determined as 195µm at 900°C.

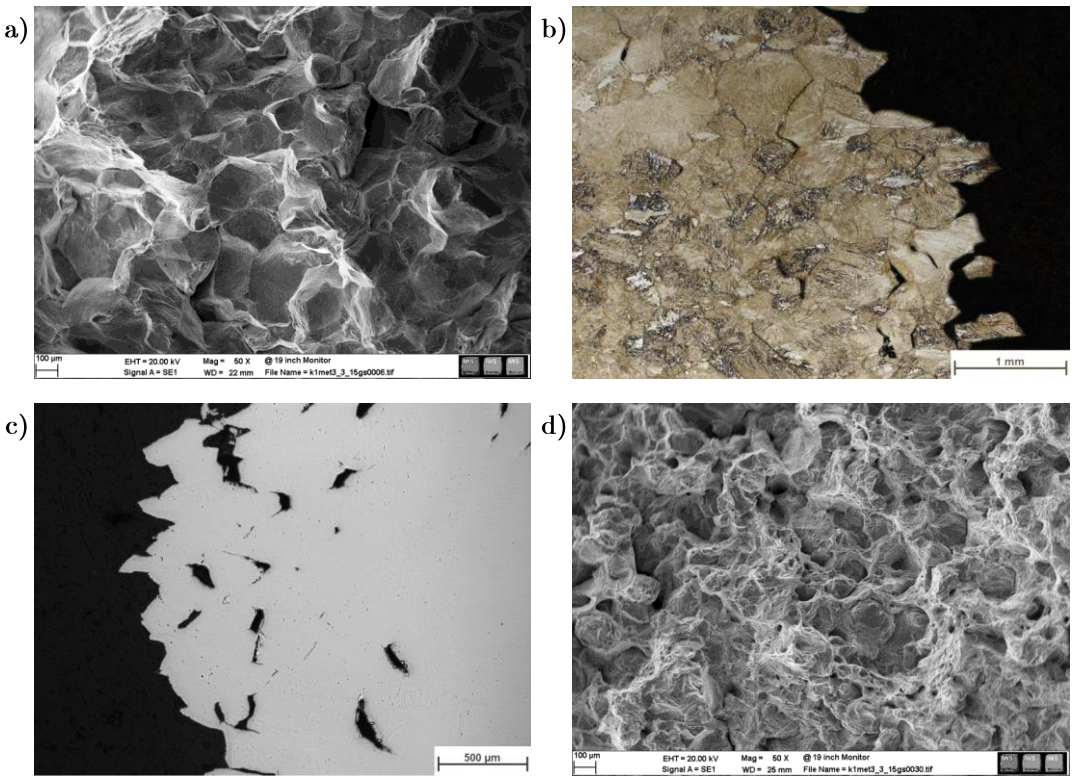

Fig. 55: a) SEM-fractograph and b) LOM-image of specimen tested at 850°C (RA=31%). c) Longitudinal section of polished specimen tested at 900°C (RA=41%). d) Fracture surface (SEM) of sample tested at 1000°C (RA=47%).

5.1.3 Slow cooling – Ti-Nb microalloyed steel

The influence of the slow cooling process on the hot ductility of the Ti-Nb steel specimens is shown in Fig. 56. Again, the ductility reaches a minimum at 800°C within region 2 with a reduction of area of almost 40%. Towards higher testing temperatures, the ductility steadily increases up to around 60%, while achieving a RA of 45% at 700°C in region 1.

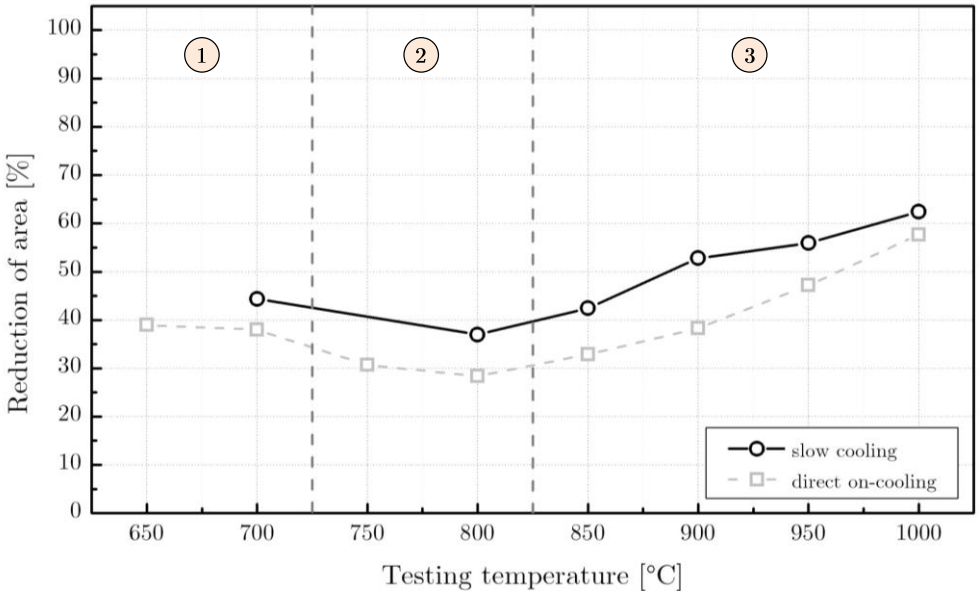

Fig. 56: Hot ductility curve of specimens after being subjected to the slow cooling process.

5.1.3.1 Microstructural investigations

Region 1: Testing temperatures 650–700°C

The fracture appearance of a specimen tested at 700°C within the low-temperature end is mainly characterized by a mixed ductile-brittle fracture as can be seen in Fig. 57. A close-up of the fracture surface is further showing partial laid-open melting cracks.

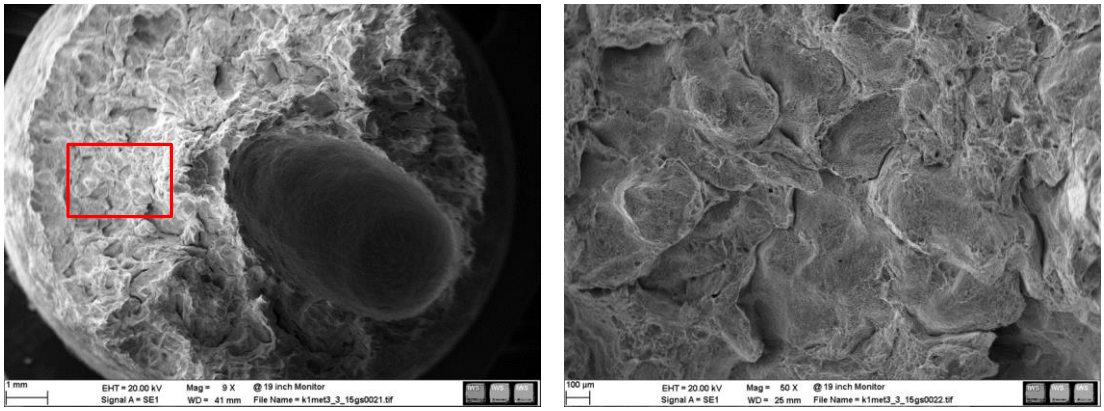

Fig. 57: Fracture surface of specimen tested at 700°C (RA=44%).

Region 2: Testing temperatures 750–800°C

The enhanced embrittlement in the intermediate hot ductility testing range is characterized by intergranular fracture with loose grain bonds as exemplary illustrated in Fig. 58 for a testing temperature of 800°C, which evinced the lowest measured RA at 800°C.

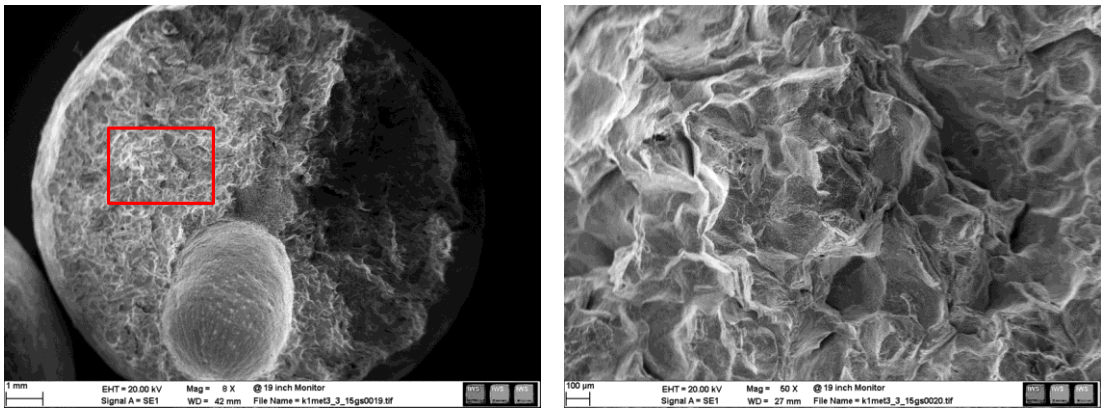

Fig. 58: Fracture surface of specimen tested at 800°C (RA=37%)

Region 3: Testing temperatures 850–1000°C

Fig. 59a and Fig. 59b demonstrate LOM-images of specimens which were strained at 850°C and at 950°C until the onset of necking and which were directly water-quenched to room temperature. The microstructures reveal pronounced crack propagation along austenite grain boundaries (Fig. 59a) and incipient austenite grain boundary loosening (Fig. 59b), respectively. The higher the testing temperature, the more ductile the material has become, characterized by few ductile dimples on the fracture surface, Fig. 59c at 900°C and Fig. 59d at 1000°C.

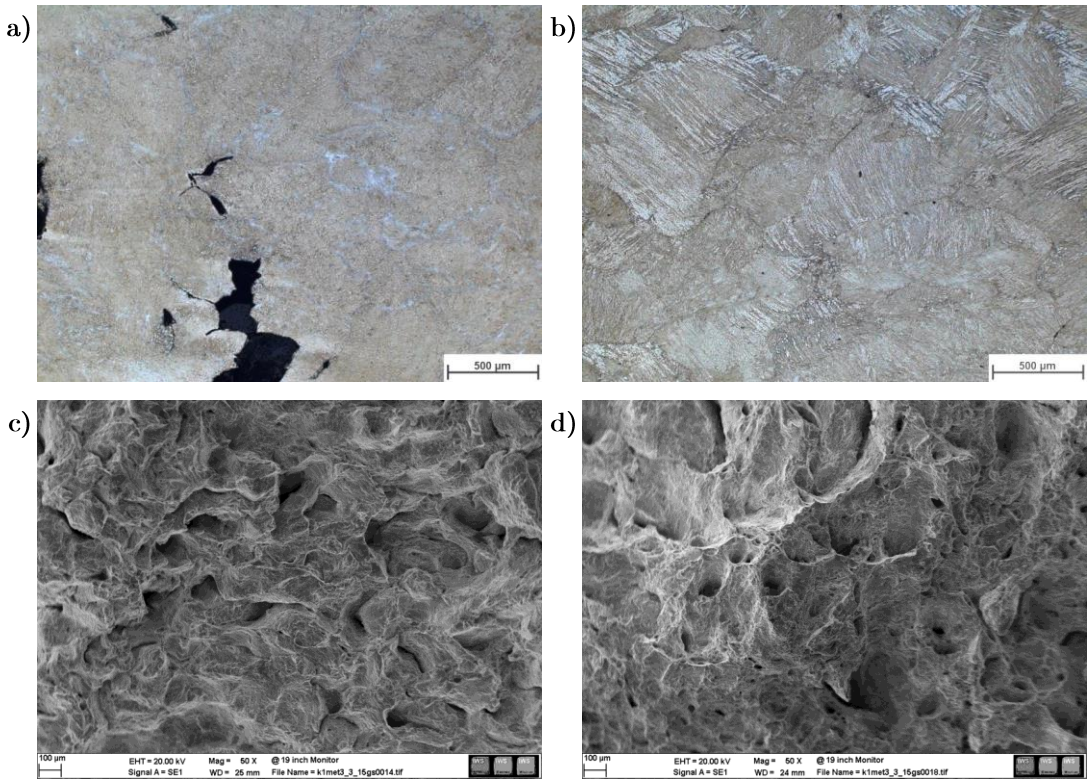

Fig. 59: LOM-images of partially strained specimen at a) 850°C (total exposure time=150s) and b) 950°C (total exposure time=160s). Fracture surface (SEM) of specimen tested at c) 900°C (RA=53%) and d) 1000°C (RA=62%).

5.1.4 Surface structure control cooling – Ti-Nb microalloyed steel

The ductility curve of specimens exposed to the SSCC process is plotted in Fig. 60. It is more obvious that the present results do not display the typical shape of a ductility curve with a pronounced ductility minimum as already observed during previous experiments. Rather, a distinct ductility loss above 750°C can be noticed. In the lower temperature region between 650-700°C, the specimens possess very good ductility behavior around 70%. At 750°C, however, the ductility severely drops to 20% and remains very poor with increasing testing temperatures persisting up to the end of region 3.

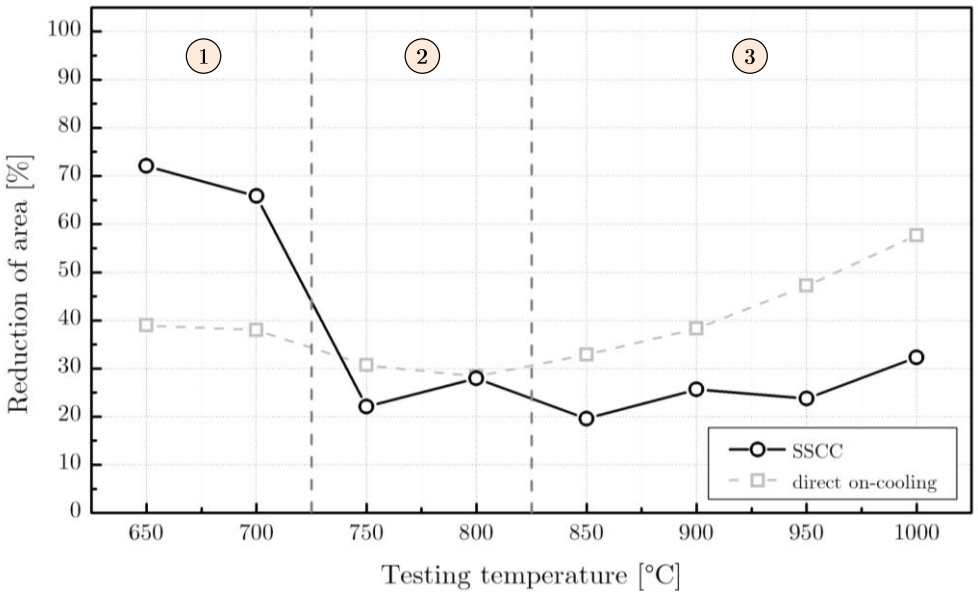

Fig. 60: Hot ductility curve of samples after being subjected to the SSCC process.

5.1.4.1 Microstructural investigations

Region 1: Testing temperatures 650–700°C

Fig. 61 shows different microstructural observations from specimens tested in the low temperature end, in which the highest RA-values were obtained (RA=66-72%). As illustrated in Fig. 61, the fracture surface of specimen tested at 700°C reveal ductile fracture proportions, while Fig. 61b shows a ductile fracture appearance with a microstructure which consists of almost entirely single ferrite-phase.

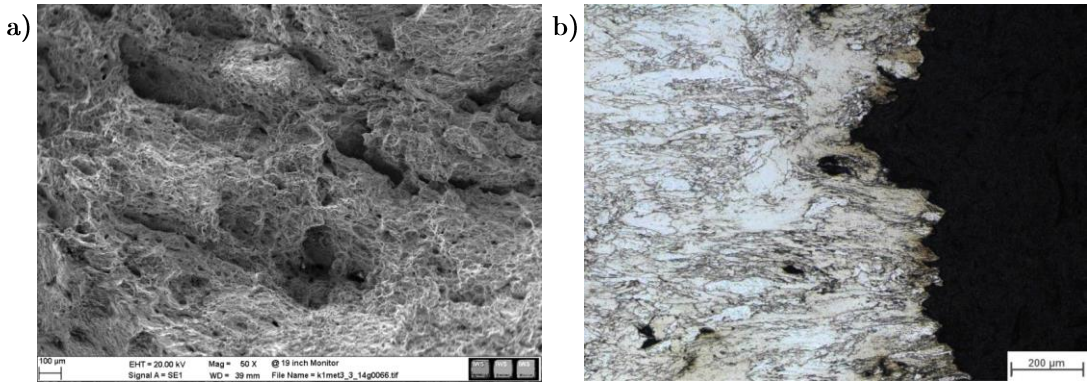

Fig. 61: Fracture surface of specimen tested at a) 700°C (RA=66%). b) LOM-image of specimen tested at 650°C (RA=72%).

Region 2: Testing temperatures 750–800°C

In Fig. 62a–d, the light optical micrographs and appropriate SEM-images of specimens tested between 750-800°C are presented showing marked intergranular fracture. The light optical micrographs in Fig. 62b and Fig. 62d reflect a fine-grained microstructure with partly isolated cracks behind the brittle fracture surface.

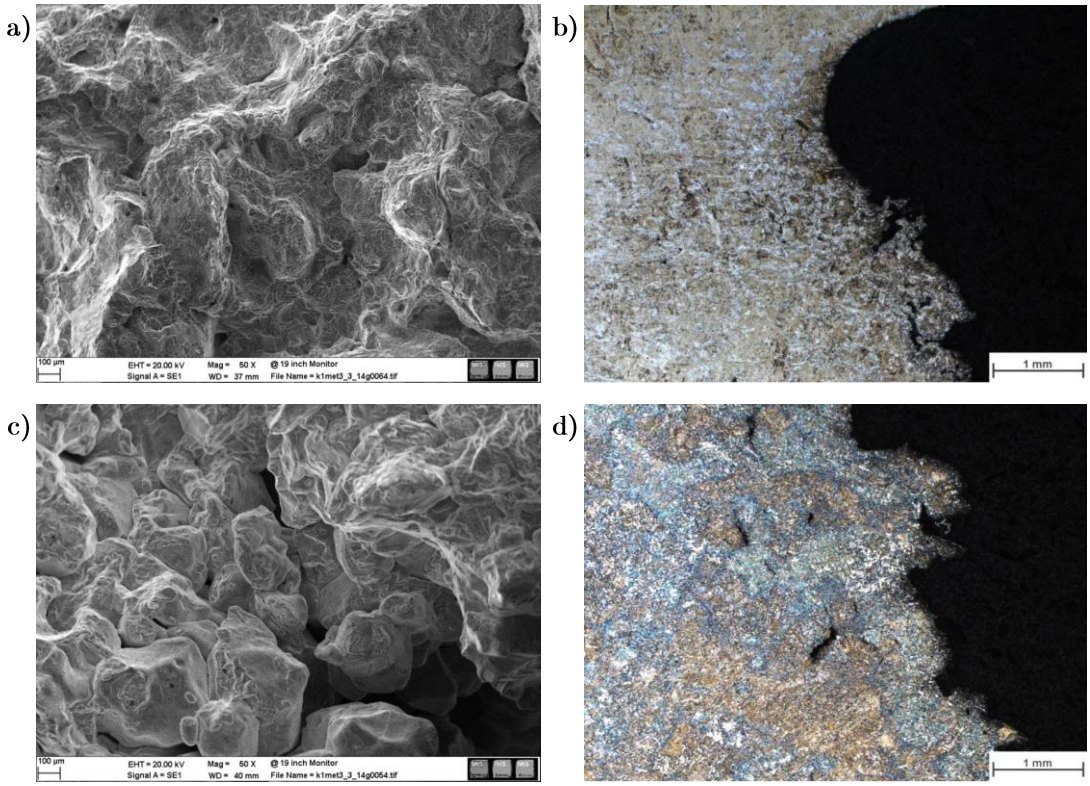

Fig. 62: SEM-fractographs (a and c) and LOM-images (b and d) of specimen tested at 750°C (RA=22%) and at 800°C (RA=28%), respectively.

Region 3: Testing temperatures 850–1000°C

With increasing testing temperature, the SSCC-process caused the ductility to deteriorate within the high-temperature end as well, resulting in materials decohesion characterized by distinct grain separation with low RA-values. Fig. 63 presents representative fracture surfaces of specimens which failed in a brittle manner at deformation temperatures between 900°C and 1000°C. The brittle fracture appearance does not significantly differ from the microstructures observed within the intermediate testing region.

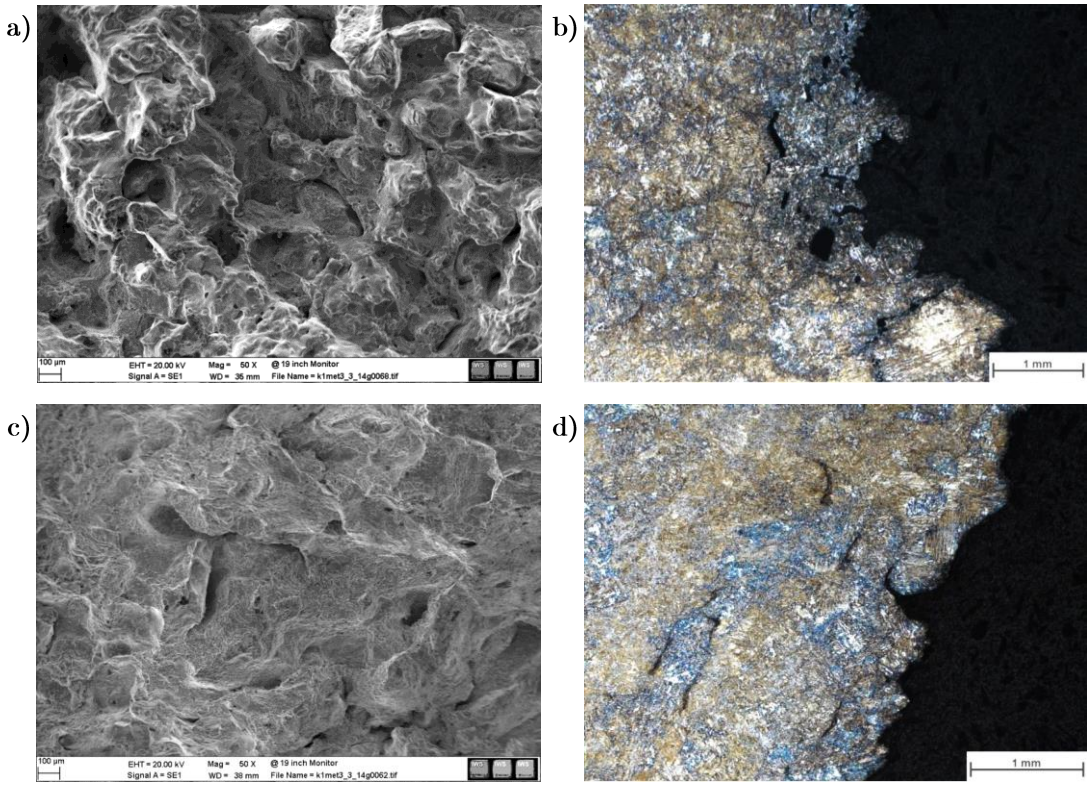

Fig. 63: a) Fracture surface of specimen tested at 900°C (RA=26%). b) LOM-image of specimen tested at 1000°C (RA=32%). c) Fracture surface and d) LOM-image of specimen tested at 950°C (RA=24%).

5.2 Results of transformation behaviors

This section gives an overview of the simulation results regarding the transformation behaviors which have been determined by means of MatCalc and JMatPro.

5.2.1 Low-alloyed steel

The results of the equilibrium calculations and Scheil-simulations by MatCalc will be presented first. Then, the results of the JMatPro-calculations including CCT and TTT-diagrams will be demonstrated for the low-alloyed steel.

5.2.1.1 Equilibrium calculations

In a first step, thermodynamic equilibrium calculations using MatCalc have been performed to predict the type and amount of equilibrium and precipitates phases which are expected to appear over a certain temperature range. Fig. 64 shows an equilibrium diagram

between 600°C and 1600°C for all elements up to a phase fraction of 0.001%, whereas phosphorus has been excluded from the calculations for simplification purposes. It can be seen, that all arising precipitate phases (cementite, AlN, MnS and MX) only exist in the solid state. The major constituents of the secondary MX phase were Ti, Nb, C and N which stay stable up to a maximum temperature of 1068°C. The equilibrium transformation temperatures A_{e3} and A_{e1} were determined to be 820°C and 693°C, respectively. The results of the observed transformation temperatures and the solution temperatures of the different equilibrium phases have been summarized in Table 2.

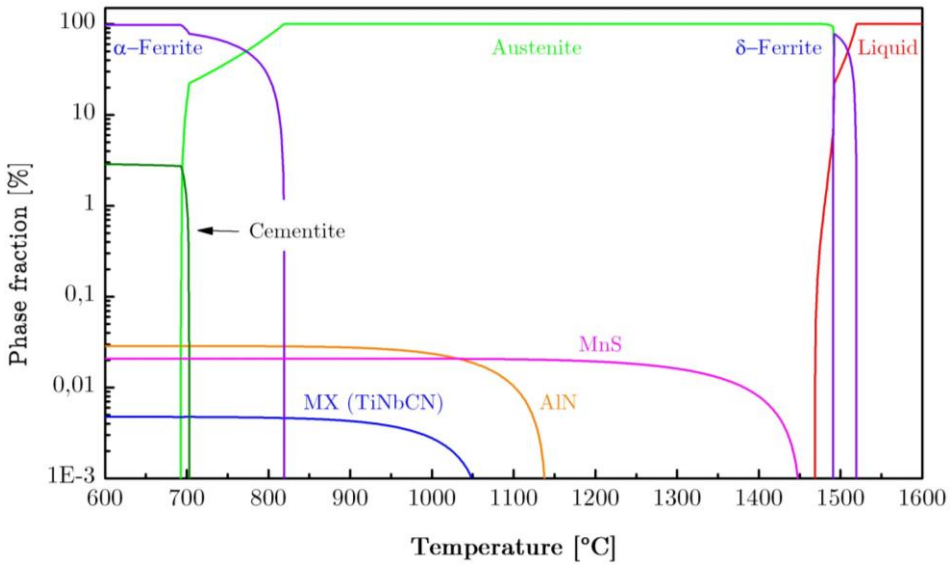

Fig. 64: Equilibrium phase diagram for the low-alloyed steel.

Table 2: Equilibrium phase transformation and precipitate dissolution temperatures for low-alloyed steel.

Matrix phases	$\alpha \leftrightarrow \alpha + \gamma$ (A_{e1})	693°C
	$\alpha + \gamma \leftrightarrow \gamma$ (A_{e3})	820°C
	$\gamma \leftrightarrow L + \gamma$ (T_S)	1469°C
	$L + \gamma \leftrightarrow L + \gamma + \delta$	1491°C
	$L + \gamma + \delta \leftrightarrow L + \delta$	1492°C
	$L + \delta \leftrightarrow L$ (T_L)	1519°C
Precipitate phases	Cementite_sol	704°C
	MnS_sol	1453°C
	AlN_sol	1141°C
	MX_sol	1068°C

5.2.1.2 Scheil-Gulliver-calculations

Scheil-Gulliver simulations have been performed to predict the fraction and composition of primary precipitation during solidification. Fig. 65 shows the residual liquid fraction down to 3% at a final temperature of 1364°C if the classical Scheil-model has been applied. By considering the back-diffusion of the interstitial elements C and N, the solidification temperature increases from 1364°C up to 1460°C, giving a more realistic impression of the solidification behavior of the respective steel alloy. For the sake of completeness, the solidification temperature by the full thermodynamic equilibrium (1486°C at 3% liquid fraction) has been added to the diagram as well.

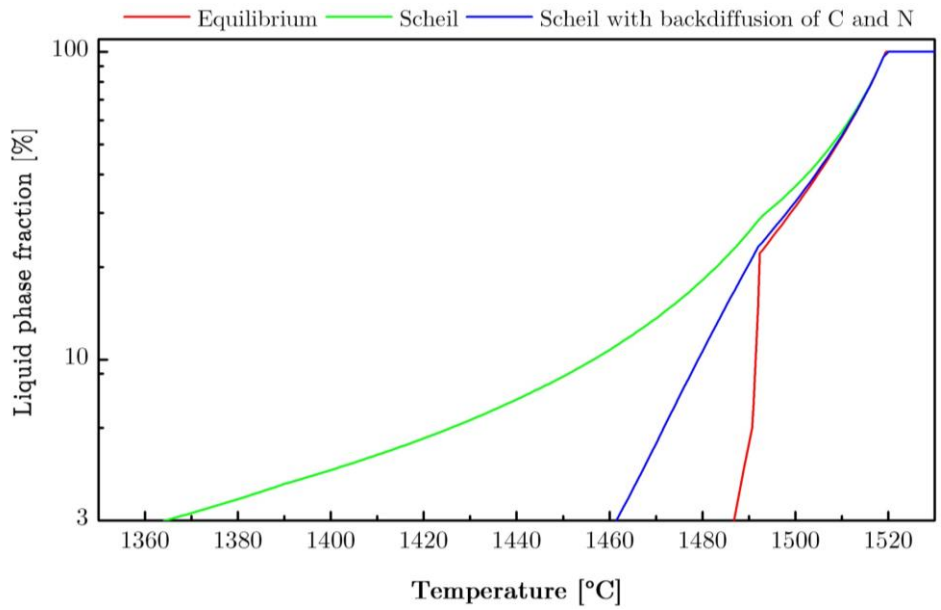

Fig. 65: Solidus-temperatures for equilibrium and solidification intervals according to Scheil with and without back-diffusion of C and N.

Fig. 66 shows the calculated primary solid phases with backdiffusion of C and N up to a liquid phase fraction of 1% (1449°C). In contrast to the equilibrium calculations, it can be seen that the MnS-phase should be present as a primary phase in the solidified material. This phase starts to precipitate within the liquid at 1452°C and reaches 0.01% phase fraction at 1% liquid fraction. The composition of the arising MnS-phase with around 50%Mn and 50%S, however, is illustrated in Fig. 67.

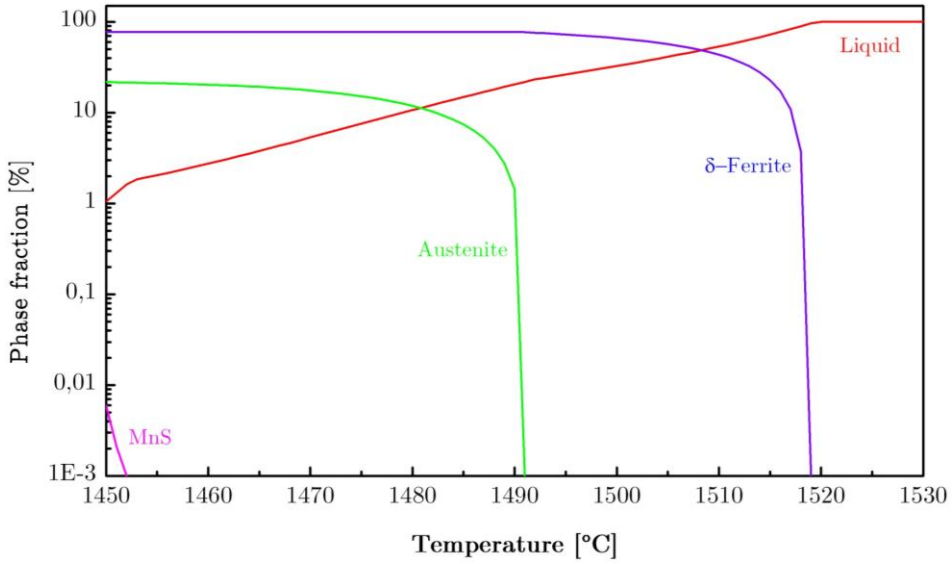

Fig. 66: Primary phases during solidification according to Scheil for the low-alloyed steel.

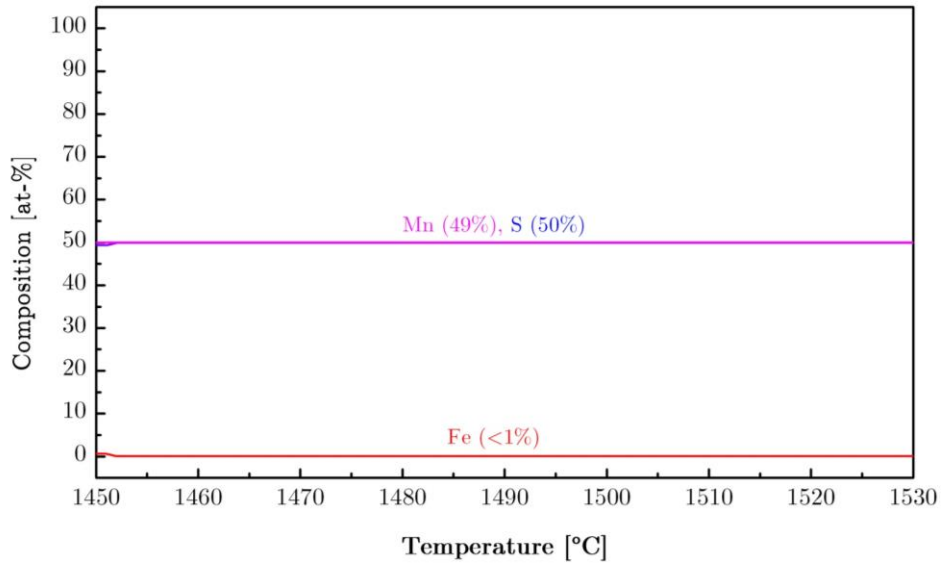

Fig. 67: Composition of the primary precipitate phase MnS according to Scheil for the low-alloyed steel.

5.2.1.3 JMatPro-simulations

The calculated continuous cooling transformation (CCT)–diagram for different cooling rates is plotted in Fig. 68. The given grain size of 1140µm is equivalent to the measured mean grain size during the direct on-cooling treatment as shown in section 5.1.1. As can be seen, the ferrite-start-temperature on cooling for a cooling rate of 1°Cs^{-1} for instance, is located at approximately 730°C. The A_{e3}-temperature, on the other hand, was found to be at 825°C, coinciding well with the value obtained by MatCalc (820°C). Additionally, Fig. 69 illustrates a time-temperature-transformation (TTT)–diagram, showing which phases are to

be expected once the steel has been quickly cooled from a defined austenitizing state to a certain temperature at which it is isothermally kept for specific time periods.

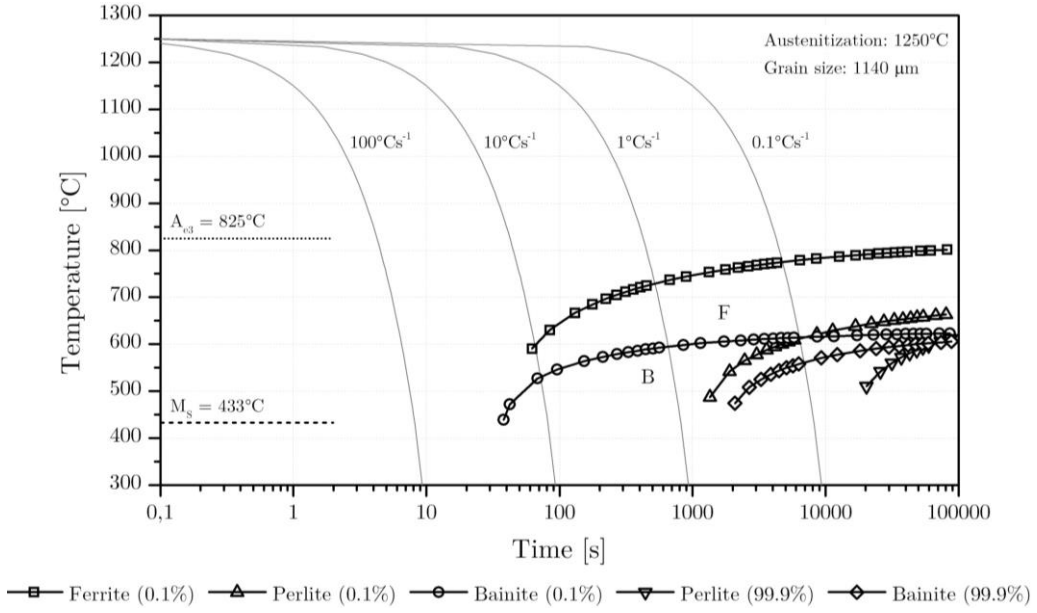

Fig. 68: CCT-diagram for the low-alloyed steel /JMatPro.

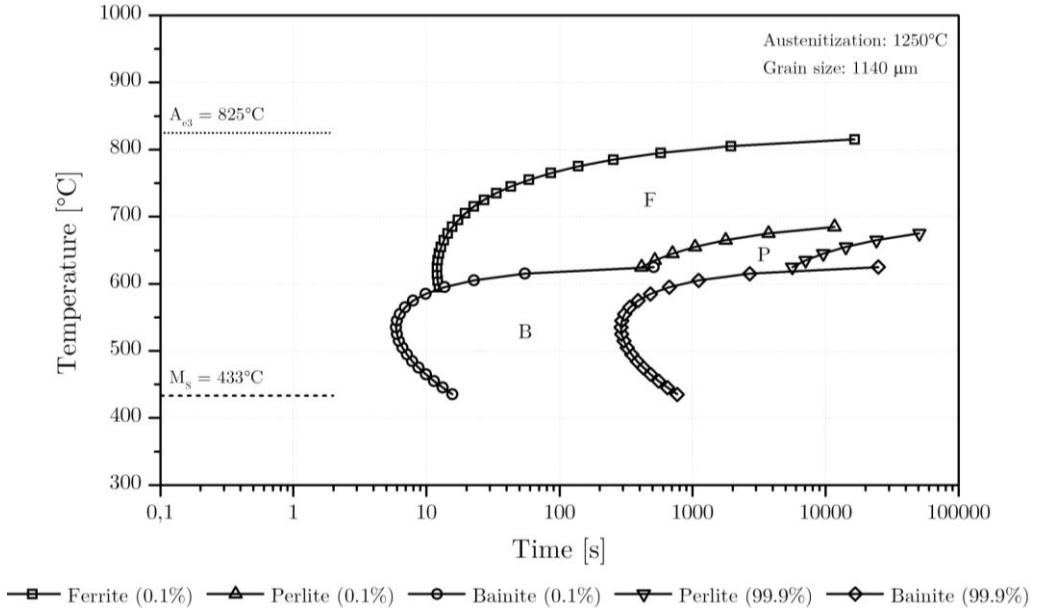

Fig. 69: TTT-diagram for the low-alloyed steel /JMatPro.

5.2.2 Ti-Nb microalloyed steel

This section contains the MatCalc-simulation results of the evaluated thermodynamic phases for both equilibrium and Scheil-Gulliver non-equilibrium solidification states for the Ti-Nb alloyed steel. Following this, the simulation results of phase transition temperatures obtained by the JMatPro software are finally presented.

5.2.2.1 Equilibrium calculations

The results of the thermodynamic equilibrium analysis for the Ti-Nb-microalloyed steel by plotting an equilibrium phase diagram between 600°C and 1600°C up to a phase fraction of 0.001% are displayed in Fig. 70. It can be seen, that the relative high amount of Ti together with the higher amount of Nb compared to the low-alloyed steel cause the formation of a Ti-Nb-rich primary MX-precipitate-phase up to a phase fraction of 0.33% with a solution temperature of 1519°C, almost coinciding with the materials liquidus temperature. In this case, the equilibrium transformation temperatures A_{e3} and A_{e1} were determined to be 829°C and 641°C, respectively.

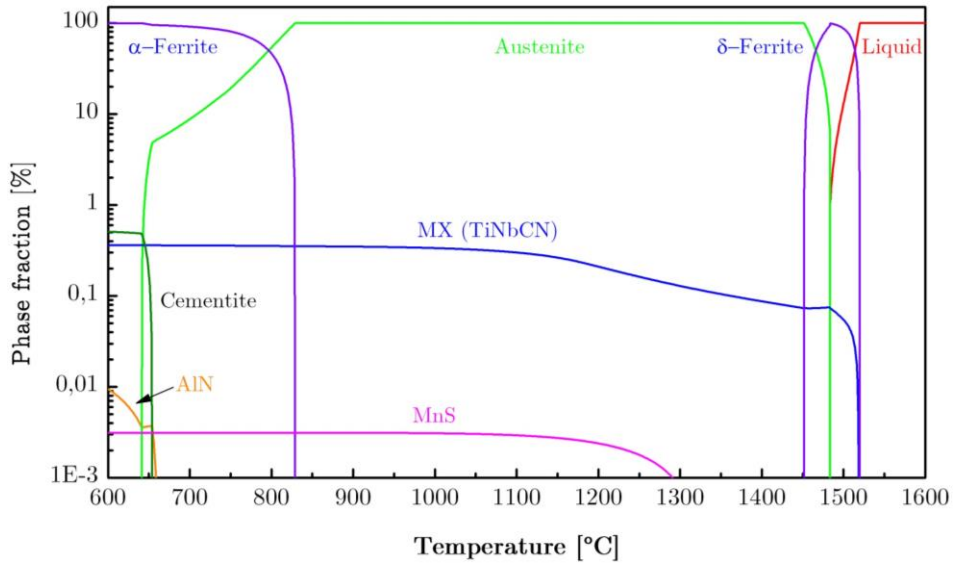

Fig. 70: Equilibrium phase diagram for the Ti-Nb microalloyed steel.

Table 3 summarizes the evaluated equilibrium phases and corresponding solution temperatures. The results of the low-alloyed steel have also been added to the table for comparison.

Table 3: Equilibrium phase transformation and precipitate dissolution temperatures for Ti-Nb microalloyed and low-alloyed steel.

		Ti-Nb microalloyed steel	**Low-alloyed steel**
Matrix phases	$\alpha \leftrightarrow \alpha + \gamma$ (A_{e1})	641°C	693°C
	$\alpha + \gamma \leftrightarrow \gamma$ (A_{e3})	829°C	820°C
	$\gamma \leftrightarrow \gamma + \delta$	1452°C	1469°C
	$\gamma + \delta \leftrightarrow L + \gamma + \delta$ (T_S)	1483°C	1491°C
	$L + \gamma + \delta \leftrightarrow L + \delta$	1484°C	1492°C
	$L + \delta \leftrightarrow L$ (T_L)	1520°C	1519°C
Precipitate phases	Cementite_sol	654°C	704°C
	MnS_sol	1327°C	1453°C
	AlN_sol	660°C	1141°C
	MX_sol	1519°C	1068°C

5.2.2.2 Scheil-Gulliver-calculations

The results of the Scheil-Gulliver analysis up to 3% liquid phase fraction are presented in Fig. 71, again by making use of both the standard Scheil-Gulliver-simulation and the analysis with back-diffusion of the fast diffusing elements C and N.

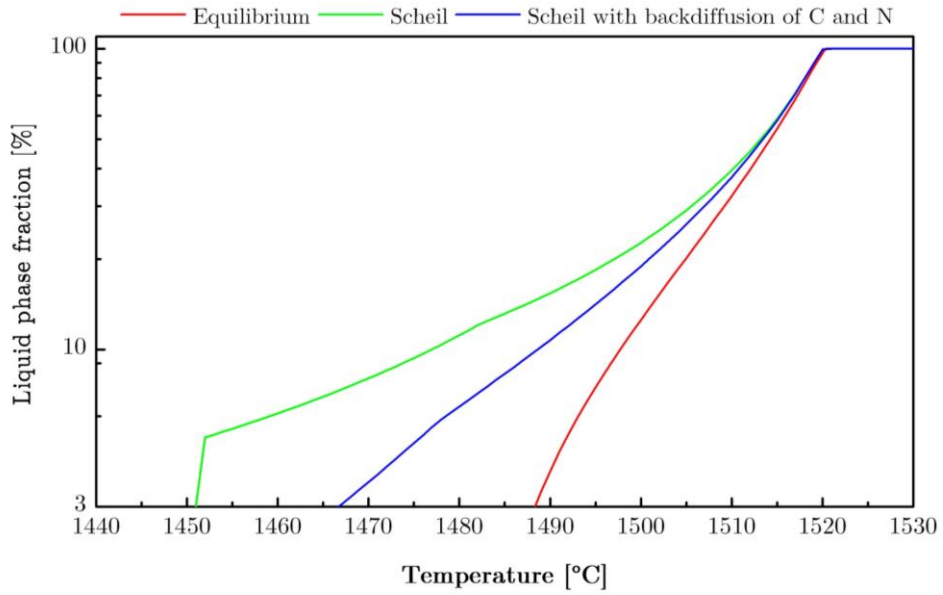

Fig. 71: Solidus-temperatures for equilibrium and solidification intervals according to Scheil with and without back-diffusion of C and N.

As can be seen, the backdiffusion leads to a slight increase of the solidification temperature of about 10°C to 1462°C. Furthermore, the liquid and solid phase fractions as a function of temperature at 1% liquid by taking into account the backdiffusion of C and N are displayed in Fig. 72. The composition of the primary precipitate phase versus temperature is

shown in Fig. 73. It can be seen, that primarily Ti, C and N are present within the liquid range during solidification.

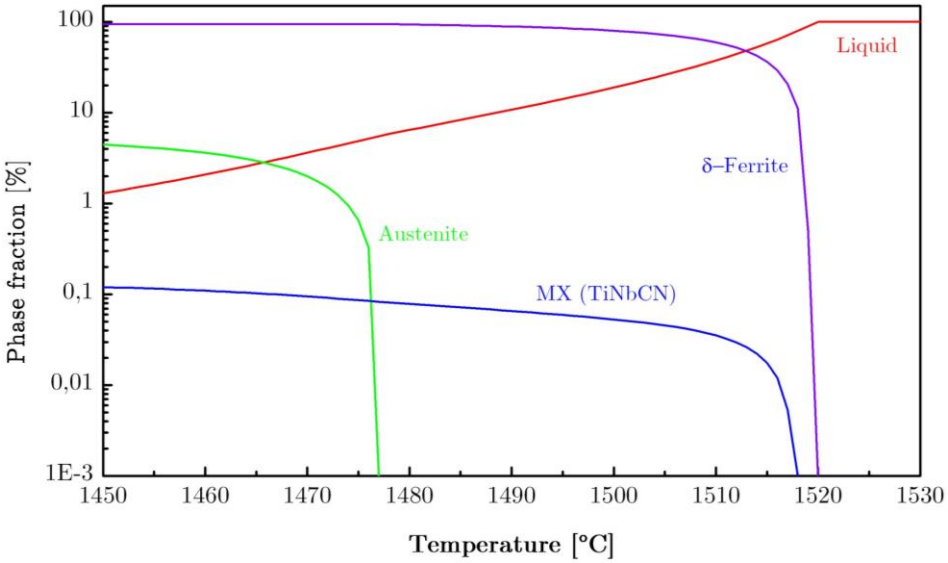

Fig. 72: Primary phases during solidification according to Scheil for the Ti-Nb microalloyed steel.

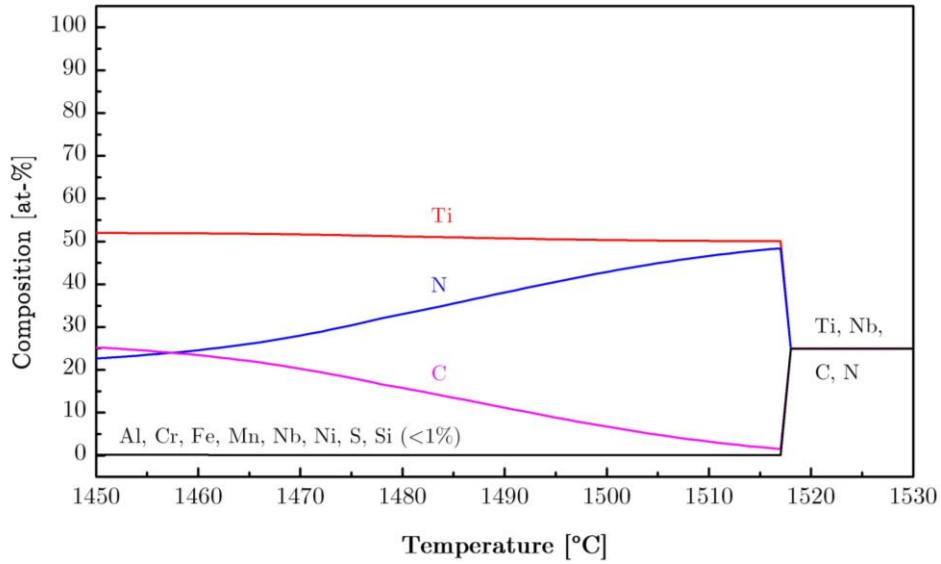

Fig. 73: Composition of the primary precipitate phase MX according to Scheil for the Ti-Nb microalloyed steel.

5.2.2.3 JMatPro-simulations

The CCT-diagram using the software JMatPro for the Ti-Nb microalloyed steel is shown in Fig. 74. Here, the austenite-to-ferrite transformation temperature for a continuous cooling of 1°Cs^{-1} is slightly lower at 720°C compared to the low-alloyed steel, taking into account the experimentally obtained finer mean grain size as shown in section 5.1.1. The equilibrium temperature A_{e3} was found to be at 837°C. Furthermore, the calculated TTT-diagram (Fig. 75) indicates that e.g. no ferrite is expected to be present below around e.g. 600°C.

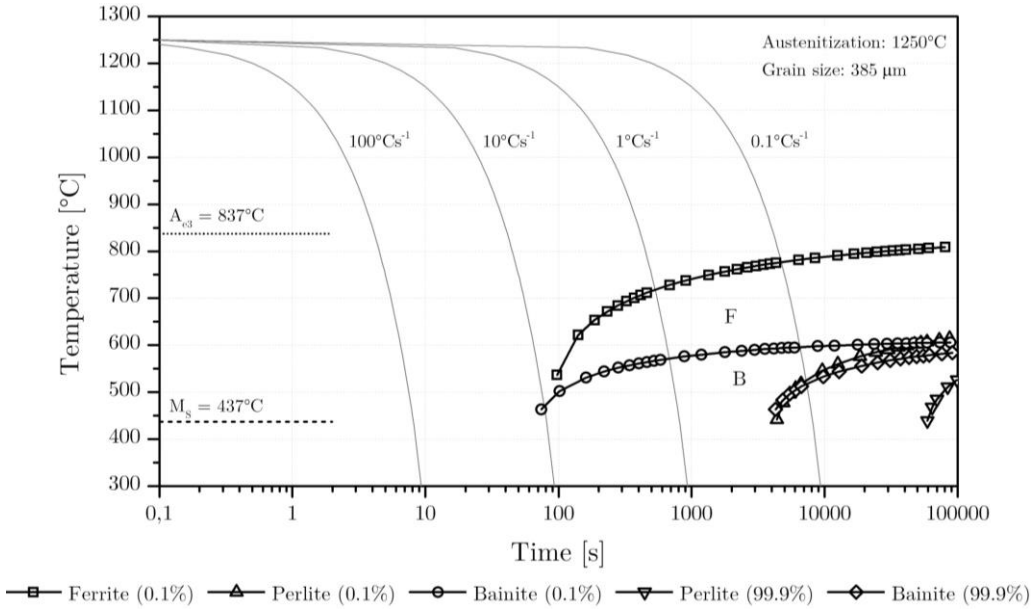

Fig. 74: CCT-diagram for the Ti-Nb microalloyed steel /JMatPro.

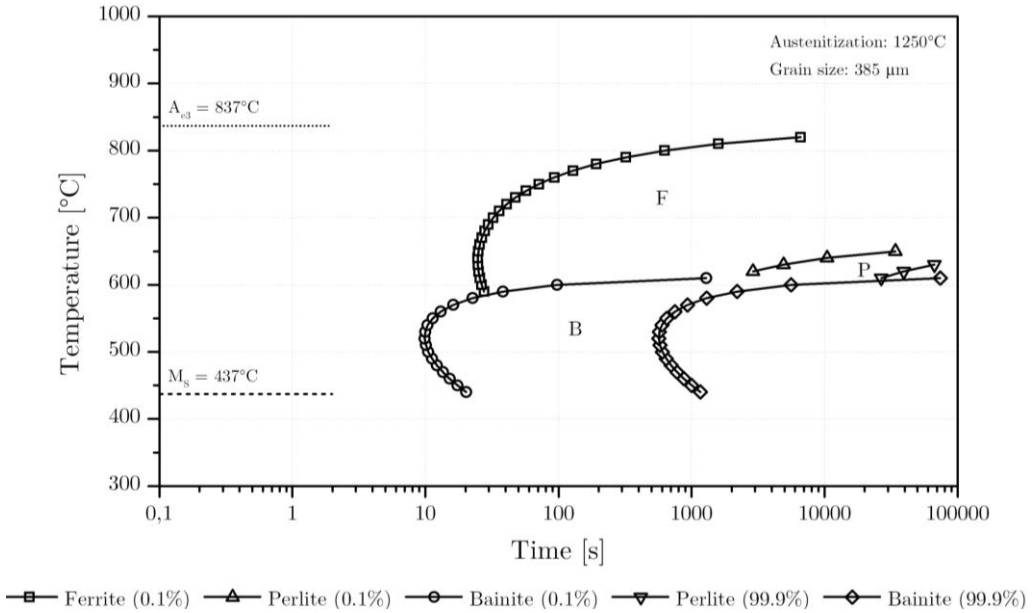

Fig. 75: TTT-diagram for the Ti-Nb microalloyed steel /JMatPro.

6 Discussion

This chapter analyzes the hot ductility behavior of the investigated steels between 650°C and 1000°C (regions 1–3) and discusses the diverse observed embrittlement phenomena during the thermomechanical treatments. The influence of the direct on-cooling process on the hot ductility of the low– and Ti-Nb alloyed steel is discussed in detail first. Then, the hot ductility behavior during solution treatment, slow cooling and SSCC process are discussed.

6.1 Direct on-cooling – Low- and Ti-Nb microalloyed steel

The analysis of the hot ductility behaviors of the low- and microalloyed steels are divided into three testing temperature regions 1–3, beginning from region 3 at testing temperatures from 850°C to 1000°C. Subsequently, the hot ductility within region 2 and region 1 are compared and discussed.

6.1.1 Region 3: Testing temperatures 850–1000°C

Starting from the high-temperature end as highlighted in Fig. 42, an addition of titanium and niobium clearly leads to a substantial loss in ductility over the whole region by applying the respective thermomechanical schedule after melting and solidification. At first glance, the microstructural observations on quenched specimens show noticeable differences between the austenite grain sizes of the two tested steels (1140µm for the low-alloyed and 385µm for the Ti-Nb steel). Despite the fact that the low-alloyed steel exhibits a coarser microstructure than the Ti-Nb steel, the larger grain size does not impair the ductility as would have been expected. Basically, a finer microstructure results in increased grain boundary surfaces and increased amount of triple-points, impeding crack propagation [73], [74]. Therefore, the worse hot ductility of Ti-Nb alloyed steel in the single austenite region is most likely related to the precipitation states such as precipitates size and volume fraction [52]. For this reason, additional quenching experiments at 850°C and 950°C were carried out to conduct microstructural analyses by TEM and EDX using carbon extraction replicas.

Fig. 76 shows a characteristic microstructure with homogeneously distributed small precipitates of a specimen which was strained at 950°C using a strain rate of ε=0.001s^{-1} until the onset of necking and subsequently water-quenched. These particles were primarily found inside the grains and infrequently on grain boundaries and were almost entirely identified as Ti-Nb-rich carbides of cuboidal shape with chemical compositions of around 50–65at.-% Ti and 20–30at.-% Nb.

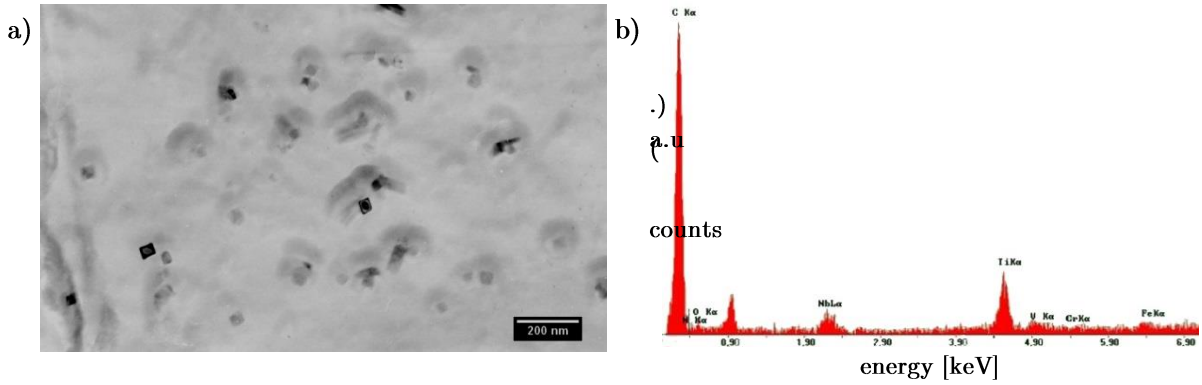

Fig. 76: a) TEM-image of specimen strained until necking and water-quenched at 950°C.
b) Typical EDX spectrum obtained from a particle.

Additionally, statistical analyses of the precipitates distribution have been performed by determining the particles mean diameter (D) as well as the particles number density (N_V)[3]:

$$D = \frac{\text{total length of particles}}{\text{number of particles}} \text{ [m]}, \qquad (1.\ 9)$$

$$N_V = \frac{\text{number of particles}}{\text{area} \times \text{thickness of replica sample}} \text{ [m}^{-3}\text{]}, \qquad (1.\ 10)$$

According to the analyses, around 72% of the analyzed particles were in the size interval between 20 to 40nm, with a mean particle diameter of 31nm.

Thermo-kinetic calculations by means of MatCalc have been performed to simulate the precipitation evolution of the TiNb-precipitates during the direct on-cooling process. It was assumed that the secondary particles nucleate on dislocations in austenite with a selected equilibrium dislocation density of $1 \cdot 10^{11}$m^{-2}. In order to account for the influence of the primary precipitates on the secondary ones, the mean diameter of the primary MX was experimentally determined to be 1800µm. The phase fractions and chemical compositions, on the other hand, were taken from the Scheil-calculations at 3% liquid fraction (Fig. 72). Even

[3] Should be treated with caution, since a certain level of inaccuracy may still exist.

though any secondary MnS-particles have not been found at the metallographic specimens, the nucleation and growth of these particles have been considered in the calculations as well, since they have been found to occur in the equilibrium diagram shown in Fig. 70.

The simulation results for 950°C are presented in the following, Fig. 77. As the phase fraction of the MnS is below 10^{-6} percent, the results of these particles are thus not shown in the figure.

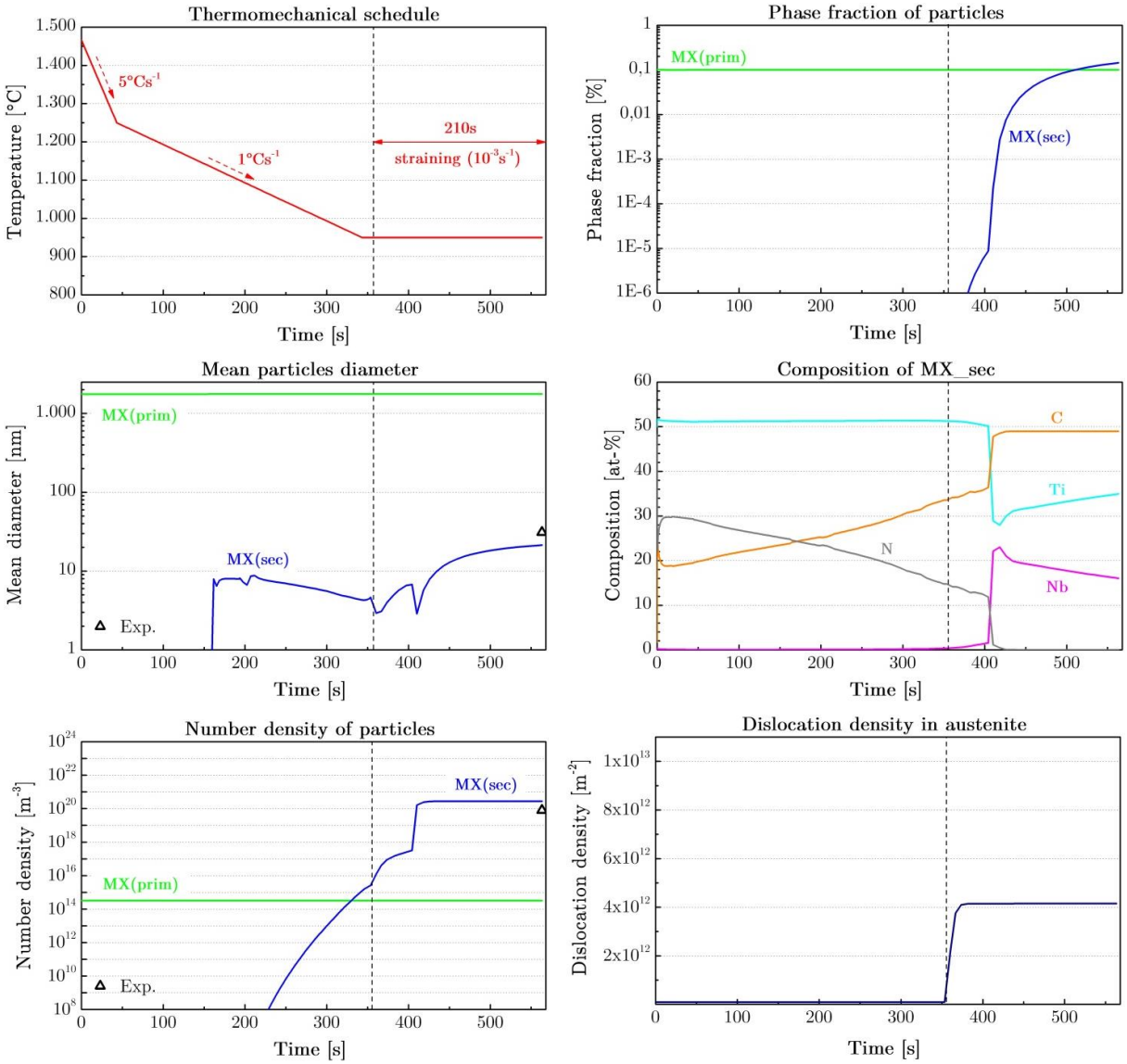

Fig. 77: MatCalc kinetic precipitation calculations during "direct on-cooling" process at 950°C with partially straining for 210s.

As can be seen, secondary Ti-carbonitrides start to nucleate at approximately 1140°C and quickly grow up to around 10nm. On further continuous cooling, the mean radius slightly decreases as the number density of the particles continuously increases. The second slight rise in number density and decrease in mean diameter appears due to strain-induced precipitation

by the increased number of dislocations ($4.1 \cdot 10^{12} m^{-2}$) and available nucleation sites upon deformation (dashed line). A third nucleation at around 400s takes place, thus increasing the particles number density and phase fraction and, in turn, slightly decreasing the particles mean diameter, respectively. This effect eventually occurs due to the change of the chemical composition of the particles, where the C-content increases and the Ti-content markedly decreases. At the same time, the nitrogen of the compound falls to zero and is replaced by niobium thus giving rise to the formation of TiNb-carbides. Then, the particles number density remains constant with a simultaneous continuous particles growth up to 21nm. The resulting chemical composition of the secondary precipitate is 49%C, 35%Ti and 16%Nb (at.-%) with a final phase fraction of 0.14%. Since the number density steadily increases, no coarsening of the particles are therefore observed.

Of particular interest is the precipitation state of the sample, which has been strained at 850°C. Here, considerably more and finer particles of 6nm in mean diameter of roughly spherical shape have been detected, Fig. 78.

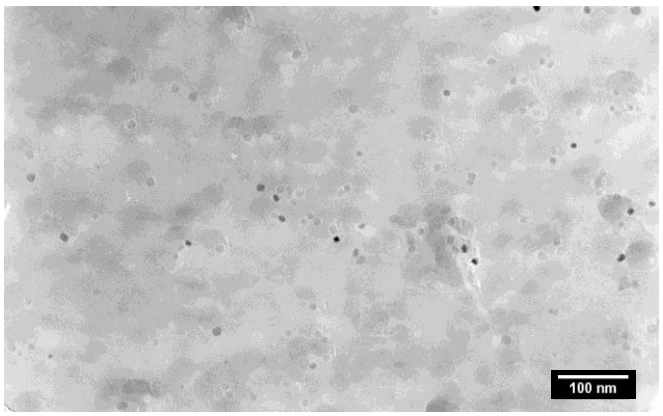

Fig. 78: TEM-image of specimen strained until necking and water-quenched at 850°C.

By simulating the thermomechanical history by means of MatCalc (Fig. 79), this condition becomes comprehensibly apparent, since the deformation at lower temperatures increases the dislocation density in austenite to a greater extend from $1 \cdot 10^{11}$ to $9.9 \cdot 10^{12} m^{-2}$ and therefore the nucleation process during straining. The stepped increase of the number density and the deviations in the mean diameter result from similar effects as previously described for the deformation at 950°C. However, the resulting phase fraction of the secondary precipitates is found to be 0.05%C with a chemical composition of 49%C, 32%Ti and 19%Nb (at.-%). Table 4 summarizes the experimental and simulation results for the mean particle diameter as well as the number density which are in quite good agreement with each other, thus supporting the assumption of a dislocation-assisted particles nucleation.

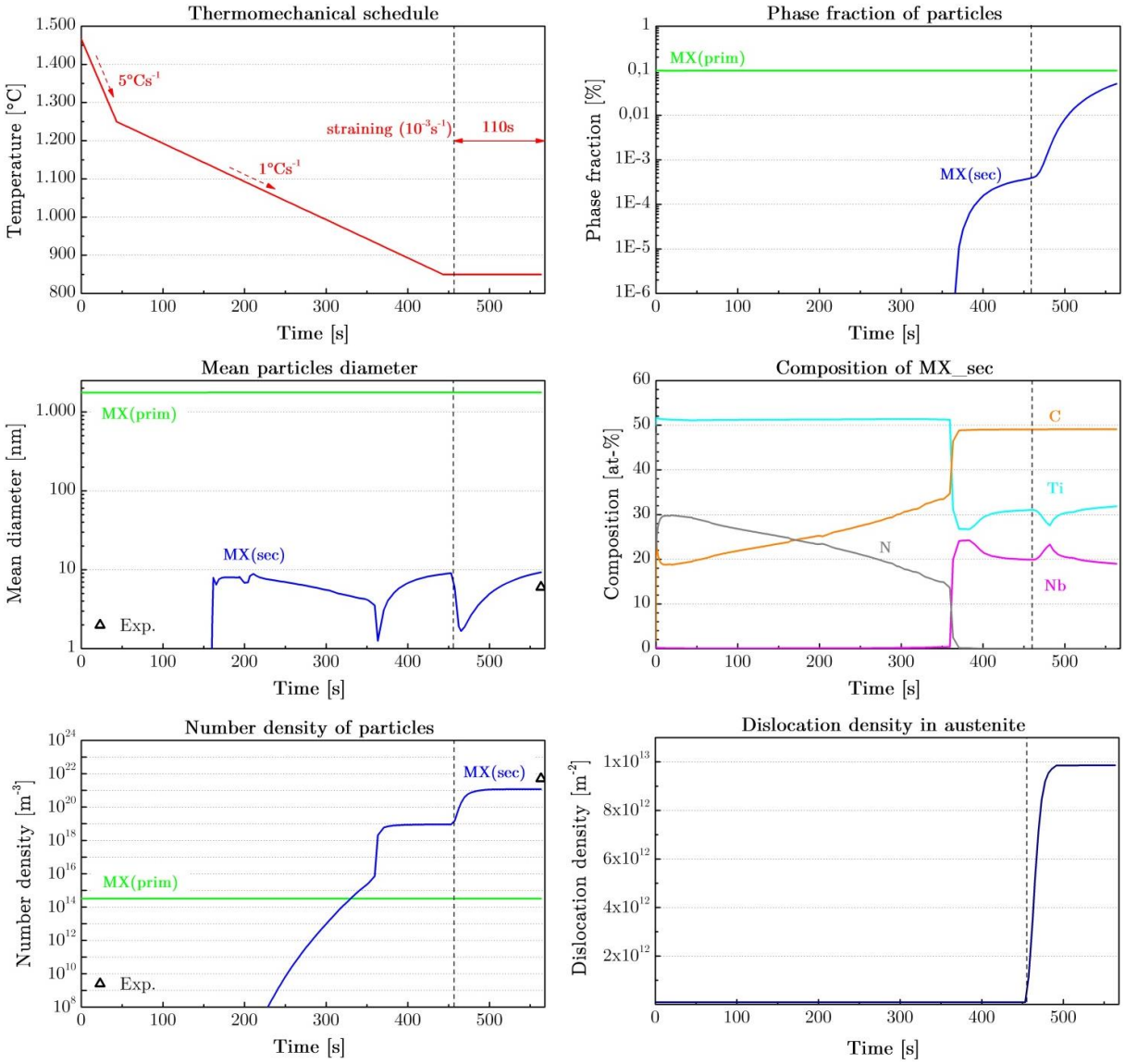

Fig. 79: MatCalc kinetic precipitation calculations during “direct on-cooling” process at 850°C with partially straining for 110s.

Table 4: Comparison of calculated and measured mean particle diameters and number densities.

Testing temperature	Testing method	D [nm]	N_V [m^{-3}]
950°C	TEM	31±4	$8 \cdot 10^{19}$
	MatCalc	21	$3 \cdot 10^{20}$
850°C	TEM	6±3	$5 \cdot 10^{21}$
	MatCalc	9	$1 \cdot 10^{21}$

Moreover, Fig. 80 shows this distinct change in distribution of the experimentally analyzed particles within the two tested microstructures at 950°C and 850°C.

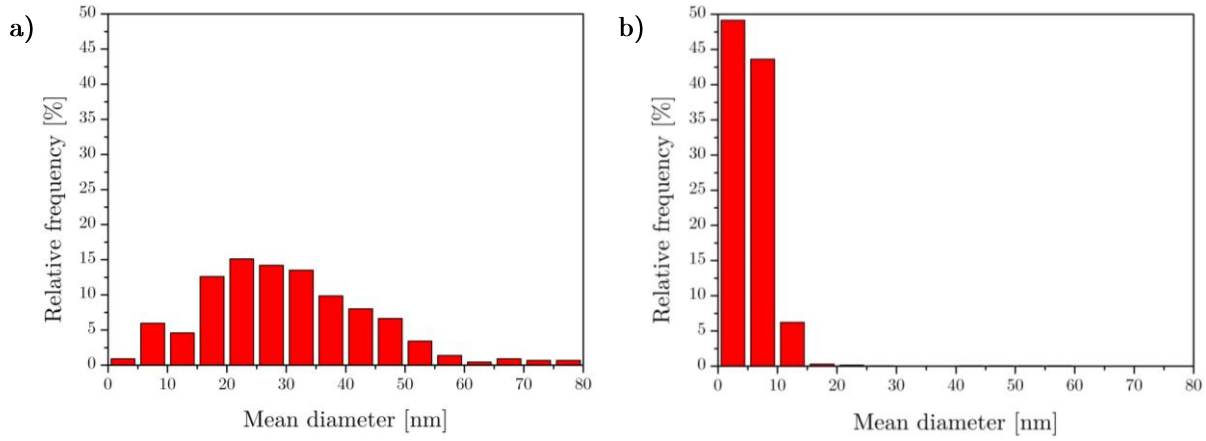

Fig. 80: Histograms of the analyzed particles for specimens tested at a) 950°C; b) 850°C.

On the basis of the above observations, the poor ductility can be mainly attributed to fine dislocation-precipitation, which increases the strength of the austenite grains and therefore the stress within grain boundary regions decreasing the plastic deformability and encouraging austenite grain decohesion by the interlinkage of cavities [22], [62], [97], [110], [111]. This accelerated linking of cavities, primarily around triple-point regions of grain boundaries, induce the typical wedge-type cracking as illustrated in Fig. 50b.

There are only few studies available in literature which report the formation and influence of complex TiNb-precipitates on the hot ductility of Ti-Nb steels after melting and solidification [41], [57], [65], [81], [92], [94], [112]. Luo et al. [81], for instance, have reported a marked deterioration of the ductility by adding 0.015–0.038%Ti to a 0.1%C–1.5%Mn-0.03%Nb–0.005%N steel after melting the specimens in-situ by applying both a direct cooling with $4°Cs^{-1}$ or an undercooling step by 100°C prior to straining. They reported very fine strain-induced TiNb(C,N) with a size of 10nm at 900°C, which led to finer and more frequent precipitation and markedly extended the ductility trough to very poor RA-values within the entire testing regime. Similar observations were found in the work by Banks et al. [65] that an addition of Nb gave rise to poor ductility and which became even worse when Ti was additionally added. This resulted in a finer mean precipitate size and an increased number density. Carpenter et al. [57] reported a continuous decrease of the mean diameter of Ti-Nb-particles in steels with 0.16%C–1.23%Mn-0.019%Nb–0.015%Ti–0.005%N with decreasing testing temperature from 1000°C (43nm) to 850°C (5nm), this also being comparable with the present results summarized in Table 4.

However, many researchers have pointed out that an addition of Ti to Nb-containing steels has a detrimental influence on the hot ductility [57], [64], [65], [81], while, on the

contrary, a slight improvement or no deterioration of the hot ductility have also been reported, depending on the Ti:N ratio, Ti · N product and applied cooling rate [59], [62].

6.1.2 Region 2: Testing temperatures 750–800°C

The distinct drop in ductility within region 2, especially in the case for the low-alloyed steel, can be clearly related to the presence of thin ferrite bands surrounding the austenite grain boundaries during the austenite to ferrite transformation as revealed in Fig. 46. This allows strain concentration in the thin intergranular ferritic phase, as schematically demonstrated in Fig. 81, and accounts for the lowest ductility down to a minimum of 20% RA at 750°C, since ferrite is softer than austenite at the respective temperatures. [10], [22], [31], [74], [88]

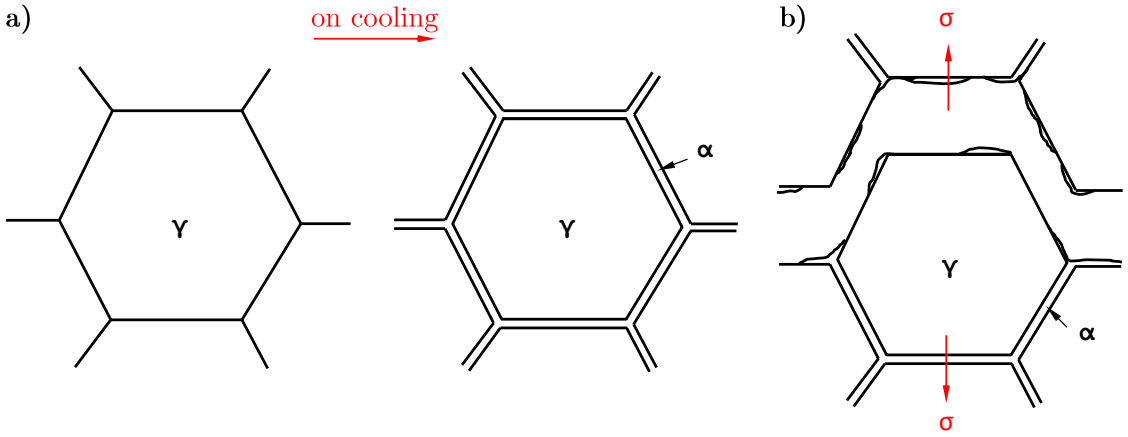

Fig. 81: Embrittlement mechanism within the two-phase austenite-ferrite region.
a) Start of austenite to ferrite transformation along austenite grain boundaries on cooling;
b) Intergranular fracture due to strain concentration along these thin ferrite bands.

However, it rather seems that the increased depth of the ductility trough of the low-alloyed steel is controlled by the coarser grain size as reported e.g. in [73] for a plain C-Mn steel. From a macroscopic point of view, it can be assumed, that the grain separation at the same ferrite film thickness and applied load may be even accelerated when the grain size becomes larger, thus decreasing the ferrite volume fraction. This may avoid a uniform stress distribution or an increased localized stress concentration within the ferrite bands. There are also indications that insufficient deformation induced ferrite between the calculated A_{r3}-(730°C, Fig. 68) and A_{e3}-temperature (820°C, Fig. 64) have been formed during straining to increase the ferrite fraction between 750–800°C, Fig. 46. It should be noted that the calculated A_{r3}-temperature seems to be at least 20°C lower, since a very thin ferrite film of ≤5µm thickness was visible after a holding time of 20s at 750°C, Fig. 46a.

In the case of the Ti-Nb microalloyed steel, it can be suggested that, beside the intergranular ferrite, additional fine dynamic precipitation has the major influence on the hot ductility behavior within the trough and, in turn, concentrating the strain at grain boundary regions [74]. This combined influence of the precipitation may therefore cause the broad shape of the ductility curve as shown in Fig. 42. The slightly higher position of the ductility minimum at 30% RA compared to the low-alloyed steel, on the other hand, may be related to the finer grain size, respectively [21], [91].

6.1.3 Region 1: Testing temperatures 650–700°C

By lowering the testing temperatures, the ductility of the low-alloyed steel rapidly improves to 50% RA between 650–700°C. This can be attributed to the increased amount of ferrite preventing intergranular strain concentration [73]. Mintz suggests that at least 50% transformation induced ferrite prior deformation is required to improve the ductility to values of >40% RA for a similar plain C-Mn steel with 0.15%C and 1.4%Mn [113]. However, this is not the case for the present investigated steel, since the measured ferrite fraction at 700°C after 20s was found to be 3% with a film-thickness of 20µm, Fig. 44a. This discrepancy may be explained by the fast ferrite formation below A_{r3} during testing for a total exposure time of 290s until fracture, eventually showing a ferrite fraction of almost 50%, Fig. 44b. This issue may also be confirmed using the calculated isothermal transformation diagram for the respective steel, Fig. 69. Furthermore, according to the work of Wray [114], the strength difference between γ and α with decreasing testing temperature due to the work hardening effect may have become smaller as well, which reduces local strain concentration and increases the materials ductility.

No or very less recovery of the hot ductility could be observed for the Ti-Nb containing steel in this region, even though the measured grain size was significantly finer with a calculated A_{r3}–temperature being very close to those of the low-alloyed steel. The reason for this is probably due to the sluggish increase in ferrite fraction on cooling because of the lower γ-finish temperature, Fig. 70, or to the combined deteriorating effect of precipitates.

6.1.4 Summary

This section summarizes the results of the hot ductility investigations for both steel alloys during the direct on-cooling after preceding melting and solidification. As proposed by Mintz et al. [11] (see section 3.2), the RA-value should be in excess of 40% to avoid surface cracking

during the respective thermomechanical history. On this basis, Fig. 82 and Fig. 83 outline the critical temperature ranges for embrittlement plus a representative image at which tensile straining should be avoided. For the sake of completeness, the equilibrium transformation temperatures A_{e1} and A_{e3} have been added to the figures as well.

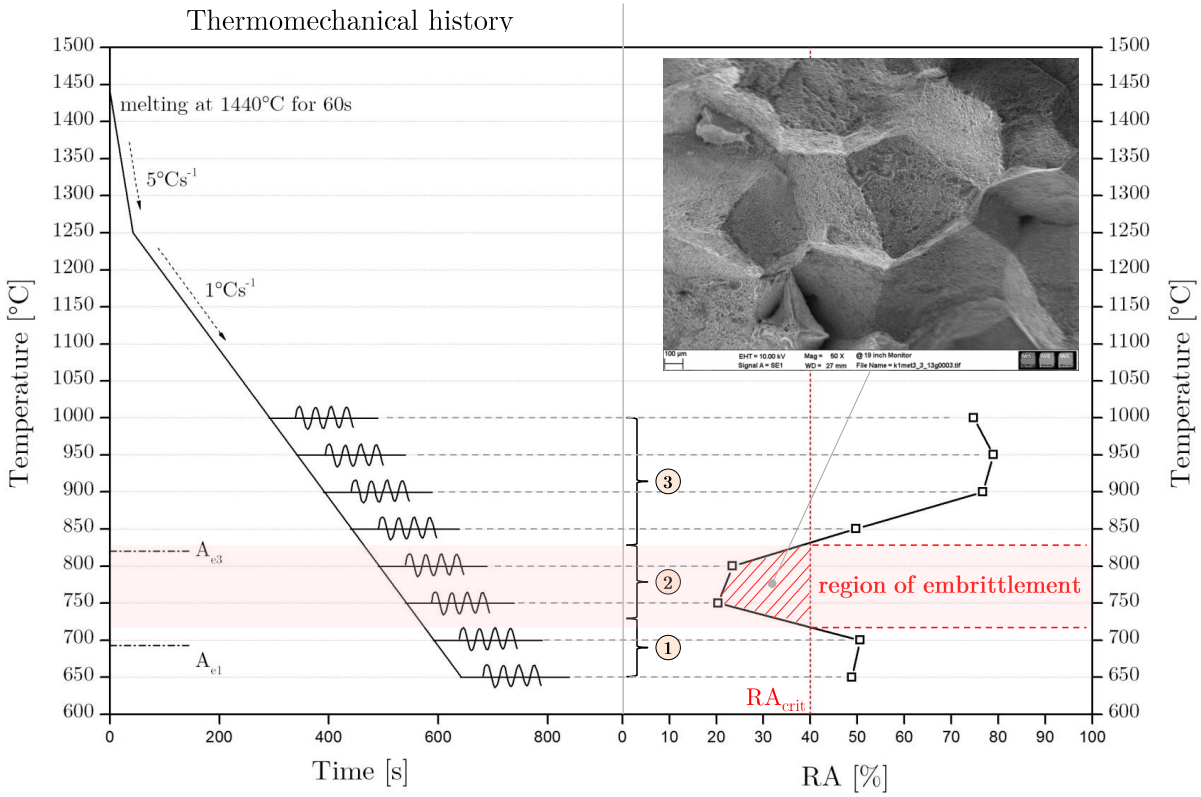

Fig. 82: Summarized illustration of the hot ductility results for low-alloyed steel during direct on-cooling treatment.

It can be seen, that the region of embrittlement for the low-alloyed steel is roughly between 700°C and 850°C, whereas the Ti-Nb microalloyed steel evinces a distinct broader critical region of 650°C and 900°C.

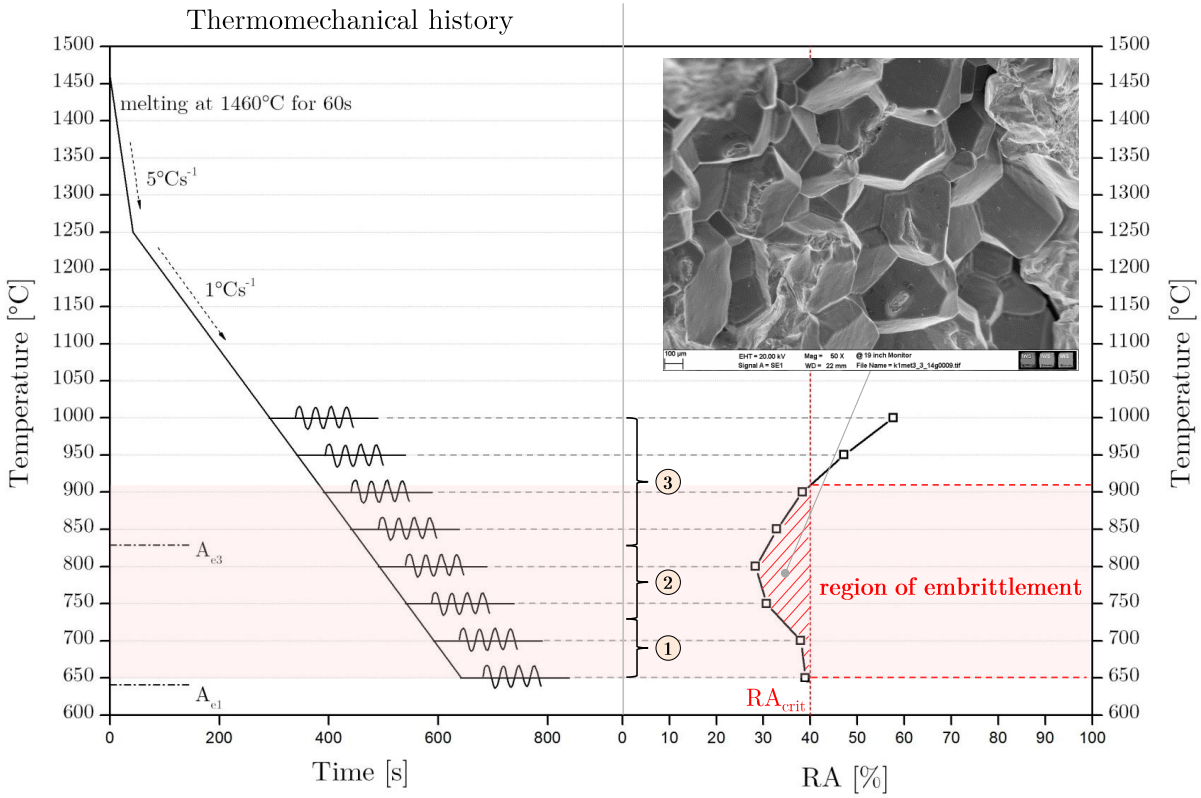

Fig. 83: Summarized illustration of the hot ductility results for Ti-Nb microalloyed steel during direct on-cooling treatment.

6.2 Solution treatment – Ti-Nb microalloyed steel

The results of the solution treatment experiments are discussed in the following section, starting with region 1 (testing temperatures 650–700°C), whereas regions 2 and 3 have been merged into one (testing temperatures 750–1000°C).

6.2.1 Region 1: Testing temperatures 650–700°C

As illustrated in Fig. 52, the hot ductility within the low-temperature end is slightly improved by 13% RA once a simple solution treatment process has been applied. This behavior can be primarily related to the finer mean grain size being about twice as small (195µm) as observed during the direct on-cooling process (385µm) probably due to the remaining and undissolved Ti-rich particles inhibiting grain growth on heating, since these precipitates may be stable up to the materials liquidus temperature, Fig. 72. Consequently, this results in an increase in grain boundary areas favoring an accelerated nucleation and growth of ferrite up to 68% at 650°C, Fig. 53.

6.2.2 Regions 2–3: Testing temperatures 750–1000°C

According to the diagram shown in Fig. 52, reheated tensile specimens with a refined austenite grain structure did not give rise to an improved ductility behavior across a broad temperature range from 800°C to 1000°C as would have been expected. Above 950°C, the hot ductility becomes even worse than the one from direct on-cooling, supposing that the ductility is predominantly controlled by the deteriorating effect of fine second phase particles.

Luo and Zhao [115] observed similar poor ductility, when they investigated the influence of high amounts of titanium (0.04–0.085wt.-%) on the hot ductility of reheated 0.2%C–Mn–Cr–Al steel samples with 0.008%N (Ti:N ratios=5.5, 8.85 and 10). In these steels, precipitates mainly consisted of $Ti_4C_2S_2$ and Ti(CN). Fine Ti(CN)-particles were only found in the steel with a Ti/N ratio of 5.5, which were extensively finely distributed throughout the matrix (<50nm) during deformation. This steel evinced the worst ductility behavior with a broad ductility trough (RA<40% from 700°C to 1000°C). With increased Ti/N ratios up to 10, the ductility was slightly improved or has changed a little, when coarse $Ti_4C_2S_2$-precipitates were preferentially formed which could remove more sulfur atoms from the matrix and boundaries [16], [115].

In the present case, it can be assumed that the much greater Ti-content of the steel (Ti:N ratio=18.43) primarily contributes to a considerable increase of both the number density and amount of solute Ti being able to precipitate out of the supersaturated solid solution, forming fine and detrimental MX-particles upon the thermomechanical treatment. This may be better explained by plotting the ultimate tensile strengths (R_m) into the graph as illustrated in Fig. 84. Especially at 950–1000°C, the deteriorating effect of precipitates seems to outweigh the positive influence of the fine grain structure on the hot ductility assuming that much more precipitates may have been formed during the respective heat treatment giving less RA-values. This again increases the stress within grain boundary areas relative to that within the grain interior and encourages the formation of wedge cracks as presented in Fig. 55b and Fig. 55c. The effect of grain refinement on the hot ductility seems to become more relevant as the temperature decreases below 800°C. However, further microstructural examinations would be necessary to fully confirm these assumptions.

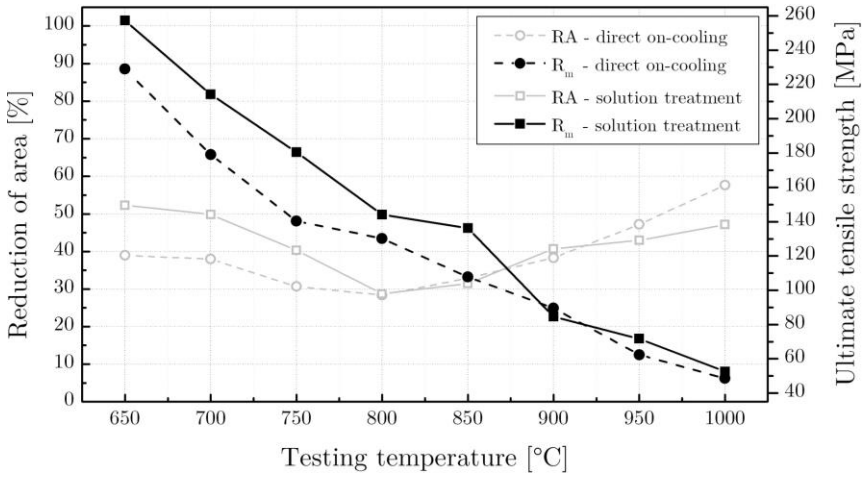

Fig. 84: Hot ductility curves and ultimate tensile stresses for Ti-Nb containing steel after solution treatment and direct on-cooling within regions 1 and 3.

6.2.3 Summary

Fig. 85 highlights the observed results of the hot tensile experiments during the solution treatment process which in turn reveals poor ductility up to 900°C. Refining the grain size, however, enables the ductility to quickly recover towards lower testing temperatures.

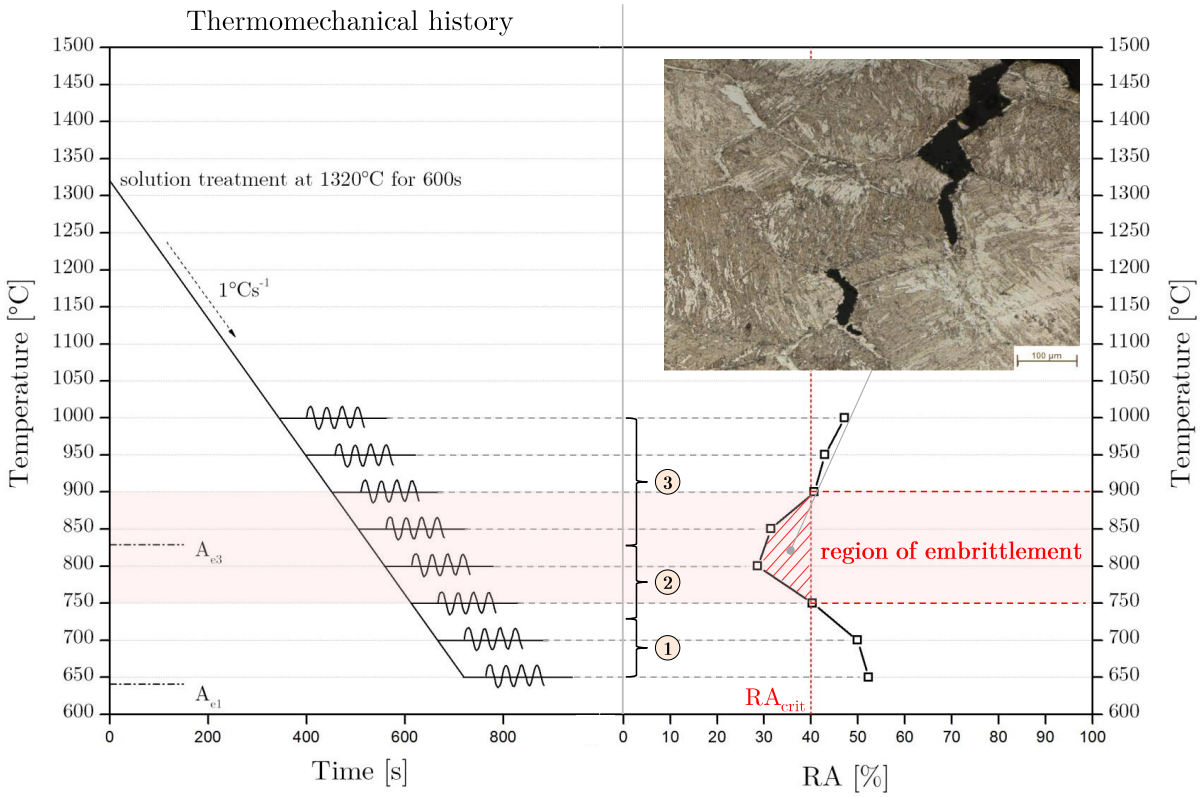

Fig. 85: Summarized illustration of the hot ductility results for Ti-Nb microalloyed steel during solution treatment.

6.3 Slow cooling – Ti-Nb microalloyed steel

The results obtained within regions 1 to 3 have been entirely merged into one section as will be discussed in the following.

6.3.1 Regions 1-3: Testing temperatures 700–1000°C

The slow cooling process appears to not substantially affect the ductility behavior within the whole testing temperature regime as illustrated in Fig. 56. The deviation of the measured RA at 700°C, for instance, was found to be only 6%. This also applies for the testing temperature region above 800°C, even though it has often been argued that a Ti:N above the stoichiometric ratio of 3.42:1 and/or by utilizing a slow cooling rate should encourage coarse precipitation resulting in an improved ductility [35], [57], [59], [62], [65], [81], [92]. However, Fig. 86 presents the results of the TEM examinations taken from carbon extraction replicas of specimens tested at 950°C and 850°C, respectively.

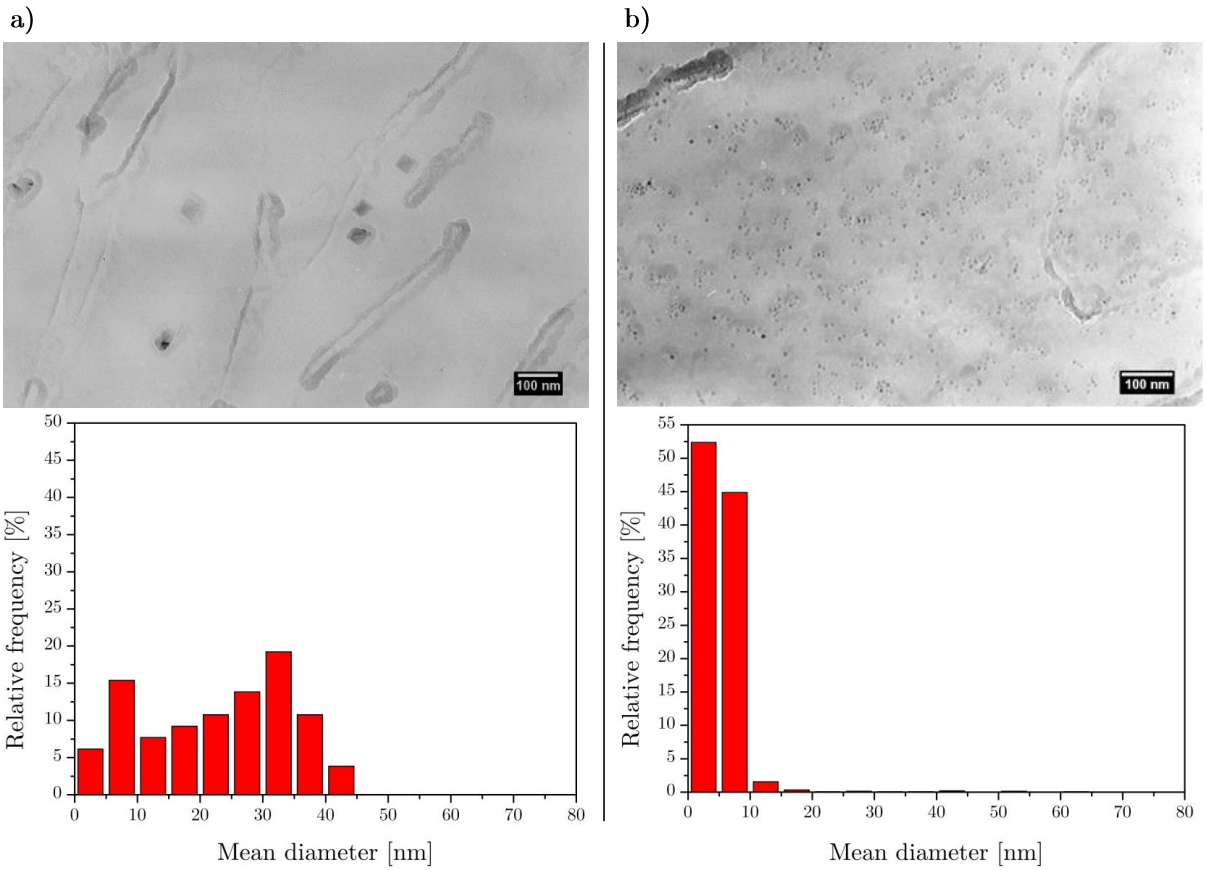

Fig. 86: a) TEM-images and histograms of analyzed particles on specimen tested at a) 950°C and b) 850°C.

In contrast to literature, no significant differences in the precipitates size could therefore be observed which would indicate any significant coarsening of the precipitates compared to steels being subjected to the direct on-cooling process. As can be seen at 850°C (Fig. 86b), the microstructure appears to contain rather a larger number density of homogeneously distributed Ti-Nb-rich precipitates with a mean diameter of 6nm. The mean particles diameter at a test temperature of 950°C, on the other hand, was found to be 26nm.

Associated kinetic calculations by MatCalc using the same setup parameters as presented in section 6.1.1 manifest this poor ductility behavior if fine TiNb-rich precipitates at dislocations along with a high volume fraction are present, Fig. 87.

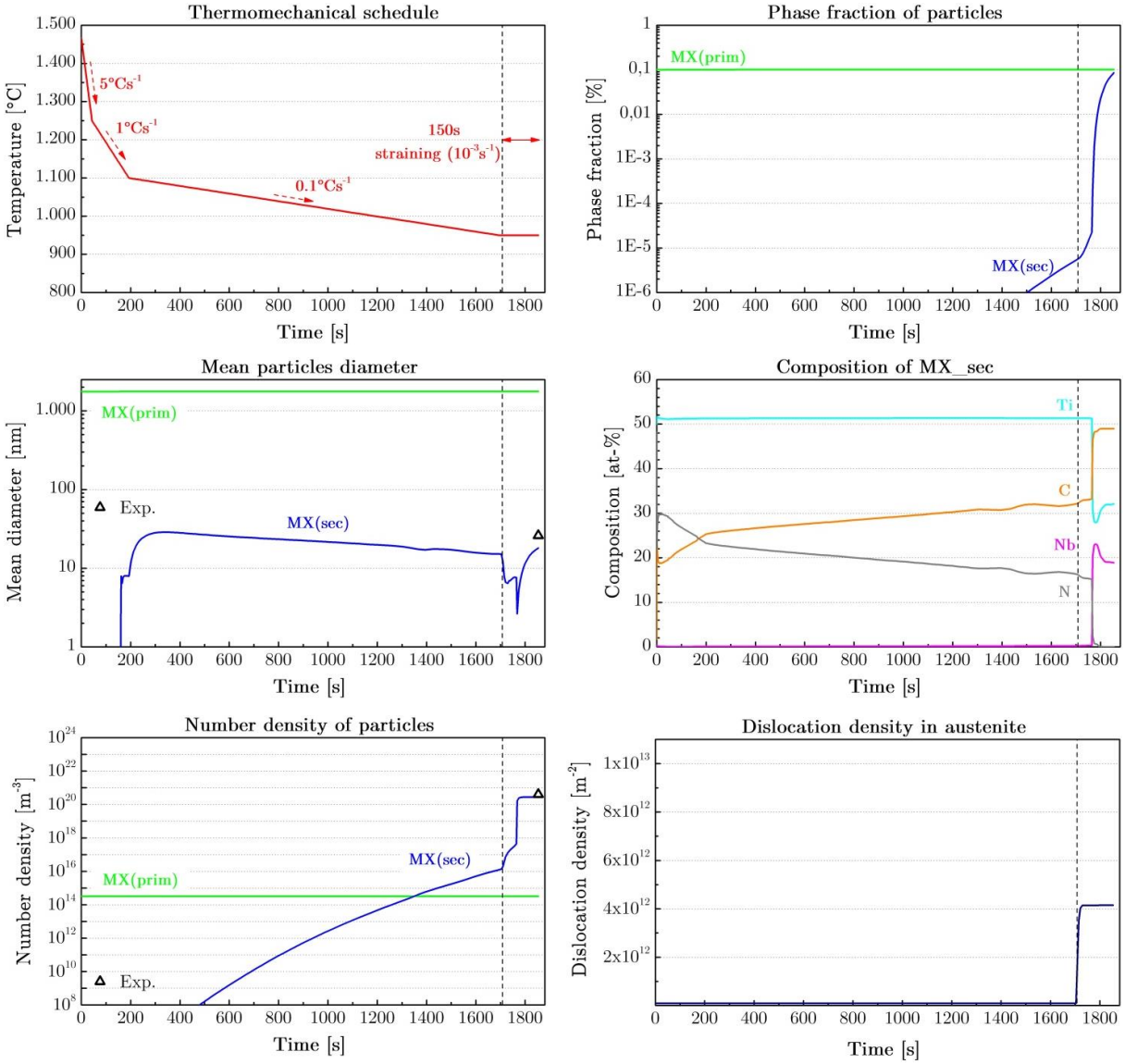

Fig. 87: MatCalc kinetic precipitation calculations during "slow cooling" process at 950°C with partially straining for 150s.

As observed during the direct on-cooling process, a slight increase of the number density by one order of magnitude appears upon straining. As a consequence, the mean particles diameter becomes reduced and further decreases to around 2nm with the sudden change of the chemical composition from TiCN to TiNbC shortly after deformation. Afterwards the particles continue to grow to 18nm and reach a final particles number density of $3 \cdot 10^{20} m^{-3}$. The resulting phase fraction of the precipitates is found to be 0.08% with a chemical composition of 49%C, 32%Ti and 19%Nb, respectively.

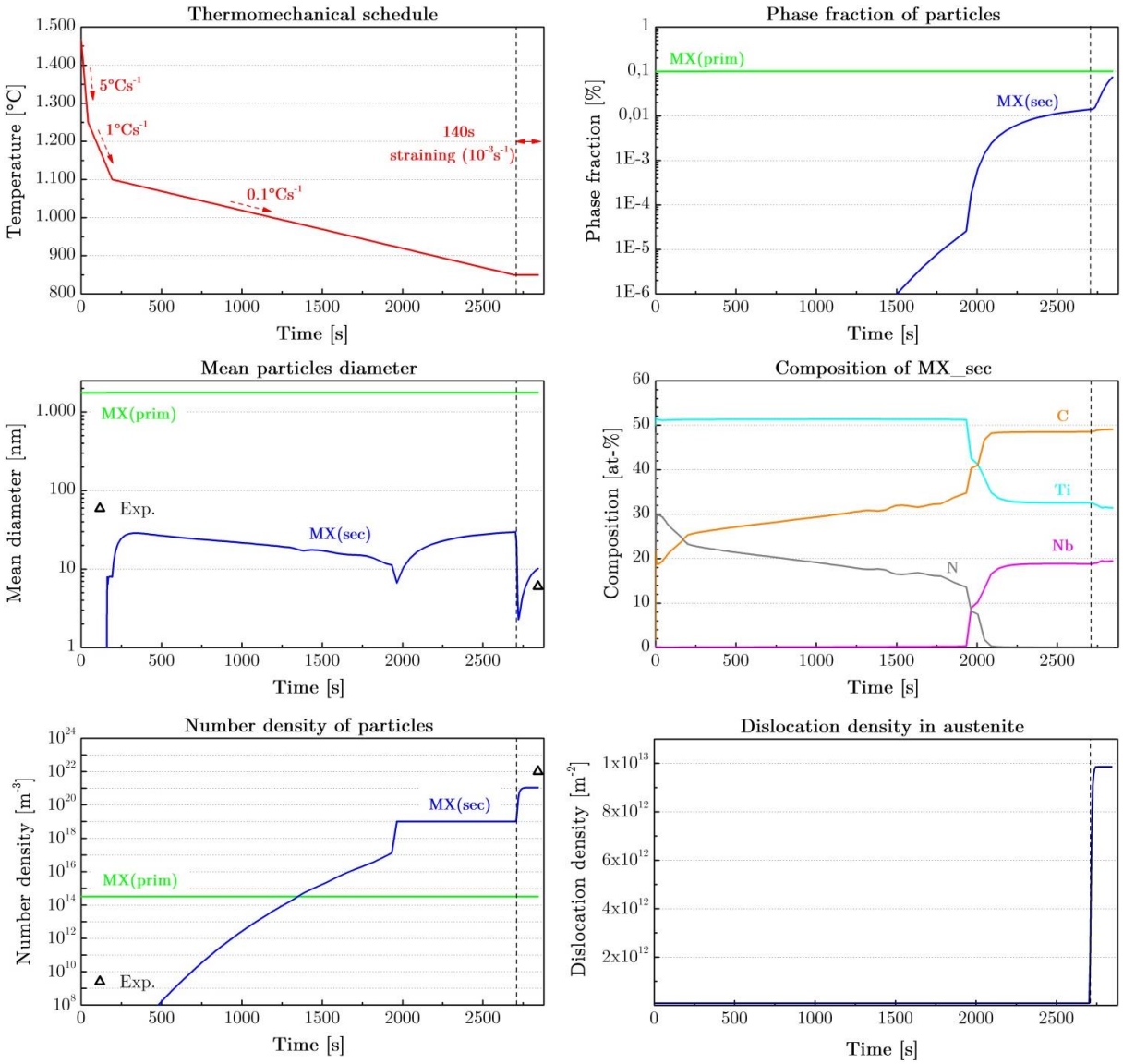

Fig. 88: MatCalc kinetic precipitation calculations during "slow cooling" process at 850°C with partially straining for 140s.

According to the calculations, similar evolution of the TiNb-precipitates can be observed on further cooling to 850°C, except that the dislocation density in austenite increases by a greater amount when a deformation is introduced as stated previously. Thus, the number

density rises up to $1 \cdot 10^{21} m^{-3}$ and the mean diameter decreases to 10nm until the simulation stops after 140s. The resulting phase fraction of the precipitates appears to be 0.07%, Fig. 88.

Again, the simulated mean particle diameters as well as the number densities obtained for the slow cooling process are very consistent with the experimental TEM-results, Table 5.

Table 5: Comparison of calculated and measured mean particle diameters and number densities.

Testing temperature	**Testing method**	**D [nm]**	**N_V [m^{-3}]**
950°C	TEM	26±12	$4 \cdot 10^{20}$
	MatCalc	18	$3 \cdot 10^{20}$
850°C	TEM	6±3	$1 \cdot 10^{22}$
	MatCalc	10	$1 \cdot 10^{21}$

The observations in the present work are in relative good agreement with the results reported by Carpenter et al. [57], who investigated the influence of different thermal patterns on the hot ductility of 0.16%C-1.23%Mn-0.019%Nb-0.0.15%Ti steels (Ti:N stoichiometric=1.42) after melting the specimens in-situ. The mean diameter of the assessed Ti-Nb-particles were 12nm and 11nm at 950°C for cooling rates $3.33°Cs^{-1}$ and $1.67°Cs^{-1}$, respectively, while 4nm and 5nm were measured at 850°C. A coarsening of the precipitates could only be achieved when additional thermal oscillations were introduced on cooling. This improvement has also been confirmed by Banks et al. [92] who investigated the influence of various thermal histories on the hot ductility of in-situ melted Ti-Nb steels. Nevertheless, despite the extensive precipitation observed in the present steel, the reason for the overall slight improvement of about 10% RA has yet to be clarified.

6.3.2 Summary

Fig. 89 gives an overview of the results during the slow cooling treatment with a little less pronounced embrittlement region (~750–850°C) compared to the direct on-cooling and solution treatment cycles.

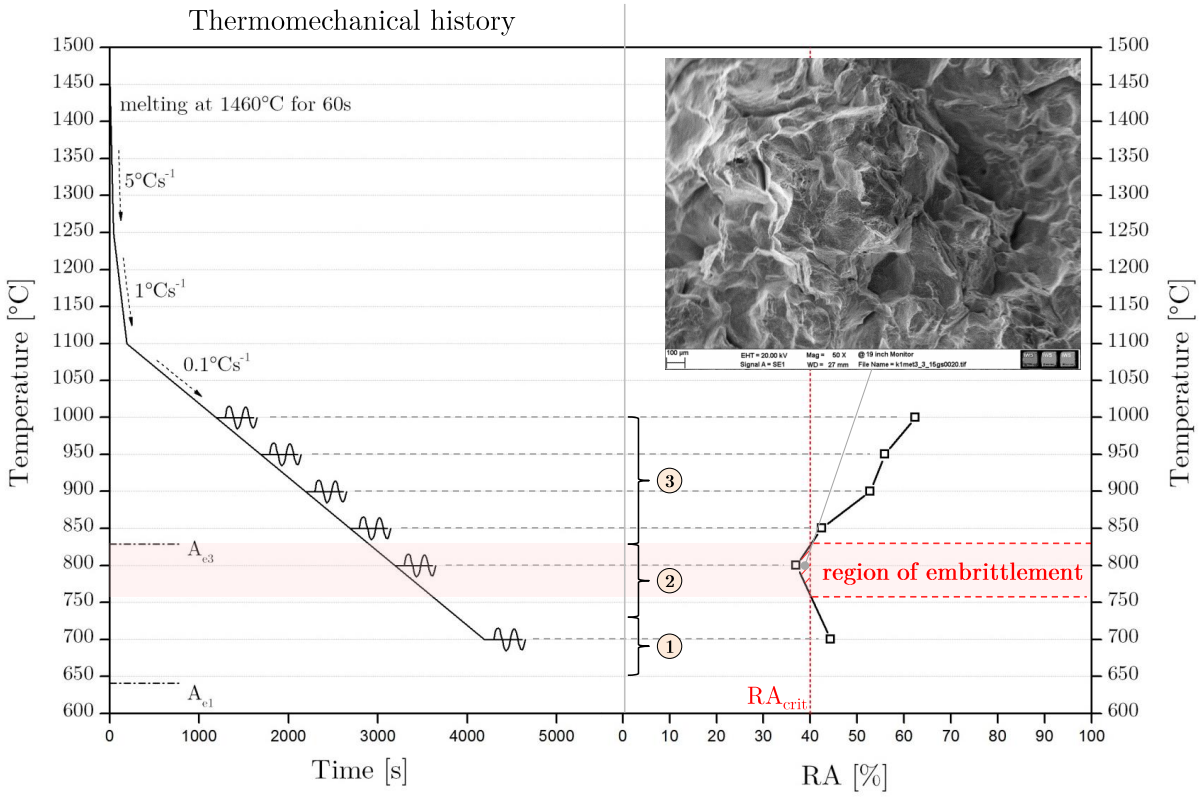

Fig. 89: Summarized illustration of the hot ductility results for Ti-Nb microalloyed steel during slow cooling treatment.

6.4 Surface structure control cooling – Ti-Nb microalloyed steel

The results of the surface structure control cooling experiments are discussed in the following, beginning with region 1 (testing temperatures 650–700°C), whereas regions 2 and 3 have been merged into one for better legibility.

6.4.1 Region 1: Testing temperatures 650–700°C

The concept of the SSCC has been adopted to control the microstructure by means of a second recrystallization from cooling and reheating, since it has been reported to significantly improve the ductility by refining the microstructure and suppressing the formation of intergranular ferrite compared to steels which have been directly cooled to test temperature [94], [116]–[119]. Basically, this gives a higher ductility especially within the low-temperature end, but only if specimens are sufficiently cooled below the A_{r3}-temperature [117], [119]. This behavior also applies for the present investigated Ti-Nb-steel, since the reverse α–γ phase transformation on subsequent heating (Fig. 41) produces much finer grains with homogeneously distributed ferrite throughout the microstructure allowing the ductility to

fully recover at lower deformation temperatures. As shown in Fig. 43b, almost 100% ferrite is present after fracture at 650°C with a reduction of area above 70% confirming the positive effect of the SSCC for this region.

6.4.2 Regions 2–3: Testing temperatures 750–1000°C

However, at testing temperatures above 700°C, the materials hot ductility becomes seriously impaired with a ductility trough extending from 750°C up to 1000°C. The revealed results within the austenite region are partly inconsistent with the results reported in most literature [94], [116], [118], [120]. Kato et al. [94], for instance, who used almost equal process parameters as in the current work, concluded that the SSCC led to both uniform ferrite and precipitate distribution on their investigated 0.07%C–1.5%Mn–0.02%Nb–0.01%Ti–steel which caused a distinct recovery of the ductility over the whole testing temperature range. Unlike during the mild cooling process (similar to the direct on-cooling process), in which they observed fine grain boundary precipitation, homogeneously distributed TiNb-carbonitrides (<20nm) have been found in their investigated steel. On the contrary, Walmag et al. [119] could not observe any improvements in the austenitic regime for 0.09%C–0.71%Mn–0.013%Nb–steel by the double phase transformation. The ductility was still poor and the trough was even widened although the grain was refined. It was assumed, that the respective cooling and heating paths enhanced the final amount of precipitates than during the conventional on-cooling treatment. Obviously, this statement coincides with the present intensified embrittlement in the Ti-Nb alloyed steel which can be, in turn, related to the presence of considerably denser TiNb-precipitates compared to the direct on-cooling process. Similar observations have been recently made by Lückl et al. [117], who obtained very fine and dense TiNb(CN)-precipitates on the identical steel alloy by using the same thermal history of SSCC but without preceding melting. The process caused the ductility to deteriorate up to 1050°C due to finer and denser precipitation compared to the mild cooling process and was confirmed by supplementary kinetic MatCalc-calculations. The simulations have shown that intense nucleation of fine TiNb-carbonitrides has been promoted during the holding time in the ferritic range which led to a reduced ductility.

The results of the maximum austenite stresses during SSCC as a function of temperature are given in Fig. 90. The significant stress increase compared to the resulting stress from the direct on-cooling treatment may be again predominantly attributed to the increased pinning of dislocations due to precipitates thus allowing fast formation of cavities preferably at grain corners and making it easier for cracks to interlink.

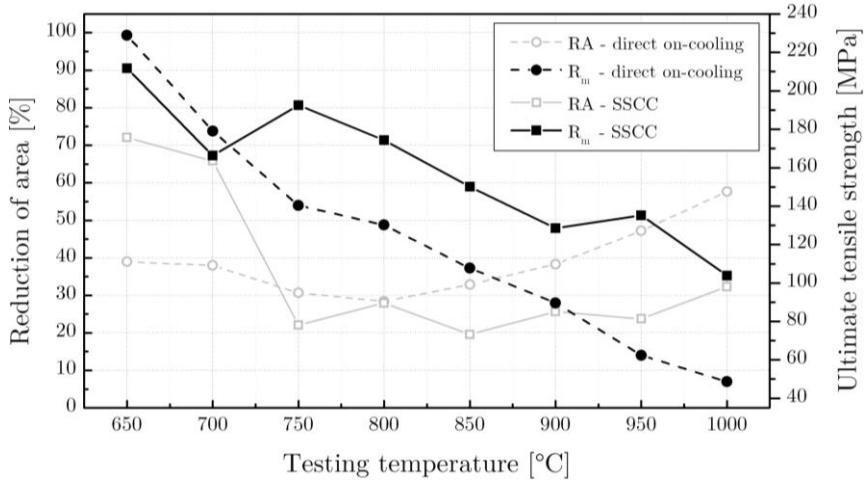

Fig. 90: Hot ductility curves and ultimate tensile stresses for Ti-Nb containing steel after SSCC and direct on-cooling within regions 1 and 3.

6.4.3 Summary

Fig. 91 illustrates the ductility curve for the SSCC treatment including the distinct embrittlement being initiated above 700°C up to the highest testing temperature of 1000°C.

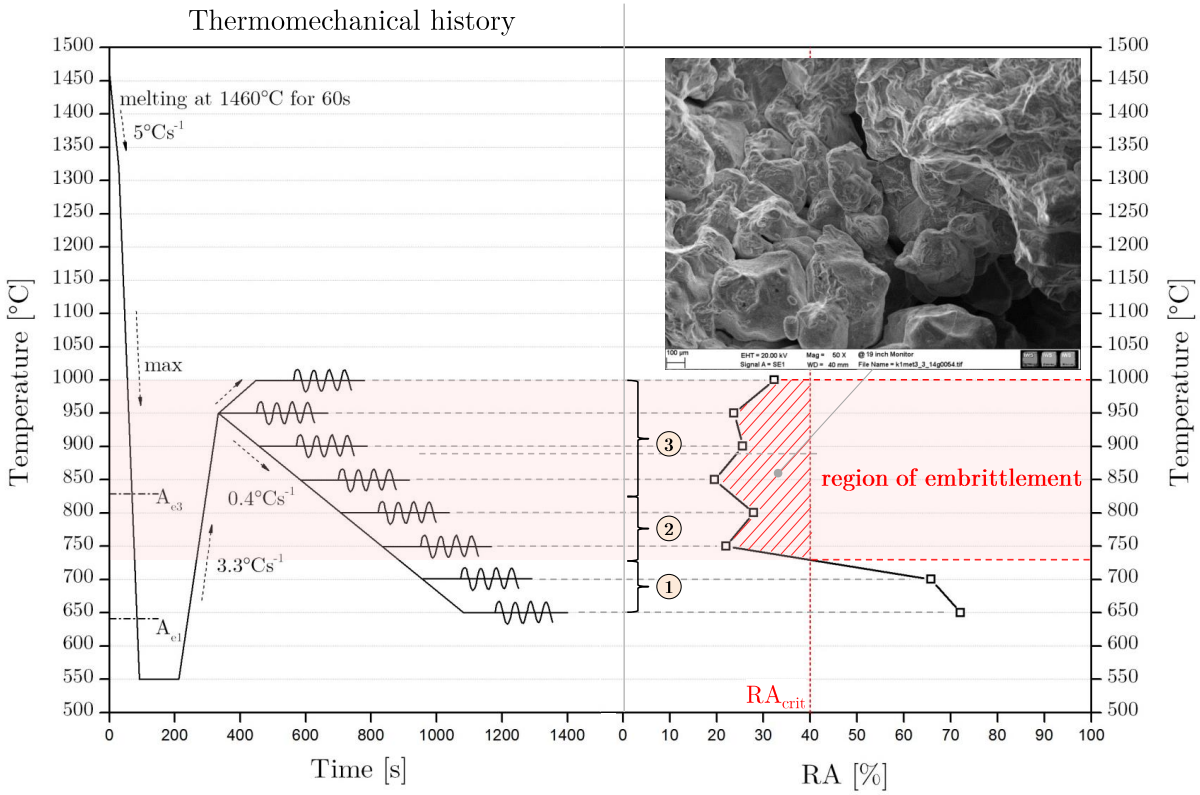

Fig. 91: Summarized illustration of the hot ductility results for Ti-Nb microalloyed steel during SSCC treatment.

7 Summary and conclusions

The hot ductility of low- and Ti-Nb microalloyed steel exposed to different thermomechanical histories was investigated in order to evaluate the tendency for transverse surface cracking during the continuous casting process. In the course of preliminary conventional hot tensile tests with preceding melting and solidification using the casting simulator BETA 250-5, it was observed that the Ti-Nb microalloyed steel evinced very poor ductility behavior with a ductility trough extending over the entire testing temperature range. The reduced ductility within the austenite region occurred due to fine and dense TiNb-precipitates which were homogeneously dispersed throughout the whole microstructure. By contrast, the low-alloyed steel exhibited a deeper but narrower ductility trough with improved ductility towards both lower and higher testing temperatures. The microstructural observations on these samples, which have been tested within the ductility trough, have shown that the embrittlement was characterized by intergranular cracking through thin ferrite films along austenite grain boundaries.

Supplementary hot ductility investigations on the Ti-Nb alloyed steel without remelting the specimens prior to cooling, showed no improvement in ductility behavior at the high-temperature-end, even though the grains were significantly refined. This indicated that, in turn, fine TiNb-precipitation appeared to primarily control the hot ductility within the austenite region and making the material sensitive to intergranular fracture by grain boundary segregation.

One of the important findings of the present work was the fact that a slow cooling process below 1100°C at $0.1°Cs^{-1}$ did not lead to any coarsening of the existing TiNb-precipitates which would have probably resulted in improved ductility. The results from microstructural TEM-examinations have shown that the excess amount of Ti together with the presence of Nb favored an accelerated nucleation of TiNb-precipitates on decelerated cooling. Further computer simulations by means of MatCalc with dislocation-assisted approaches could fully support the enhanced nucleation during straining and the dislocation-pinning effect of Ti-Nb precipitates impeding ductile deformation. The kinetic calculations showed also good agreement with the experimental TEM results.

It became even obvious, that certain thermal histories such as the surface structure control cooling pattern could promote much more and intense TiNb-precipitation, severely deteriorating the hot ductility within the two-phase austenite-ferrite as well as within the single-austenite region regardless of a much finer persisting microstructure. However, the SSCC-process caused the hot ductility to fully recover at lower testing temperatures due to sufficiently formed ferrite, capable of outweighing the negative influence of fine TiNb-precipitation. The following Table 6 gives an overview of the critical temperature ranges at which the materials are expected to be prone to cracking during the respective thermomechanical treatments and summarizes the results of the hot ductility experiments.

Table 6: Summary of hot ductility investigations for low- and Ti-Nb alloyed steel.

Steel	**A_{c1} [°C]**	**A_{e3} [°C]**	**Thermo-mechanical history; grain size**	**Ductility minimum**	**Crit. temperature region (<40% RA); major causes for embrittlement**	**Recommended straightening/ unbending temperatures (>50% RA)**
Low-alloyed steel	693	820	direct on-cooling; 1140µm	750°C (RA=20.4%)	725–825°C; thin α along γ grain boundaries	>850°C <700°C
Ti-Nb microalloyed steel	641	829	direct on-cooling 385µm	800°C (RA=28.4%)	650–900°C; fine and dense Ti-Nb precipitation; thin α along γ grain boundaries	>950°C
			slow cooling; grain size similar to direct on-cooling	800°C (RA=37.0%)	750–825°C; fine and dense Ti-Nb precipitation	>900°C
			SSCC; not feasible	850°C (RA=19.6%)	725–1000°C; fine and dense Ti-Nb precipitation [117]	<700°C
			solution treatment; 195µm	800°C (RA=28.7%)	750–900°C; fine and dense Ti-Nb precipitation thin α along γ grain boundaries	

Conclusions

- The possibility of water quenching on the hot tensile machine BETA 250-5 has been successfully implemented within the scope of the present work. This enables an appropriate “freezing” of the microstructure for useful subsequent metallographic examinations, which was not feasible before.
- The second ductility minimum in both investigated steels appears within the two-phase ferrite-austenite region. This allows strain concentration within thin intergranular bands of ferrite once an external stress is applied.
- High quantities of Ti in a Nb-containing low-carbon steel does not improve the materials hot ductility to preclude any transverse surface cracking during continuous casting, as the test material is subjected to thermo-mechanical histories similar to direct on-cooling, slow cooling or SSCC-process. Therefore, it cannot be necessarily ruled out that the same steel alloy without additions of Ti and Nb may possess a better hot ductility.
- It has been shown that a ten times slower cooling rate below 1100°C in this alloy composition does not lead to an improvement of the hot ductility compared to the conventional direct on-cooling process, since it still allows permanent nucleation of fine and dense Ti-Nb precipitation without any considerable coarsening of the particles.
- Refining the grain size of the Ti-Nb microalloyed steel does not result in improved ductility within the austenite region, but it accelerates the formation of α-ferrite allowing the ductility to fully recover at lower testing temperatures.
- MatCalc provides a good estimation and valuable information about the precipitation phenomena in steels during thermomechanical treatments.
- Hot ductility depends on both size and volume fraction of second phase TiNb-particles. Increasing the volume fraction or decreasing the mean particles diameter results in deterioration of the hot ductility.
- The preceding melting process and the resulting solidification cavities during tensile testing may quantitatively decrease the RA-values due to the internal notch effect, but it is expected to have minor influence on the general course of the ductility curve in the present study.

8 Outlook and commercial implications

Laboratory hot ductility experiments, in which the test materials are often exposed to continuous cooling to deformation temperatures, only roughly reflect real industrial casting conditions, even if in-situ melting has been applied. This oversimplification does not consider e.g. any complex thermal oscillations which arise on the strand surface within the secondary cooling zone prior to straightening or unbending. An improved physical simulation of the thermomechanical history may therefore influence the precipitation behavior of Ti-containing particles which control the hot ductility. As reported by Carpenter et al. [57] and Banks et al. [65], alternating cooling cycle promotes the formation of coarse TiNb-precipitation resulting in improved ductility compared to Ti-free steels and better validates the beneficial effect of Ti on reducing the cracking propensity during commercial continuous casting [22], [52]. Apart from that, the positive influence of Ti on the hot ductility may be further achieved when the Ti:N ratio becomes significantly decreased in order to limit the phase fraction of Ti-rich precipitates upon cooling and deformation. However, further hot tensile tests with modified temperature-profiles and accompanying extensive numerical simulations by means of MatCalc as well as microstructural investigations must be performed to gain a better understanding of the precipitation behavior in the Ti-Nb-alloyed steel. Nevertheless, the more experience and data can be gained and collected, the better the estimations and forecasts will become for industrial applications in order to save e.g. expensive casting trials. It is also worth noting that due to the restricted castability at voestalpine Stahl GmbH, both investigated steels in the present study are not directly comparable in the chemical compositions. Therefore, appropriate examinations of the same microalloyed steel but without additions of Ti and Nb would provide better reliable information regarding the influence of only Ti, Nb or of both microalloying elements on the hot ductility behavior.

According to the current assessments, it is recommended to straighten the steel alloys well below the A_{r3}-temperatures, if the continuous caster is appropriately designed to sufficiently withstand the higher forces during operation. The low-alloyed steel, on the other hand, may be suited to be straightened within its austenite regime as well, but only if any risk of unexpected outbreak of the melt can be totally and securely excluded from the process.

9 List of literature

[1] World-Steel-Assocation, “World Steel Association - Yearbook archive.” [Online]. Available: http://www.worldsteel.org/statistics/statistics-archive/yearbook-archive.html. [Accessed: 13-Jul-2015].

[2] R. D. Pehlke, “Steel Continuous Casting,” in *ASM Handbook, Volume 15: Casting*, ASM International, 2008, pp. 918–925.

[3] K. Schwerdtfeger, *Metallurgie des Stranggießens*. Verlag Stahleisen mbH, Düsseldorf, 1992.

[4] H. Schrewe, *Stranggießen von Stahl: Einführung und Grundlagen*. Verlag Stahleisen mbH, Düsseldorf, 1987.

[5] J. K. Brimacombe and K. Sorimachi, “Crack Formation in the Continuous Casting of Steel,” in *Continuous Casting - Heat Flow, Solidification and Crack Formation*, Iron & Steel Society of AIME, 1984, pp. 199–214.

[6] R. Steffen, W. Dahl, R. Flesch, H. Litterscheidt, F. Rakowski, P. Scheller, and E. Sowka, *Hochtemperatureigenschaften und Rissbildung beim Stranggießen*. 1999.

[7] K. Schwerdtfeger, *Rissanfälligkeit von Stählen beim Stranggießen und Warmumformen*. Verlag Stahleisen mbH, Düsseldorf, 1994.

[8] W. T. Lankford, “Some Considerations of Strength and Ductility in the Continuous-Casting Process,” *Metall. Mater. Trans. B*, vol. 3, no. 6, pp. 1331–1357, 1972.

[9] Committee on Technology, *Continuous Casting of Steel 1985 - A Second Study*. International Iron and Steel Institute, 1986.

[10] J. K. Brimacombe and K. Sorimachi, “Crack Formation in the Continuous Casting of Steel,” *Metall. Trans. B*, vol. 8, pp. 489–505, 1977.

[11] B. Mintz, “Importance of Ar3 temperature in controlling ductility and width of hot ductility trough in steels, and its relationship to transverse cracking,” *Mater. Sci. Technol.*, vol. 12, pp. 132–138, 1996.

[12] H. G. Suzuki, S. Nishimura, and S. Yamaguchi, “Physical Simulation of the Continuous Casting of Steels,” in *Physical Simulation of Welding, Hot Forming and Continuous Casting*, 1988, pp. II–1–II–14.

[13] H. G. Suzuki, S. Nishimura, and Y. Nakamura, “Improvement of Hot Ductility of Continuously Cast Carbon Steels,” *Trans. ISIJ*, vol. 24, pp. 54–59, 1984.

[14] H. G. Suzuki, S. Nishimura, and S. Yamaguchi, “Characteristics of Hot Ductility in Steels Subjected to the Melting and Solidification,” *Trans. ISIJ*, vol. 22, pp. 48–56, 1982.

[15] F. Weinberg, “The Ductility of Continuously-Cast Steel Near the Melting Point - Hot Tearing,” *Metall. Trans. B*, vol. 10, pp. 219–227, 1979.

[16] B. Mintz and D. N. Crowther, “Hot ductility of steels and its relationship to the problem of transverse cracking in continuous casting,” *Int. Mater. Rev.*, vol. 55, no. 3, pp. 168–196, 2010.

[17] N. A. McPherson and A. McLean, *Continuous Casting Volume 8: Transverse Cracking in Continuously Cast Products*. Warrendale: Iron & Steel Society, 1997.

[18] T. H. Coleman and J. R. Wilcox, “Transverse cracking in continuously cast HSLA slabs - influence of composition,” *Mater. Sci. Technol.*, vol. 1, no. 1, pp. 80–83, 1985.

[19] C. Offerman, C.-A. Däcker, and C. Enström, “A Way to Avoid Transverse Cracking by Surface Temperature Control,” *Scand. J. Metall.*, vol. 10, no. 3, pp. 115–119, 1981.

[20] D. N. Crowther, “The Effects of Microalloying Elements on Cracking During Continuous Casting,” Beijing, China, in *Proceedings of the International Symposium 2001 on Vanadium Application Technology*, 2001.

[21] B. Mintz and R. Abushosha, “Effectiveness of hot tensile test in simulating straightening in continuous casting,” *Mater. Sci. Technol.*, vol. 8, pp. 171–177, 1992.

[22] B. Mintz, S. Yue, and J. J. Jonas, “Hot ductility of steels and its relationship to the problem of transverse cracking during continuous casting,” *Int. Mater. Rev.*, vol. 36, no. 5, pp. 187–217, 1991.

[23] H. G. Suzuki, S. Nishimura, J. Imamura, and Y. Nakamura, “Embrittlement of Steels Occuring in the Temperature Range from 1000 to 600°C,” *Trans. ISIJ*, vol. 24, no. 3, pp. 169–177, 1984.

[24] B. Ilschner, *Hochtemperatur-Plastizität: Warmfestigkeit und Warmverformbarkeit metallischer und nichtmetallischer Werkstoffe*, 23rd ed. Berlin/Heidelberg: Springer-Verlag, 1973.

[25] H. C. Chang and N. J. Grant, “Mechanism of Intercrystalline Fracture,” *Trans. AIME, J. Met.*, vol. 8, no. 5, pp. 544–551, 1956.

[26] S. K. Kim, J. S. Kim, and N. J. Kim, “Effect of Boron on the Hot Ductility of Nb-Containing Steel,” *Metall. Mater. Trans. A*, vol. 33, pp. 701–704, 2002.

[27] Y. Ohmori and Y. Maehara, “High-temperature ductility of AISI 310 austenitic stainless steels,” *Mater. Sci. Technol.*, vol. 2, no. 6, pp. 595–602, 1986.

[28] F. Zarandi and S. Yue, “The Effect of Boron on Hot Ductility of Nb-microalloyed Steels,” *ISIJ Int.*, vol. 46, no. 4, pp. 591–598, 2006.

[29] K. Yasumoto, Y. Maehara, S. Ura, and Y. Ohmori, “Effects of sulphur on hot ductility of low-carbon steel austenite,” *Mater. Sci. Technol.*, vol. 1, no. 2, pp. 111–116, 1985.

[30] Y. Maehara and Y. Ohmori, “The precipitation of AlN and NbC and the Hot Ductility of Low Carbon Steels,” *Mater. Sci. Eng.*, vol. 62, pp. 109–119, 1984.

[31] C. M. Chimani and K. Mörwald, “Micromechanical Investigation of the Hot Ductility Behavior of Steel,” *ISIJ Int.*, vol. 39, no. 11, pp. 1194–1197, 1999.

[32] J. R. Lewis, J. J. Jonas, and B. Mintz, “The Formation of Deformation Induced Ferrite during Mechanical Testing,” *ISIJ Int.*, vol. 38, no. 3, pp. 300–309, 1998.

[33] M. Militzer, R. Pandi, and E. B. Hawbolt, “Ferrite Nucleation and Growth During Continuous Cooling,” *Metall. Mater. Trans. A*, vol. 27, no. 6, pp. 1547–1556, 1996.

[34] D. N. Crowther and B. Mintz, “Influence of carbon on hot ductility of steels,” *Mater. Sci. Technol.*, vol. 2, no. 7, pp. 671–676, Jul. 1986.

[35] R. Abushosha, O. Comineli, and B. Mintz, “Influence of Ti on hot ductility of C – Mn – Al steels,” *Mater. Sci. Technol.*, vol. 15, no. 3, pp. 278–286, 1999.

[36] B. Mintz, J. R. Lewis, and J. J. Jonas, “Importance of deformation induced ferrite and factors which control its formation,” *Mater. Sci. Technol.*, vol. 13, pp. 379–388, 1997.

[37] A. Cowley, R. Abushosha, and B. Mintz, “Influence of Ar3 and Ae3 temperatures on hot ductility of steels,” *Mater. Sci. Technol.*, vol. 14, pp. 1145–1153, 1998.

[38] N. E. Hannerz, “Critical Hot Plasticity and Transverse Cracking in Continuous Slab Casting with Particular Reference to Composition,” *Trans. ISIJ*, vol. 25, pp. 149–158, 1985.

[39] Y. Maehara, K. Yasumoto, Y. Sugitani, and K. Gunji, “Effect of Carbon on Hot Ductility of As-cast Low Alloy Steels,” *Trans. ISIJ*, vol. 25, no. 10, pp. 1045–1052, 1985.

[40] A. Guillet and M. G. Akben, “Influence of Carbon Level on Hot Ductility of Microalloyed Steels,” in *Physical Simulation of Welding, Hot Forming and Continuous Casting*, 1988, pp. II–53–II–62.

[41] J. Wans, “Oberflächenqualität peritektisch erstarrender Kohlenstoffstähle – Vergleich zwischen Strangguss und Bandguss,” 2006.

[42] K. Matsuura, Y. Itoh, and M. Kudoh, “Effects of Carbon Content and Cooling Rate on Growth Rate of Gamma-phase during Peritectic Solidification in Iron-carbon System,” *Tetsu-to-Hagane*, vol. 84, no. 7, pp. 26–31, 1998.

[43] B. Yang, H. P. Degischer, H. Presslinger, G. Xia, and P. Reisinger, “Influence of Chemical Composition on High Temperature Tensile Properties of Carbon Steels,” *BHM Berg- und Hüttenmännische Monatshefte*, vol. 150, no. 9, pp. 313–320, 2005.

[44] B. Mintz, “Influence of nitrogen on hot ductility of steels and its relationship to problem of transverse cracking,” *Ironmaking Steelmaking*, vol. 27, no. 5, pp. 343–347, 2000.

[45] C. Ouchi and K. Matsumoto, “Hot Ductility in Nb-bearing High-strength Low-alloy Steels,” *Trans. ISIJ*, vol. 22, pp. 181–189, 1982.

[46] R. Abushosha, S. Ayyad, and B. Mintz, “Influence of cooling rate on hot ductility of C-Mn-Al and C-Mn-Nb-Al steels,” *Mater. Sci. Technol.*, vol. 14, pp. 346–351, 1998.

[47] N. Pradhan, N. Banerjee, B. B. Reddy, S. K. Sahay, C. S. Viswanathan, P. K. Bhor, D. S. Basu, and S. Mazumdar, “Control of transverse cracking in special quality slabs,” *Ironmaking Steelmaking*, vol. 28, no. 4, pp. 305–311, 2001.

[48] P. Sricharoenchai, C. Nagasaki, and J. Kihara, “Hot Ductility of High Purity Steels Containing Niobium,” *ISIJ Int.*, vol. 32, no. 10, pp. 1102–1109, 1992.

[49] G. I. S. L. Cardoso, B. Mintz, and S. Yue, “Hot ductility of aluminium and titanium containing steels with and without cyclic temperature oscillation,” *Ironmaking Steelmaking*, vol. 22, no. 5, pp. 365–377, 1995.

[50] H. Su, W. D. Gunawadarna, A. Tuling, and B. Mintz, “Influence of Al and P additions on hot ductility of steels,” *Mater. Sci. Technol.*, vol. 23, no. 11, pp. 1357–1366, Nov. 2007.

[51] W. Dahl and H. Hengstenberg, “Untersuchungen über die Ursachen für das Auftreten von Warmbruch an niedrig legierten allgemeinen Baustählen,” *Arch. für das Eisenhüttenwes.*, vol. 35, no. 12, pp. 1123–1132, 1964.

[52] B. Mintz, “The Influence of Composition on the Hot Ductility of Steels and to the Problem of Transverse Cracking,” *ISIJ Int.*, vol. 39, no. 9, pp. 833–855, 1999.

[53] E. Hurtado-Delgado and R. D. Morales, “Hot Ductility and Fracture Mechanisms of a C-Mn-Nb-Al Steel,” *Metall. Mater. Trans. B*, vol. 32, pp. 919–927, 2001.

[54] B. Mintz and J. M. Arrowsmith, “Hot-ductility behaviour of C-Mn-Nb-Al steels and its relationship to crack propagation during the straightening of continuously cast strand,” *Met. Technol.*, vol. 6, pp. 24–32, 1979.

[55] K. M. Banks, A. Tuling, and B. Mintz, “The influence of N on hot ductility of V-, Nb-, and Nb-Ti- containing steels using improved thermal simulation of continuous casting,” *J. South. African Inst. Min. Metall.*, vol. 111, no. 10, pp. 711–716, 2011.

[56] B. Mintz, J. M. Stewart, and D. N. Crowther, “The Influence of Cyclic Temperature Oscillations on Precipitation and Hot Ductility of a C-Mn-Nb-Al Steel,” *Trans. ISIJ*, vol. 27, pp. 959–964, 1987.

[57] K. R. Carpenter, R. Dippenaar, and C. R. Killmore, “Hot Ductility of Nb- and Ti-Bearing Microalloyed Steels and the Influence of Thermal History,” *Metall. Mater. Trans. A*, vol. 40, no. 3, pp. 573–580, Jan. 2009.

[58] H.-J. Eckstein, *Mikrolegieren von Stahl*, 1. Aufl. Leipzig: VEB Deutscher Verlag für Grundstoffindustrie, 1984.

[59] R. Abushosha, R. Vipond, and B. Mintz, "Influence of titanium on hot ductility of as cast steels," *Mater. Sci. Technol.*, vol. 7, no. 7, pp. 613–621, 1991.

[60] K. C. Cho, D. J. Mun, Y. M. Koo, and J. S. Lee, "Effect of niobium and titanium addition on the hot ductility of boron containing steel," *Mater. Sci. Eng. A*, vol. 528, no. 10–11, pp. 3556–3561, Apr. 2011.

[61] S. Luo, M. Zhu, and S. Louhenkilpi, "Numerical Simulation of Solidification Structure of High Carbon Steel in Continuous Casting Using Cellular Automaton Method," *ISIJ Int.*, vol. 52, no. 5, pp. 823–830, 2012.

[62] O. Comineli, R. Abushosha, and B. Mintz, "Influence of titanium and nitrogen on hot ductility of C-Mn-Nb-Al steels," *Mater. Sci. Technol.*, vol. 15, pp. 1058–1068, 1999.

[63] D. Djuric, O. Caliskanoglu, D. Leidinger, S. Ilie, and C. Sommitsch, "Untersuchung des zweiten Duktilitätsminimums mikrolegierter Stähle mit einer neu entwickelten Heißzugprüfung," *BHM Berg- und Hüttenmännische Monatshefte*, vol. 157, no. 8–9, pp. 296–300, Aug. 2012.

[64] C. Spradbery and B. Mintz, "Influence of undercooling thermal cycle on hot ductility of C-Mn-Al-Ti and C-Mn-Al-Nb-Ti steels," *Ironmaking Steelmaking*, vol. 32, no. 4, pp. 319–324, 2005.

[65] K. M. Banks, A. Tuling, C. Klinkenberg, and B. Mintz, "Influence of Ti on hot ductility of Nb containing HSLA steels," *Mater. Sci. Technol.*, vol. 27, no. 2, pp. 537–545, Feb. 2011.

[66] G. Alvarez de Toledo, O. Campo, and E. Lainez, "Influence of sulfur and Mn/S ratio on the hot ductility of steels during continuous casting," *Steel Res.*, vol. 64, no. 6, pp. 292–299, 1993.

[67] F. Weinberg, "The Strength and Ductility of Continuously- Cast Steels Above 800°C," *Metall. Trans. B*, vol. 10, no. 12, pp. 513–522, 1979.

[68] J. K. Brimacombe, F. Weinberg, and E. B. Hawbolt, "Formation of Longitudinal, Midface Cracks in Continuously-Cast Slabs," *Metall. Trans. B*, vol. 10, pp. 279–292, 1979.

[69] B. G. Thomas, J. K. Brimacombe, and I. V. Samarasekera, "The Formation of Panel Cracks in Steel Ingots: A State-of-the-Art Review: Part I: Hot Ductility of Steel," *ISS Trans.*, vol. 7, pp. 7–20, 1986.

[70] Y. Maehara and T. Nagamichi, "Effects of sulphur on hot ductility of niobium containing low carbon steels during low strain rate deformation," *Mater. Sci. Technol.*, vol. 7, no. 10, pp. 915–922, 1991.

[71] G. A. Wilber, R. Batra, W. F. Savage, and W. J. Childs, "The Effects of Thermal History and Composition on the Hot Ductility of Low Carbon Steels," *Metall. Trans. A*, vol. 6, no. 9, pp. 1727–1735, 1975.

[72] A. Cowley and B. Mintz, “Relative importance of transformation temperatures and sulphur content on hot ductility of steels,” *Mater. Sci. Technol.*, vol. 20, no. 11, pp. 1431–1439, Nov. 2004.

[73] D. N. Crowther and B. Mintz, “Influence of grain size on hot ductility of plain C-Mn steels,” *Mater. Sci. Technol.*, vol. 2, pp. 951–955, 1986.

[74] D. N. Crowther and B. Mintz, “Influence of grain size and precipitation on hot ductility of microalloyed steels,” *Mater. Sci. Technol.*, vol. 2, no. 11, pp. 1099–1105, 1986.

[75] K. A. Bywater and T. Gladman, “Influence of composition and microstructure on hot workability of austenitic stainless steels,” *Met. Technol.*, vol. 3, no. 1, pp. 358–365, 1976.

[76] F. Hassani, T. M. Maccagno, J. J. Jonas, and S. Yue, “Behavior of steels near the incipient melting temperature,” *Metall. Mater. Trans. A*, vol. 25, no. 1, pp. 125–133, 1994.

[77] T. Revaux, J. D. Guerin, and J.-P. Bricout, “Hot Ductility Study of Continuous Casting Steels,” *J. Mater. Sci. Technol.*, vol. 20, no. 1, pp. 19–22, 2004.

[78] E. Schmidtmann and M. Ebrecht, “Einfluss von chemischer Zusammensetzung und Herstellungsbedingungen auf die Rissanfälligkeit Te-legierter Automatenstähle,” *Steel Res.*, vol. 62, no. 11, pp. 522–527, 1991.

[79] H. Mizukami, Y. Shirai, and A. Yamanaka, “Prediction of Tensile Strength and Elongation of High Alloy,” *ISIJ Int.*, vol. 46, no. 7, pp. 1040–1046, 2006.

[80] A. M. El-wazri, F. Hassani, S. Yue, E. Essadiqi, L. E. Collins, and K. Iqbal, “The Effect of Thermal History on the Hot Ductility of Microalloyed Steels,” *ISIJ Int.*, vol. 39, no. 3, pp. 253–262, 1999.

[81] H. Luo, L. P. Karjalainen, D. a. Porter, H.-M. Liimatainen, and Y. Zhang, “The Influence of Ti on the Hot Ductility of Nb-bearing Steels in Simulated Continuous Casting Process.,” *ISIJ Int.*, vol. 42, no. 3, pp. 273–282, 2002.

[82] M. Lückl, S. Ilie, J. Six, and E. Kozeschnik, “Surface Microstructure Control during Continuous Casting of Micro- Alloyed Steel,” Montreal, in *Materials Science and Technology (MS&T)*, 2013.

[83] K. Yamamoto, H. G. Suzuki, Y. Oono, N. Noda, and T. Inoue, “Formation Mechanism and Prevention Method of Facial Cracks of Continuously Cast Steel Slabs Containing Boron,” *Tetsu-to-Hagane*, vol. 73, no. 1, pp. 115–122, 1987.

[84] S. K. Kim, Y. D. Lee, K. Hansson, and H. Fredriksson, “Influence of Cooling Rate on the Hot Cracking Formation of Nickel Rich Alloys,” *ISIJ Int.*, vol. 42, no. 5, pp. 512–519, 2002.

[85] J. Calvo, A. Rezaeian, J. M. Cabrera, and S. Yue, “Effect of the thermal cycle on the hot ductility and fracture mechanisms of a C-Mn Steel,” *An. Mec. la Fract.*, vol. 22, pp. 184–189, 2005.

[86] M. Vedani, D. Dellasega, and A. Mannuccii, “Characterization of Grain-boundary Precipitates after Hot-ductility Tests of Microalloyed Steels,” *ISIJ Int.*, vol. 49, no. 3, pp. 446–452, 2009.

[87] S. Großeiber, S. Ilie, C. Poletti, B. Harrer, and H. P. Degischer, “Influence of Strain Rate on Hot Ductility of a V-Microalloyed Steel Slab,” *Steel Res. Int.*, vol. 83, no. 5, pp. 445–455, May 2012.

[88] O. Caliskanoglu, S. Ilie, C. Beal, and C. Sommitsch, “Hot Ductility Behavior of a Continuously Cast Steel During Solidification,” Ostrava, Czech Republic, in *5th International Conference on Modelling and Simulation of Metallurgical Processes in Steelmaking*, 2013.

[89] D. N. Crowther, Z. Mohamed, and B. Mintz, “Influence of Micro-alloying Additions on the Hot Ductility of Steels Heated Directly to the Test Temperature,” *Trans. ISIJ*, vol. 27, pp. 366–375, 1987.

[90] Y. Maehara, K. Nakai, K. Yasumoto, and T. Mishima, “Hot Cracking of Low Alloy Steels in Simulated Continuous Casting-Direct Rolling Process,” *Trans. ISIJ*, vol. 28, pp. 1021–1027, 1988.

[91] B. Mintz, “Understanding the low temperature end of the hot ductility trough in steels,” *Mater. Sci. Technol.*, vol. 24, no. 1, pp. 112–120, Jan. 2008.

[92] K. M. Banks, A. Tuling, and B. Mintz, “Influence of thermal history on hot ductility of steel and its relationship to the problem of cracking in continuous casting,” *Mater. Sci. Technol.*, vol. 28, no. 5, pp. 536–542, 2012.

[93] F. Ma, G. Wen, P. Tang, G. Xu, F. Mei, and W. Wang, “Effect of Cooling Rate on the Precipitation Behavior of Carbonitride in Microalloyed Steel Slab,” *Metall. Mater. Trans. B*, vol. 42, no. 1, pp. 81–86, Nov. 2011.

[94] T. Kato, Y. Ito, M. Kawamoto, A. Yamanaka, and T. Watanabe, “Prevention of Slab Surface Transverse Cracking by Microstructure Control,” *ISIJ Int.*, vol. 43, no. 11, pp. 1742–1750, 2003.

[95] D. Djuric, “K1-MET Annual Meeting - Vienna,” 2011.

[96] A. Ofenheimer, “Adaptierung und Inbetriebnahme einer Prüfmaschine für Hochtemperatur-Zugversuche im teilflüssigen Bereich,” 2001.

[97] T. Revaux, P. Deprez, J.-P. Bricout, and J. Oudin, “In situ Solidified Hot Tensile Test and Hot Ductility of Some Plain Carbon Steels and Microalloyed Steels,” *ISIJ Int.*, vol. 34, no. 6, pp. 528–535, 1994.

[98] D. Djuric, “Untersuchung des ersten Duktilitätsminimums eines Stahles mit einer neu entwickelten Aufschmelz-Heißzugprüfmethode,” 2012.

[99] C. Hoflehner, “Konstruktion einer Abschreckvorrichtung,” 2013.

[100] W. Rasband, "ImageJ 1.46r," *National Institutes of Health, USA*. [Online]. Available: http://imagej.nih.gov/ij/.

[101] M. Domankova, "TEM-investigations of samples 334, 495, 496 and 497," Trnava, Slovakia, 2015.

[102] E. Kozeschnik, "MatCalc version 5.52 (database mc_fe_v2.019)." .

[103] E. Kozeschnik, J. Svoboda, and F. D. Fischer, "Modified evolution equations for the precipitation kinetics of complex phases in multi-component systems," *CALPHAD*, vol. 28, no. 4, pp. 379–382, 2004.

[104] J. Svoboda, F. D. Fischer, P. Fratzl, and E. Kozeschnik, "Modelling of kinetics in multi-component multi-phase systems with spherical precipitates I," *Mater. Sci. Eng. A*, vol. 385, no. 1–2, pp. 166–174, 2004.

[105] E. Kozeschnik, J. Svoboda, P. Fratzl, and F. D. Fischer, "Modelling of kinetics in multi-component multi-phase systems with spherical precipitates II," *Mater. Sci. Eng. A*, vol. 385, no. 1–2, pp. 157–165, 2004.

[106] M. Lückl, "Determination of the phase transformation behavior for C-Mn and C-Mn-Ti-Nb steel by JMatPro," 2015.

[107] N. Saunders, Z. Guo, X. Li, A. P. Miodownik, and J. Schillé, "Using JMatPro to Model Materials Properties and Behavior," *J. Miner. Met. Mater. Soc.*, vol. 55, no. 12, pp. 60–65, 2003.

[108] E. Kozeschnik, W. Rindler, and B. Buchmayr, "Scheil – Gulliver simulation with partial redistribution of fast diffusers and simultaneous," *Int. J. Mater. Res.*, vol. 98, no. 9, pp. 826–831, 2007.

[109] B. Sonderegger and E. Kozeschnik, "Interfacial Energy of Diffuse Phase Boundaries in the Generalized Broken-Bond Approach," vol. 41, no. 12, pp. 3262–3269, 2010.

[110] R. Abushosha, R. Vipond, and B. Mintz, "Influence of sulphur and niobium on hot ductility of as cast steels," *Mater. Sci. Technol.*, vol. 7, no. 12, pp. 1101–1107, 1991.

[111] I.-W. Chen and A. S. Argon, "Creep cavitation in 304 stainless steel," *Acta Metall.*, vol. 29, no. 7, pp. 1321–1333, 1981.

[112] B. Mintz and Z. Mohamed, "Hot Ductility of Directly Cast Microalloyed Steels," in *Physical Simulation of Welding, Hot Forming and Continuous Casting*, 1988, pp. II–25–II–37.

[113] B. Mintz and A. Cowley, "Deformation induced ferrite and its influence on the elevated temperature tensile flow stress – elongation curves of plain C – Mn and Nb containing steels," vol. 22, no. 3, pp. 279–292, 2006.

[114] P. J. Wray, "Plastic flow and failure of plain carbon steels in ferrite+austenite region," *Met. Technol.*, vol. 8, pp. 466–471, 1981.

[115] H. Luo and P. Zhao, “Influence of excess titanium on hot ductility of C-Mn-Cr-Al steel,” *Mater. Sci. Technol.*, vol. 17, no. 12, pp. 1589–1595, 2001.

[116] U. H. Lee, T. E. Park, K. S. Son, M. S. Kang, Y. M. Won, C. H. Yim, S. K. Lee, I. Kim, and D. Kim, “Assessment of Hot Ductility with Various Thermal Histories as an Alternative Method of in situ Solidification,” *ISIJ Int.*, vol. 50, no. 4, pp. 540–545, 2010.

[117] M. Lückl, O. Caliskanoglu, S. Ilie, J. Six, and E. Kozeschnik, “Impact of Surface Structure Control Cooling during Continuous Casting on Hot Ductility of Microalloyed Steel,” *Steel Res. Int.*, in press, 2015.

[118] N. Baba, K. Ohta, Y. Ito, and T. Kato, “Prevention of slab surface transverse cracking at Kashima n° 2 caster with Surface Structure Control (SSC) cooling,” *Rev. Métallurgie*, vol. 103, pp. 174–179, 2006.

[119] G. Walmag, A. Schmitz, and C. Marique, “A New Secondary Cooling Concept for Avoiding Surface Cracks During Casting of Peritectic and Micro-Alloyed Steels,” Birmingham, UK, in *4th European Continuous Casting Conference*, 2002.

[120] M. Suzuki, C. H. Yu, H. Shibata, and T. Emi, “Recovery of Hot Ductility by Improving Thermal Pattern of Continuously Cast Low Carbon and Ultra Low Carbon Steel Slabs for Hot Direct Rolling,” *ISIJ Int.*, vol. 37, no. 9, pp. 862–871, 1997.